Studies of Niobium and Development of Niobium Resonant RF Cavities for Accelerator Driven System

By

JAYANTA MONDAL

(Enrolment Number: PHYS01200704017)

Bhabha Atomic Research Centre, Mumbai – 400 085 INDIA

A thesis submitted to the

Board of Studies in Physical Sciences

In partial fulfillment of requirements

For the Degree of

DOCTOR OF PHILOSOPHY

of

HOMI BHABHA NATIONAL INSTITUTE

January, 2013

Homi Bhabha National Institute

Recommendations of the Viva Voce Board

As members of the Viva Voce Board, we certify that we have read the dissertation prepared by **JAYANTA MONDAL** entitled " Studies of Niobium and Development of Niobium Resonant RF Cavities for Accelerator Driven System" and recommend that it may be accepted as fulfilling the dissertation requirement for the Degree of Doctor of Philosophy.

_____**Date:**

Chairman: **Prof. S. Kailas**

_____**Date:**

Guide/Convenor: **Prof. K. C. Mittal**

_____**Date:**

Member 1: **Prof. S. K. Gupta**

_____**Date:**

Member2: **Prof. R. G. Pillay**

_____**Date:**

Examiner: **Dr. Amit Roy**

_____

Final approval and acceptance of this dissertation is contingent upon the candidate's submission of the final copies of the dissertation to HBNI. I hereby certify that I have read this dissertation prepared under my direction and recommend that it may be accepted as fulfilling the dissertation requirement.

Date:

Place: Mumbai **Guide: Prof. K. C. Mittal**

STATEMENT BY AUTHOR

This dissertation has been submitted in partial fulfillment of requirements for an advanced degree at Homi Bhabha National Institute (HBNI) and is deposited in the Library to be made available to borrowers under rules of the HBNI.

Brief quotations from this dissertation are allowable without special permission, provided that accurate acknowledgement of source is made. Requests for permission for extended quotation from or reproduction of this manuscript in whole or in part may be granted by the Competent Authority of HBNI when in his or her judgment the proposed use of the material is in the interests of scholarship. In all other instances, however, permission must be obtained from the author.

Jayanta Mondal

DECLARATION

I, hereby declare that the investigation presented in the thesis has been carried out by me. The work is original and has not been submitted earlier as a whole or in part for a degree / diploma at this or any other Institution / University.

Jayanta Mondal

Dedicated to

My Parents

Late. Shri. Anil Kumar Mondal

Smt. Anna Mondal

My Wife

Dr. Tanushree Mondal

And

My Daughter

Miss. Tanisha Mondal

ACKNOWLEDGEMENTS

Foremost, I would like to express my sincere gratitude to my guide Prof. K. C. Mittal for the continuous support of my Ph.D study and research, for his patience, motivation, enthusiasm, and immense knowledge. His guidance helped me in all the time of research and writing of this thesis.

Besides my advisor, I would like to thank the rest of my Doctoral committee: Dr. S. K. Gupta, Dr. R. G. Pillay and Dr. S.Kailas for their encouragement, insightful comments, and hard questions.

My sincere thank also goes to Dr. Ganpati Myneni of Thomas Jefferson Lab, Newport News, Virginia, USA for giving me the opportunity to work at Jlab. His immense knowledge, motivation and guidance helped me tremendously while doing experiments at Jlab or interpreting the experimental results.

Now I would like to thank a special person from Jlab Dr. Gianluigi Ciovati popularly know as Gigi. I feel myself fortunate that I have worked under his supervision during my stay at Jlab. He is so knowledgeable and having such a good experimental hand that really excited and motivated me while doing the experiments at Jlab. I could not have imagined a better mentor for my Ph.D study. Besides helping me academically he has taken care of me and my family like a big brother and I truly confess that a 'thank-you' is not sufficient for that.

I also would like to express my sincere gratitude to Dr. Peter Knisel (Jlab). He has helped and guided me during sample testing, cavity fabrication, cleaning, RF testing. He has also given me the opportunity to attend and a slot for the oral presentation in SRF 2009.

I thank my fellow labmates and seniors in Jefferson Lab: Gary Slack and Bob Manus (Cavity Fabrication), Michael Morrone (during assembly and all last minute fixes for heaters, thermometers), Pete Kushnick (cryo-support), Caroline (for all kind of administrative support) and a big thank you to all my colleagues and friends.

I thank Dr. D. Dutta and Dr. P. K. Pujari for helping me with the positron annihilation studies.

I thank all my friend and colleagues from Accelerator and Pulse Power Division.

Last but not the least; I would like to express gratitude to my family without their support I could not have done this work.

Jayanta Mondal

CONTENTS

LIST OF ABREVIATIONS

BCS	-	Bardeen, Cooper, Schrieffer
GL	-	Ginzburg - Landau
RF	-	Radio frequency
SCRF	-	Superconducting radio frequency
LTB	-	Low temperature baking
BCP	-	Buffered chemical polishing
EDM	-	Electric discharge machining
mfp	-	Mean free path
HK	-	Hu, Korenman
RRR	-	Residual resistivity ratio
ADSS	-	Accelerator driven subcritical system

SYNOPSIS

Niobium is the material of choice for superconducting radio frequency (SRF) cavity programs in different particle accelerator laboratories because of its mechanical properties favorable for formability, machinability and also high T_C and high first flux penetration field H_{C1}.SRF cavity performances have been continually improved for past three decades to achieve reproducible quality factor of 10^{10} and accelerating fields (E_{acc}) of 30-35MV/m. The present approach for the fabrication of superconducting radio frequency (SRF) cavities is to roll and deep draw sheets of polycrystalline high-purity niobium. Jefferson Laboratory pioneered the use of large-grain/single-crystal Nb directly sliced from an ingot for the fabrication of single-crystal high-purity Nb SRF cavities [1].The large grain/single crystal niobium has several potential advantages over the polycrystalline niobium as discussed in Ref. [2] and has become a viable alternative to the standard fine grain (ASTM grain size>6 μm), high purity (RRR ≥ 250) niobium for the fabrication of high-performance SRF cavities for particle accelerators.

The other alternative approach of cavity fabrication is the niobium – coated copper cavities pioneered by CERN [3]. In many laboratories this path of coating technology is pursued as an alternative to bulk niobium technology [4].

Niobium metal superconductivity in SRF accelerators is a nanoscale, near surface phenomena because of small RF penetration depth of the order of 10 – 100 nm. The cavity performance improvement over the past 3-4 decades strongly indicates the topography and the chemistry of the inner surface impacts the final cavity performance [5].

Present day cavity preparation chemistry for the inner surface follows two different routes namely buffered chemical polishing (BCP) and electropolishing (EP). The BCP solution is

prepared with 1:1:1 or 1:1:2 (volume) mixture of HNO_3(69%), HF(48%) and H_3PO_4 (85%) at 15-20 ^{0}C. The large grain or single crystal material after BCP produces very smooth and shiny surfaces; the measured surface roughness was 50 times better then the BCP'd polycrystalline niobium [6]. In the present thesis the studies are carried out with BCP surface treatment and EP route is not explored.

It has been known for quite some time that the low temperature baking (LTB) (100 – 140 ^{0}C) is a necessary final preparation stage to achieve high accelerating gradients in niobium RF cavity [7, 8]. To date there exists different models to understand the LTB effect on niobium RF cavity, although none of them is complete in a sense that they can explain all the experimental observations. At present there is an oxygen diffusion model [9] which takes into account the oxygen diffusion with LTB resulting in dilution of oxygen pollution over the penetration depth. Over the time as research progressed it has been found that there are other possibilities which can explain Q-drop and baking effect namely the mechanisms based on hot-spot [10], dislocations [11], interface tunnel exchange [12] and magnetic impurities [13]. A present study of B. Visentin [14] on niobium samples with positron annihilation spectroscopy has shown that there is an increase of vacancy site with the LTB in a length scale of about 120 nm from the surface and as explained this might be due to the dissociation of hydrogen-vacancy complexes by baking followed by hydrogen diffusion.

An attempt has been made to study the material and superconducting properties of large grain niobium of different RRR value. In the present study the large grain samples are treated with BCP followed by different post purifications such as 600^{0}C annealing, low temperature baking (LTB) in the range of 100 – 140 ^{0}C. To understand the low temperature baking improvement of cavity performance experimental studies of surface magnetization are carried out.

Also the study of positron annihilation spectroscopy shows a correlation of defect density dependence before and after annealing.

The performance of SRF cavity is mostly described by the dependence of the unloaded quality factor Q_0 with accelerating electric field E_{acc}. Several past experiments had shown that there is a continuous degradation of Q_0 with E_{acc} (or peak magnetic field B_p) in the range of 20 – 100 mT. This phenomenon is termed as 'medium field Q-slope'. The present study includes the prototype single cell low beta cavity design, fabrication, EB welding and low temperature RF test at 2K. In this study the medium field Q-Slope has been analyzed with the help of an added non linear term in Heabel's analytical model [15] and an additional linear term for the BCS surface resistance R_s [16].

Chapter 1: Basics of Superconductivity and Superconducting Radio Frequency Cavity

Superconductivity in mercury below Tc = 4.2K, was discovered in 1911 by Kammerlingh Onnes in Leiden. Niobium is the material of choice for SRF cavities as its properties are favorable for formability, machining and also high T_C and high first flux penetration field H_{C1}.This chapter introduces the definitions of characteristic length scale of superconductivity, magnetization behavior, thermal conductivity dependence in superconducting state [17] and also discusses the phenomenological Ginzburg-Landau theory of superconductivity.

The next part of this chapter discusses the basics of SRF cavities and different structure types with different β (v/c) values. Then the figure of merits for superconducting cavity such as accelerating gradient, quality factor Q_0, shunt impedance, peak electric and magnetic field are described. The deviations of ideal behavior of SRF cavity is attributed to different loss

mechanisms. The surface resistance is greater than the BCS resistance due to the residual resistance. The surface resistance variation with increasing accelerating gradient causes low field [18], medium field Q slopes and high field Q drop [19, 20, 21, 22] before it reaches the theoretical quench field. A detailed discussion of models of low and medium field Q-slope is presented, considering these two slopes are relevant for our studies of low β cavities.

Chapter: 2 Motivation for the Present Research

Because of potential advantages of large grain material, the interest in investigating material properties with different surface treatments will help to understand the cavity performance behavior with the same surface preparation. This thesis presents results of investigations on following material properties and the cavity behavior,

- Thermal Properties – thermal conductivity, phonon peak and the effect of different processing and trapped vortices on the thermal conductivity of niobium ingot.
- Magnetic properties – H_{c1}, H_{c2}, H_{c3} and changes in London penetration depth measured with different surface treatments.
- Positron annihilation studies to find defect density after different processing.
- Simulation of surface magnetization behavior before and after LTB.
- Mechanical properties – yield strength, tensile strength, and elongation that help to form the cavity.
- SRF cavity development with large grain niobium- design of cavity, EB-welding, surface treatments, room temperature RF characteristics and testing at 2K and medium field Q-slope analysis.

Chapter: 3 Low temperature (1.8K–5K) Thermal Conductivity Measurement

The electrons which have condensed into Cooper pairs do not contribute to any disorder or entropy transport anymore. The remaining fraction of electrons which contribute to heat transport decreases exponentially with decreasing temperature. Experimental thermal conductivity results are fitted with *Bardeen-Rickayzen-Tewordt* (BRT) theory. The important observation is that the superconducting gap energy does not change with the annealing of chemically polished large grain samples. But the decrease of lattice constant a_0 implies that hydrogen comes out from the bulk of the material on annealing, which is otherwise trapped in the tetrahedral positions increasing the lattice parameter. The measurements clearly show the presence of a phonon peak at around 2K. One important observation is that the phonon peak is eliminated by the presence of trapped vortices due to the strong scattering of phonons with vortex cores. When the vortices are trapped inside the sample, the fitting parameters indicate a reduction of the gap energy α due to the low energy excitations having very small energy gap ~ Δ_0^2/E_F close to the vortex core. Also the effective number of conduction electrons decreases due to the bound excitations in the vortex cores. The dependence of the thermal conductivity with the applied magnetic field for the samples with and without trapped vortices show the same H_{C1} and H_{C2} values as from the magnetization measurement. Finally when the temperature of the samples is cycled above T_c, the thermal conductivity measured for the sample in absence of an applied magnetic field is restored. The temperature dependence of the thermal conductivity at low temperature and low magnetic field agrees qualitatively with the model of *Vinen et al* [23]. In the vicinity of H_{C2} the thermal conductivity agrees quite well with *Houghton-Maki* [24] theory for zero-field cooled samples. But if there is initial flux trapped within the sample, the measured

thermal conductivity deviates from the *Houghton-Maki* theory and observed an increase in thermal conductivity in the range of $\mathbf{0.2 \leq \mu \leq 0.6}$. Where μ is the transport coefficient dependent on the reciprocal lattice vector k_c, Fermi velocity v_F and the electron mean free path l_e.

Chapter: 4 Low Temperature Baking Effect on Bulk Magnetization, Penetration Depth and Surface Magnetization

The measurement of DC magnetization provides the first flux penetration value H_{C1}, the upper critical magnetic field H_{C2} and from M-H curve the thermodynamic critical field H_C is calculated. Pinning of vortices leads to irreversible magnetization curves.

By connecting a small pick-up coil around the sample rod as part of a L-C oscillator, it is possible to measure the changes of the penetration depth as a function of the applied DC magnetic field by measuring the changes of the oscillator's resonant frequency f_0 (the base frequency is 270 kHz, sampling up to a depth ~10 μm) while slowly ramping up and down the magnetic field above H_{C3}. This method, which was applied for Nb surface studies, provides information about surface pinning and allows measuring the surface critical field B_{c3}. The irreversibility of the curve between B_{c1} and B_{c2} is an indication of surface pinning. The result shows that with the increased baking temperature the contaminated layer thickness increases to an average of 5.8 nm, 9.5 nm and 19.6 nm at 100 ^{0}C, 120 ^{0}C, and 140 ^{0}C baking temperature respectively. But at 140 ^{0}C both the contaminated layer thickness and bulk H_{C2} increases which may be due to the partial dissociation of the Nb_2O_5 layer as explained in the oxygen diffusion model. The oxygen diffusion model corresponds to a diffusion depth of 7.6 nm, 19 nm and 40 nm for a baking at 100 ^{0}C, 120 ^{0}C, and 140 ^{0}C for 12 hour duration. Except for the 100 ^{0}C bake the experimentally derived surface layer thickness is about half of the oxygen diffusion depth

calculated by the theoretical model. Also the first flux penetration i.e B_{C1} increases with the 100 ^{0}C and 120 ^{0}C baking for 12 hr. in vacuum. But it falls to 100 mT at 140 ^{0}C baking. The data has been analyzed with the Schmidt's model [25] taking into account the low temperature correction to H_{c3}/H_{c2} ratio in the clean limit. The enhanced H_{c3}/H_{c2} ratio has been interpreted as due to the increased contaminated surface layer thickness. This fact is further corroborated by the penetration depth measurement.

Chapter: 5 Defect Depth Profiling by Positron Annihilation Spectroscopy

Defect depth profiles were studied by slow positron implantation spectroscopy using a 50 mCi, 22Na positron source. In the defect depth profiling study the positron energy E is varied from 0.2 to 20.2keV. The line shape parameter or the S-parameter dependence on positron energy is fitted by the VEFIT software package. Large grain niobium specimen (square shaped, 1cm by 1 cm, thickness 3mm) was first chemically polished with a mixture of HF, HNO_3, H_3PO_4 in a volumetric ratio of 1:1:1. About 180 μm is removed from the outer surface of the specimen. Then we performed the defect depth profile study with the positron beam. In the second phase of the experiment the sample was heat treated at 600 ^{0}C for 10 hour in a vacuum of the order of 10^{-5} Torr. This was done to degas the hydrogen from the sample. Then we carried out the positron implantation spectroscopy measurements following this treatment. It has been observed that after annealing the defect density increases at the surface layer. This might be due to the hydrogen degassing which when comes out of the specimen leaves open volume defect within the sample. The three layer fitting of the chemically polished sample showed a surface layer of 79 nm thick has the diffusion length of 65 nm, from 79 nm to 100nm layer has a diffusion length of 0.5 nm and the bulk of the sample have a diffusion depth of 7.4 nm. After annealing it shows a surface

layer of 10 nm with diffusion length 39.4 and the bulk is having a diffusion length of 139 nm. The important observation is that after annealing the defect density at the surface increases whereas in the bulk the defect density decreases.

Chapter: 6 Design, Fabrication and RF Test of β = 0.49, f = 1050 MHz Elliptical Cavity

The first part of the chapter presents the experimental setup and mechanical measurements of large grain niobium samples. Mechanical properties such as yield strength, tensile strength and elongation were measured with different post-purification of as received material.

The second part of the chapter presents the design, fabrication, electron beam welding and low temperature RF testing of β = 0.49, f = 1050 MHz fine grain and large grain cavities. Two single cell cavities of frequency 1050 MHz, b =0.49 have been designed, fabricated and tested at 2 K. One was made of polycrystalline niobium and the other one was made of large grain niobium. Both the cavities exhibited an unloaded Q value of $1x10^{10}$ and reached the design value of 5 MV/m for the low β section of the proton linac. The large grain cavity was quenching at 6 MV/m at 2K and several areas with many pits on the surface were visible. The experimental value of Lorentz force detuning coefficient was significantly high and suggests the need for a stiffening ring for a multi-cell structure. The medium field Q-slope analysis showed a significantly higher value of γ in the large grain cavity compare to the fine grain cavity although both the cavities were subjected to similar surface treatments before the RF test. The factor γ depends on RBCS, Kapitza raistamne Rk, thermal conductivity K and the wall thickness d. The higher value of γ was most likely related to higher RF losses at the pit's locations.

Chapter: 7 Summary and Conclusions

Based on the above studies the following conclusions have been made.

1. High purity niobium mechanical properties vary from batch to batch and are very sensitive to various treatments and handling.
2. Elastic behavior of high purity niobium remains unchanged with different heat treatments only a change in yield strength is observed after 1200^0C heat treatment.
3. The thermal conductivity measurement of large grain niobium samples in the Meissner state is well described by the model of Ref. [15] within the experimental error of $\pm 6\%$.
4. One important observation is that the phonon peak is eliminated by the presence of trapped vortices due to the strong scattering of phonons with vortex cores.
5. The dependence of the thermal conductivity with and without trapped vortices show the same H_{C1} and H_{C2} values in the magnetization measurement.
6. The temperature dependence of the thermal conductivity at low temperature and low magnetic field agrees qualitatively with the model of *Vinen et al*. In the vicinity of H_{C2} the thermal conductivity agrees quite well with *Houghton-Maki* theory for the zero-field cooled samples. But if there is initial flux trapped within the sample, the measured thermal conductivity deviates from the *Houghton-Maki* theory and it was observed an increase in thermal conductivity in the range of $0.2 \leq \mu \leq 0.6$.
7. The bulk properties of the samples such as T_C, B_C, H_{C1} and H_{C2} were essentially unchanged with surface treatments such as BCP, 600 ^{0}C annealing, LTB.

8. Surface pinning measurement shows that the H_{C3} value increases with the increased LTB temperature. It also shows that the surface H_{C1} is lower than the bulk H_{C1} and that the highest surface H_{C1} was obtained after baking at 120°C for 12 hour.
9. The irreversibility between H_{C1} and H_{C2} decreases significantly with the low temperature baking, thus a reduction in the surface pinning centers can be inferred.
10. The increase of H_{C3}/H_{C2} ratio in the LTB regime has been analyzed with the Schmidt's model taking into account the low temperature correction to H_{C3}/H_{C2} ratio. The enhanced H_{C3}/H_{C2} ratio has been interpreted as the increased contaminated surface layer thickness. This fact is further corroborated by the penetration depth measurement.
11. The important observation in the positron annihilation studies (PAS) is that the surface defect density increases after the annealing whereas in the bulk the defect density decreases. This is complimentary to the conclusion inferred with the magnetization measurement.
12. RF Properties of 1050 MHz, $\beta = 0.49$ single cell Elliptical cavity has been studied by means of 2D cavity tuning code SUPERFISH and 3D High Frequency Simulation code CST Microwave Studio. Electromagnetic properties of the optimized cavity shape carried out on 2D code SUPERFISH are compared with 3D code CST Microwave Studio. Numbers of mesh cells are optimized by the adaptive mesh solver technique. It has been observed that the mode frequency remains almost constant for more than 10^5 mesh cells.
13. Two single cell cavities of frequency 1050 MHz, $\beta = 0.49$ have been designed, fabricated and tested at 2 K. One was made of polycrystalline niobium and the other one was of large grain niobium. Both the cavities exhibited an unloaded Q value of 1×10^{10} and reached the design value of 5 MV/m for the low β section of the proton linac.

14. The medium field Q-slope analysis showed a significantly higher value of γ in the large grain cavity compare to the fine grain cavity although both the cavities were subjected to similar surface treatments before the RF test. The higher value of γ is unsual for this type of material and was most likely related to higher RF losses at the pits' locations.

REFERENCES

[1] P. Kneisel, G.R.Myneni, G.Ciovati, J.Sekutowicz, T.Carneiro, Proc of the 2005 Particle Accelerator Conference,Tennessee, TPPT076.

[2] P. Kneisel, Proc of the 13th SRF Workshop, Peking Univ, China, October 2007, Th102.

[3] C. Benvenuti, Part. Accel. 40 (1992) 43.

[4] Proceedings of the 8th Workshop on RF Superconductivity, Abano Terme, Italy, 1997.

[5] Hui Tian , Charles E. Reece , Michael J. Kelley , Shancai Wang , Lukasz Plucinski , Kevin E. Smith , Matthew M. Nowell . "Surface studies of niobium chemically polished under conditions for superconducting radio frequency (SRF) cavity production", Applied Surface Science 1263, 253 (2006)

[6] P. Kneisel, G.R. Myneni, G. Ciovati, J. Sekutowicz, T. Carneiro. "Preliminary results from single crystal and very large crystal niobium cavities**",** 3991**,** 2005 Particle Accelerator Conference, Knoxville, Tennessee

[7] P. Kneisel, in Proceedings of the 9th Workshop on RF Superconductivity, Santa Fe, NM,1999, edited by F.Krawczyk (LANL, Los Alamos, NM, 2000), p. 328.

[8] B. Visentin, J. P. Charrier, and B. Coadou, in Proceedings of the 1998 European Particle Accelerator Conference, Stockholm, Sweden, 1998, edited by S. Myers, L. Liljeby, Ch. Petit-Jean-Genaz, J. Poole, and K.-G. Rensfelt (Institute of Physics, Philadelphia, USA, 1998), p. 1885.

[9] Gianluigi Ciovati, Appl. Phys. Lett. 89, 022507 (2006).

[10] G. Ciovati and A. Gurevich, Phys. Rev. ST Accel. Beams 11, 122001 (2008)

[11] A. Romanenko, in Proceedings of the 14th International Conference on RF Superconductivity, Berlin, 2009, edited by M. Abo-Bakr, B. Kuske, A. Liebezeit, S. Voronenko, and V. Schaa (SRF, Berlin, 2009), paper TUOAAU02, p. 95.

[12] J. Halbritter, in Proceedings of the 14th International Conference on RF Superconductivity, Berlin, 2009, Ref. [5], paper TUPPO089, p. 450.

[13] T. Proslier et al. Appl. Phys. Lett. 92, 212505 (2008).

[14] B. Visentin, M. F. Barthe, V. Moineau, and P. Desgardin, Phys. Rev. ST Accel. Beams 13, 052002 (2010).

[15] J. Halbritter, J. Appl. Phys. 97 (2005) 083904.

[16] G. Ciovati, J. Halbritter / Physica C 441 (2006) 57–61.

[17] K. R. Krafft, "Thermal conductivity of niobium – a survey of theory and experiment" CLANS 80/468, Laboratory of Nuclear Studies, Cornell University, Ithaca, N. Y.

[18] J. Halbritter, in *Proceedings of the 10th Workshop on RF Superconductivity*, *Tsukuba*, *2001* p. 292.

[19] J. Halbritter, Z. Physik B **31**, 19 (1978).

[20] J. Knobloch, R. L. Geng, M. Liepe, and H. Padamsee, in *Proceedings of the 9th Workshop on RF Superconductivity*, *Santa Fe*, *NM*, *1999* p. 77.

[21] B. Bonin and H. Safa, Supercond. Sci. Technol. **4**, 257 (1991).

[22] A. Gurevich, in *Proceedings of the Pushing the Limits of RF Superconductivity Workshop, Argonne*, *2004*, edited by K.-J. Kim and C. Eyberger (ANL, Argonne, IL, 2005) p. 17.

[23] W.F.Vinen, E.M.Forgan, C.E.Gough and M.J.Hood, Physica (Utrecht), 55, 94 (1971).

[24] A. Houghton, K. Maki, Phys. Rev. B 4, 843 (1971).

[25] V.V.Shmidt, in Physical Metallurgy, Physical Chemeistry and Metals Physics of Superconductors, p-90 (Moscow: Nauka, in Russian 1967).

Publications during Ph.D work

Journal Publications

1. **J. Mondal,** G.Ciovati, K.C.Mittal, G.R.Myneni**.** (2012)**. "**Thermal conductivity of large grain niobium and effect of trapped vortices in the temperature range 1.8-5K" Pramana-Journal of Physics, 635, 78(4), (2012).

2. **J. Mondal**, G. Ciovati, P. Kneisel, K. C. Mittal and G. R. Myneni (2011). "Design, fabrication, RF test at 2K of 1050 MHz, $\beta = 0.49$ single cell large and fine grain niobium cavity", Journal of Instrumentation, 6 – T11003, JINST, 2011.doi:10.1088/1748-0221/6/11/T11003.

3. Amitava Roy, **J. Mondal** and K.C. Mittal (2008). "RF properties of 1050 MHz, $\beta = 0.49$ Elliptical cavity for High Current Proton Acceleration", Journal of Instrumentation, 3-P04002, JINST, 2008.

Conference Publications

4. **J. Mondal**, K.C.Mittal, G.Ciovati, P.kneisel, G.R.Myneni, "Characterization of Ingot Materials for SRF Cavity Production", Proceedings of **SRF2009**, Berlin, Germany, THOAAU01, Page: 455-461.

5. **J. Mondal**, T.K.Saha, S.Sarkar, S.B.Jawale, R. S. Vohra, A.V.Bapat, "Design, fabrication, room temperature RF test of 1050 MHz, $\beta = 0.49$ single cell large grain niobium cavity"**,** International Vacuum Symposium-2012, VECC, Kolkata.

6. T.K.Saha, **J. Mondal**, K.C.Mittal, K.G.Bhushan and A.V.Bapat, "Fabrication of niobium superconducting accelerator cavity by electron beam welded joints" International Vacuum Symposium-2012, VECC, Kolkata.

LIST OF FIGURES

P.Bauer et.al "Review of Q-drop in SRF cavities" TD-05-56, January 2006]

Fig.3.1 Schematic of the system for measurements of superconducting properties of the sample and picture of the sample rod.

Fig. 3.2 Critical magnetic field as a function of temperature measured on a Indium rod, 99.99% purity. The solid line is a least-square fit with Eq. (3).

Fig. 3.3 The ratio of $K_{es} / K_{en} = R(y)$ as a function of reduced temperat**ure,** $\boldsymbol{T / T_c = \alpha / y}$ (within the experimental temperature range)

Fig. 3.4 Experimental thermal conductivity data for 180 μm buffered chemical polished Niobium samples from four different ingots. Solid lines are the fitting curves.

Fig. 3.5 Experimental thermal conductivity data for 600^0C heat treated Niobium samples from four different ingots. Solid lines are the fitting curves.

Fig. 3.6 Thermal conductivity data in normal and superconducting state for the sample C1. Solid lines are the fitting curves with Eqn.(6).

Fig. 3.7 Plot of k_S versus T, ■ C1-Zero field, *C1-Trapped flux 81 mT, Δ A1-Zero field, ○ A1-Trapped flux 60 mT, solid lines are the fitting curves of Eqn. (6).

Fig.3.8 Magnetization curves at T = 2K with and without remnant magnetization for ---- A1, ── C1.

Fig.6.5-a: Symmetric half cavity shape and parameters.

Fig. 6.5-b: Variation of E_{pk}/E_{acc} and B_{pk}/B_{acc} with the wall angle.

Fig. 6.6 Variation of E_{pk}/E_{acc} and B_{pk}/E_{acc} with iris ellipse ratio.

Fig. 6.7 Variation of shunt impedance with the wall angle.

Fig. 6.8 (a)Drawing of the 1050 MHz, β=0.49 cavity, (b) Electrical field distribution in TM_{010} mode, (c) Magnetic field distribution in TM_{010} mode.

Fig. 6.9 (a) Schematic of the forming die for the 1050 MHz, 4mm thick cavity, (b) Different parts of the forming die.

Fig. 6.10 Q_0 vs E_{acc} in TM_{010} mode of 1050 MHz, β = 0.49 fine grain single cell cavity.

Fig.6.10-a : Block diagram of the LLRF for the cavity testing

Fig.6.10-b Photograph of the LLRF system for the cavity test.

Fig. 6.11 Q_0 vs E_{acc} in TM_{010} mode of 1050 MHz, β = 0.49 large grain single cell cavity.

Fig. 6.12 R_s vs 1/T for TM_{010} mode of the cavity. Data points are fitted with BCS theory plus residual resistance (solid line fit curve).

Fig. 6.13 Radiation Pressure on Cavity wall at 5 MV/m accelerating gradient.

Fig. 6.14 Resonant frequency variation with $Eacc^2$.

Fig. 6.15 variation of $R_s - R_{s0}$ with B_p/B_C at 2 and 1.75K of the large grain cavity. Solid lines are fitted with Eqn.6.3.

Fig. 6.16 variation of $R_s - R_{s0}$ with B_p/B_C at 2K of the fine grain cavity. Solid lines are fitted with Eqn.6.5.

LIST OF TABLES

Chapter 1

Basics of Superconductivity and Superconducting Radio Frequency Cavity

1.1. Basics of Superconductivity

1.1.1 Introduction

Superconductivity is a class of phenomenon exhibited by a family of materials which are characterized by zero DC resistance , perfect diamagnetism and an energy gap of width 2Δ centered around the Fermi energy. It was discovered by Kamerlingh-Onnes in 1911 in mercury (Hg), having Tc = 4.2K [1]. The electrical resistivity of a metallic conductor decreases gradually as the temperature is lowered. In ordinary conductors, such as copper or silver, this decrease is limited by impurities and other defects. Even near absolute zero, a real sample of a normal conductor shows some resistance. In a superconductor, the resistance drops abruptly to zero when the material is cooled below its critical temperature. An electric current flowing in a loop of superconducting wire can persist indefinitely with no power source [2]. In 1986, it was discovered that some cuprate-perovskite ceramic materials have a critical temperature above 90 K (−183 °C) [3]. Such a high transition temperature is theoretically impossible for a conventional superconductor, leading the materials to be termed high-temperature superconductors. In conventional superconductors, electrons are held together in pairs by an attraction mediated by lattice phonons. The best available model of high-temperature superconductivity is still somewhat crude. There is a hypothesis that electron pairing in high-temperature superconductors is mediated by short-range spin waves known as paramagnons [4]. When the superconductor is placed in a weak external magnetic

field **H**, and cooled below its transition temperature, the magnetic field is ejected. The German physicists Walther Meissner and Robert Ochsenfeld discovered the phenomenon in 1933 by measuring the magnetic field distribution outside superconducting tin and lead samples [5]. The Meissner effect does not cause the field to be completely ejected but instead the field penetrates the superconductor only to a very small distance, characterized by a parameter λ, called the London penetration depth [6], decaying exponentially to zero within the bulk of the material. The Meissner effect is a defining characteristic of superconductivity. For most superconductors, the London penetration depth is on the order of 100 nm. A superconductor with little or no magnetic field within it is said to be in the Meissner state. The Meissner state breaks down when the applied magnetic field is too large. Superconductors can be divided into two classes according to how this breakdown occurs. In Type I superconductors as shown in Fig.1.1, superconductivity is abruptly destroyed when the strength of the applied field rises above a critical value H_c.

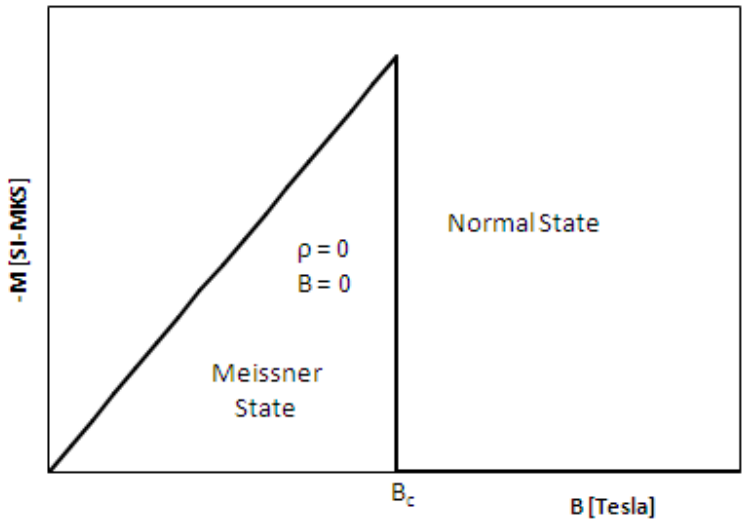

Fig. 1.1 Variation of magnetization with applied magnetic field in Type – I superconductor

In Type II superconductors as shown in Fig. 1.2, raising the applied field past a critical value H_{c1} leads to a mixed state (also known as the vortex state) in which an increasing amount of magnetic flux penetrates the material, but there remains no resistance to the flow of electric current as long as the current is not too large. At second critical field strength H_{c2}, superconductivity is destroyed.

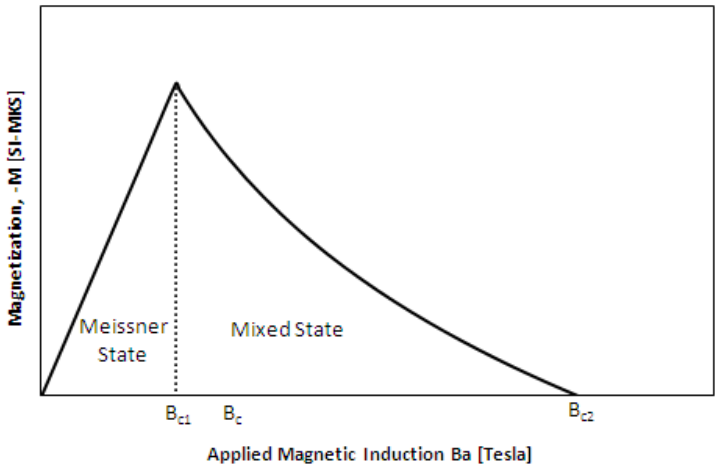

Fig.1.2 Variation of magnetization with applied magnetic field in Type-II superconductor

The onset of superconductivity is accompanied by a discontinuous jump in electronic specific heat [7] and thereafter ceases to be linear. At low temperatures, it varies instead as $e^{-\alpha/T}$ for some constant, α. This exponential behavior is one of the evidence for the existence of the energy gap. Experiments [8-10] indicate that the transition is of second-order, meaning there is no latent heat. The thermal conductivity in superconducting state is greatly reduced because the electrons which have condensed into cooper pairs do not take part in any energy transport. Also the fraction of normal electrons which are responsible for the heat transport reduces exponentially as the temperature goes down below the transition temperature.

1.1.2 Critical fields in Superconductor

Below the critical temperature T_c in a superconductor the normal electrons condense into Cooper pairs. Therefore below the transition temperature the free energy of the superconducting state must be less than that of the normal state; otherwise the metal would remain normal. When an external DC magnetic field is turned on, supercurrents flow in the penetration depth to cancel out the field in the interior. Suppose that at temperature T ($T<T_c$), and in the absence of an applied magnetic field (Ha = 0), the Gibbs free energy per unit volume of the superconducting state is $g_s(T,0)$ and that of the normal conducting state is $g_n(T,0)$ (Fig. 1.3).

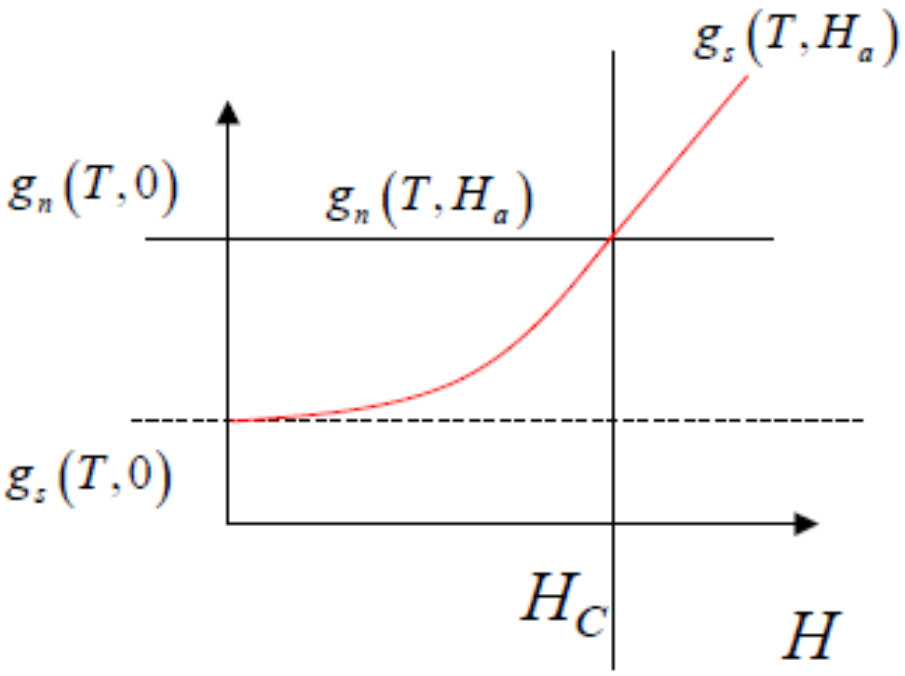

Fig.1.3 Gibbs free energy diagram in superconducting and normal conducting phase.

Now let a magnetic field *Ha* is applied parallel to the specimen. Any substance which is in an applied field H_a acquires a magnetization *M*, and changes in free energy per unit volume by an amount,

$$\Delta g\left(H_a\right) = -\mu_0 \int_0^{H_a} M dH_a \tag{1.1}$$

In case of superconducting specimen the application of magnetic field produces a negative magnetization, M=-H. The free energy per unit volume is therefore increased to,

$$g_s\left(T,H\right) = g_s\left(T,0\right) + \mu_0 \int_0^{H_a} \left|M\right| dH_a \tag{1.2}$$

In fact $\left|M\right| = H$, so the magnetic field raises the free energy density to,

$$g_s\left(T,H\right) = g_s\left(T,0\right) + \mu_0 \frac{H_a^2}{2} \tag{1.3}$$

When the external field rises to a value H_c so that the free energy of the superconducting state becomes equal to the normal conducting state, all the flux enters the superconductor. The critical magnetic field strength is given by,

$$H_c\left(T\right) = \left\{ \frac{2}{\mu_0} \left[g_n\left(T,0\right) - g_s\left(T,0\right) \right] \right\}^{\frac{1}{2}} \tag{1.4}$$

1.1.3 Phenomenological Theory

The principle phenomenological theories preceded the BCS microscopic theory [11] is no less useful for being phenomenological and incomplete. The BCS theory is based on an

idealized model, but nevertheless has been broadly successful in explaining the properties of real superconductors.

1.1.3.1 Two-Fluid Model

Gorter and Casimir in 1934 [12] introduced one of the simplest phenomenological theory of superconductivity based on the assumption that in the superconducting state there are two components of conduction electrons "fluids". One, called the superfluid component, is an ordered condensed state with zero entropy, hence is incapable of transporting heat. The other component, the normal component, is composed of electrons which behave exactly as they do in the normal state. This model states that in the superconducting state a fraction N_n of the electrons is in the normal phase and the remaining $(1\text{-}N_n)$ is in the superfluid state. The free energy of the system as a function of N_n and T is written as,

$$G_n\left(N_n,T\right)=N_n^{1/2}g_n\left(T\right)+\left(1-N_n\right)g_s\left(T\right) \tag{1.4}$$

Where, $g_n\left(T\right)=-\frac{1}{2}\gamma T^2$ and $g_s\left(T\right)=-g_0=-\frac{B_c^2\left(0\right)}{2}\mu_0$

Here g_n and g_s are the contributions to the free energy in the normal and superconducting state respectively, g_s is assumed to be independent of temperature and denotes the condensation energy gained by the electrons in the superconducting phase. Minimization of free energy leads to a relationship of the fraction of normal conducting electrons with the temperature given by $N_n=\left(\frac{T}{T_c}\right)^4$.

Thus at $T = 0$, $N_n=0$, hence all the electrons are superconducting while at $T = T_c$, $N_n=1$ so all of them are in the normal state as expected.

1.1.3.2 London Theory

The macroscopic formulation of the electrodynamics of the superconducting phase was first proposed by F. and H. London [13]. This phenomenological model is based on the two fluid model. Consider $n_s(T)$ to be the superconducting electron density at any temperature T ($T < T_c$). These superconducting electrons are freely accelerated by an electric field. If v_s is the superfluid velocity, then the equation of motion is written as,

$$m\frac{dv_s}{dt} = eE \tag{1.5}$$

One can define a superconducting current density

$$J_s = n_s e v_s \tag{1.6}$$

which obeys the following equation

$$\frac{dJ_s}{dt} = \frac{n_s e^2}{m} E \tag{1.7}$$

In the normal phase, the current density in the steady state is given by,

$$J_n = \frac{n_s e^2 \tau}{m} E = \sigma_n E \tag{1.8}$$

Where τ is the relaxation time and σ_n is the conductivity in normal state.

Taking curl of both sides of eq. (1.7), we have

$$\frac{d}{dt}\nabla\times J_s = \frac{n_s e^2}{m}\nabla\times E \tag{1.9}$$

From Maxwell's equation, since the displacement *D* inside the superconductor vanishes, one obtains

$$\nabla\times E = -\frac{dB}{dt} \tag{1.10}$$

$$\nabla\times B = \mu_0 J \tag{1.11}$$

From eqs. (1.9), (1.10) and (1.11), one obtains

$$\nabla^2 B = \frac{1}{\lambda_L^2} B \tag{1.12}$$

Where $\lambda_L = \left(\frac{m}{n_s e^2 \mu_0}\right)^{1/2}$ is a characteristic length scale known as the London penetration depth. This measures the extension of the penetration of the magnetic field inside the superconductor. It may be remarked that the decay of magnetic field in real superconductors deviates considerably from the exponential law. A more general definition

$$\frac{1}{\lambda_L} = \frac{1}{B(0)}\int_0^\infty B(x)dx \tag{1.13}$$

Pippard[14] and Faber Pippard [15] proposed a series of experiments to demonstrate, that the super current density J_s responds non locally to an applied vector potential *A*, introducing the concept of a "coherence length" ξ to characterize the distance over which this nonlocal

response occurs. In a clean superconductor, for which the mean free path length l_e of the normal electrons is sufficiently long, the intrinsic coherence length ξ_0 varies inversely with T_c, i.e. $\xi_0 = \frac{a\hbar v_F}{k_B T_c}$. In dirty superconductor or type II superconductors, for which $l_e \ll \xi_0$, the total coherence length is given by

$$\frac{1}{\xi} = \frac{1}{\xi_0} + \frac{1}{\ell_e} \tag{1.14}$$

where ξ_0 is the BCS coherence length.

1.1.3.3 Ginzburg- Landau (GL) Theory

Ginzburg and Landau [16], proposed in 1950 a highly, innovative phenomenological theory of superconductivity based on Landau's theory of phase transitions. The linear London equations are applicable with the limitation of current density $J_s << J_d$ (depairing current density) and superfluid density n_s spatially uniform. Ginzburg and Landau generalized the London equations to account for nonlinear problems. Lots of important phenomena in superconductivity occur because n_s is nonuniform. They have introduced the complex superconducting order parameter $\Psi = (ns/2)^{1/2} exp(i\theta)$ (envelope wave function of the Cooper pair). In normal state Ψ is zero. At T≈ T_c, where the superconductivity is weak and Ψ is small, and the free energy F can be expanded in Taylor series in Ψ,

$$F = F_n + \int dV \left| \alpha(T) |\Psi|^2 + \frac{\beta}{2} |\Psi|^4 + \frac{\hbar^2}{2m^*} \left| \left(\nabla + \frac{2\pi i \vec{A}}{\phi_0} \right) \Psi \right|^2 + \frac{\mu_0 H^2}{2} \right|$$

(1.15)

nonlinear inhomogeneity magnetic

We can easily see that if the order parameter does not vary in space, one obtains back exactly the London free energy and London equation by carrying out the minimization.

Equation (1.15) introduces, ab initio, two phenomenological parameters, α and β, into the free energy expression. The third term inside the integral takes into account the spatial inhomogeneity of the wave function Ψ in a nonzero magnetic field and the last term is due the free energy in a magnetic field. From Landau theory, we have $\alpha(T) = \alpha_0 (T - T_c)/T_c$ and β is positive constant independent of *T*. Energy minimization conditions $\delta F/\delta \Psi = 0$and $\delta F/\delta A = 0$ yield the GL equations for the dimensionless order parameter $\Psi = \Psi/\Psi_0$.

$$\xi^2 \left(\nabla + \frac{2\pi i}{\phi_0} \vec{A} \right)^2 \psi + \psi - \psi \, |\psi|^2 = 0 \tag{1.16}$$

$$\nabla \times \nabla \times \vec{A} = \vec{J}_s = -\frac{|\psi|^2}{\lambda^2 \mu_0} \left(\frac{\phi_0}{2\pi} \nabla \theta + \vec{A} \right) \tag{1.17}$$

Equations (1.16) and (1.17) are two coupled complex nonlinear partial differential equation for the pair wave function Ψ (r) and the magnetic vector potential A(r). They contain two fundamental lengths ξ andλ, which will be explained shortly. The correlation between the wave function and the change in free energy in normal and superconducting phase is shown in Fig.1.4.

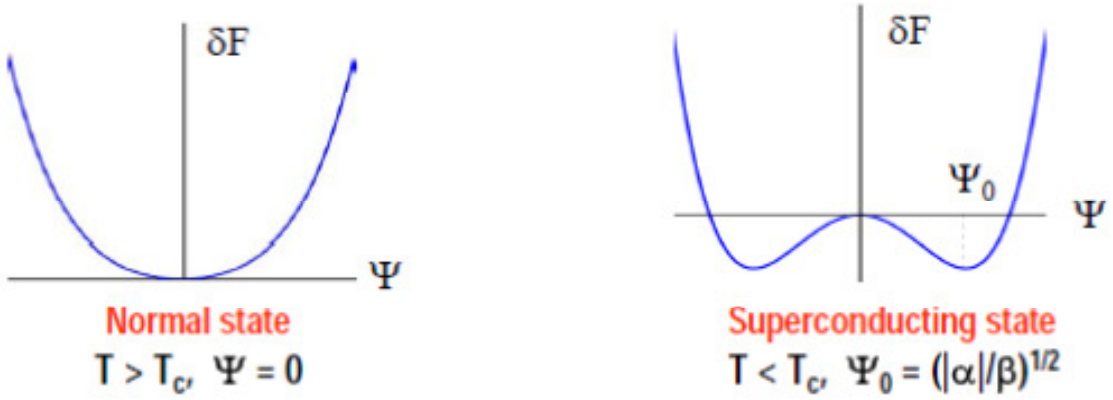

Fig.1.4 Change in free energy with complex order parameter in normal and superconducting phase [17].

1.1.3.3.1 Consequences of GL Equations

1.1.3.3.1.A Thermodynamic critical field:

For a homogeneous order parameter with no magnetic field the minimization of free energy with respect to the order parameter in eqn. (1.15) gives $|\Psi_0|^2 = -\alpha/\beta$. The Gibb's free energy difference in normal and superconducting phase is $\frac{1}{2}\mu_0 H_c^2$. Thus

$$F_n - F_s = V\frac{\alpha^2(T)}{2\beta} = V\frac{\mu_0 H_c^2(T)}{2} \tag{1.18}$$

It shows a linear temperature dependence of $H_c(T)$ near T_c as shown in Fig.1.5,

$$H_c(T) = \frac{\alpha_0}{\sqrt{\beta\mu_0}}\frac{(T_c - T)}{T_c} \tag{1.19}$$

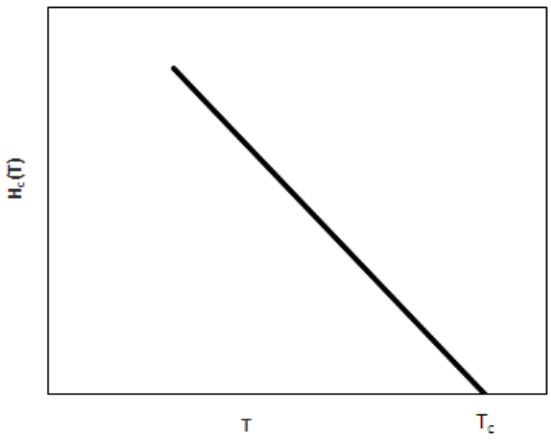

Fig.1.5 Linear variation of $H_c(T)$ near T_c

1.1.3.3.1.B Magnetic London Penetration depth[13]

In case of small applied magnetic field and assuming no variation in Ψ one obtains the London equation with magnetic London penetration depth defined by,

$$\lambda(T) = \left(\frac{m\beta}{2e^2\mu_0\alpha_0}\right)^{1/2} \sqrt{\frac{T_c}{T_c - T}} \tag{1.20}$$

The variation of penetration depth with temperature is shown in Fig.1.6.

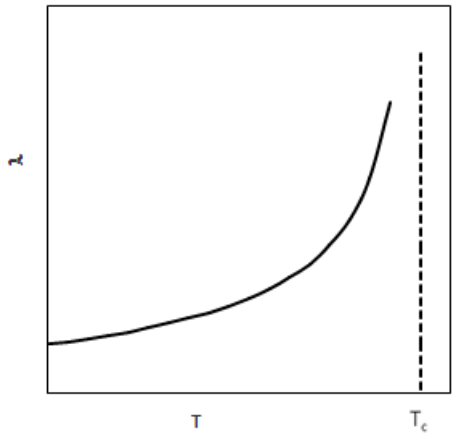

Fig.1.6 Variation of penetration depth with temperature ($T \leq T_c$)

1.1.3.3.1.C Coherence length[14]

The GL eqn. (1.6) in absence of external magnetic field defines a length scale of spatial variation of superfluid density ns(r) and it is defined by the following equation,

$$\xi(T) = \left(\frac{\hbar^2}{4m\alpha_0} \right)^{1/2} \sqrt{\frac{T_c}{T_c - T}} \tag{1.21}$$

We can see that this length like the penetration depth λ also diverges when $T \rightarrow T_c$ as $\alpha \rightarrow 0$. The variation of ξ with temperature is shown in Fig.1.7.

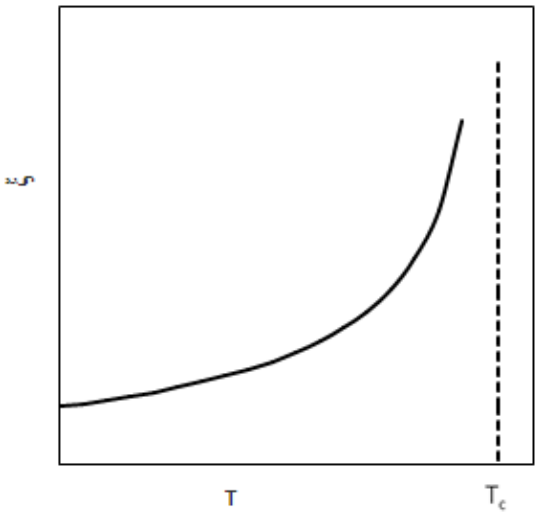

Fig.1.7 Variation of coherence length ξ with temperature ($T \leq T_c$)

1.1.3.3.1.D GL parameter[16]

The properties of superconductors depend sensitively on the ratio of the penetration depth λ to the coherence length ξ. It is convenient to define a dimensionless parameter, $\kappa = \lambda/\xi$ which is nearly independent of temperature. k is called the Ginzburg-Landau parameter. The value of the

GL parameter determines whether the superconductor will behave as Type-I or Type-II. The relationship between the 2nd critical field B_{C2} with the thermodynamic critical field B_C is given by,

$$B_{c2} = k\sqrt{2}B_c \tag{1.22}$$

i) If $k \equiv \lambda/\xi < 1/\sqrt{2}$, we have $B_{c2} < B_c$. Obviously, by decreasing the magnetic field the superconducting state appears below B_c with total expulsion of flux lines and hence a Type-I superconductor.

ii) If $k \equiv \lambda/\xi > 1/\sqrt{2}$, we have $B_{c2} > B_c$. The superconducting state appears below B_{c2} with partial expulsion of flux lines and hence a Type-II superconductor.

1.1.3.3.1.E Upper Critical Field (B_{c2})

Type-II superconductors show a second order phase transition at B_{c2}. For a second order phase transition the order parameter is small. For a uniform field B along the z axis, the GL equation 1.16 for small ψ takes the form,

$$\xi^2\nabla^2\psi + \left[1 - \left(2\pi Bx\xi/\phi_0\right)^2\right]\psi = 0 \tag{1.23}$$

The Schrodinger equation for a harmonic oscillator is given by,

$$\frac{\hbar^2}{2M}\nabla^2\psi + \left(E - \frac{M\omega^2x^2}{2}\right)\psi = 0 \tag{1.24}$$

where M = Mass of the oscillator, ω = angular frequency of the oscillator, *x*= displacement of the oscillator.

Comparing equation (1.23) and (1.24) gives,

$$\frac{\hbar^2}{2M} \to \xi^2, \quad E \to 1, \quad \sqrt{M}\,\omega \to \frac{2^{3/2}\pi B\xi}{\phi_0} \tag{1.25}$$

The lowest eigenvalue of the oscillator's energy spectrum gives the B_{C2} below which bulk superconductivity exists,

$$B_{c2}(T) = \frac{\phi_0}{2\pi\xi^2(T)} = \frac{\phi_0}{2\pi\xi_0^{\,2}}\left(1-\frac{T}{T_c}\right) \tag{1.26}$$

In case of dirty superconductor i.e. for which the electron mean free path $\ell < \xi_0$, the B_{C2} increases proportional to the residual resistivity ρ and is given by,

$$B_{c2}(T) \cong \frac{\phi_0}{2\pi\xi_0\ell}\left(1-\frac{T}{T_c}\right) \propto \rho \tag{1.27}$$

1.1.3.3.1.F Lower Critical Field (B_{c1})

The lower critical field B_{c1} corresponds to the thermodynamic limit above which it is energetically favorable for vortices to penetrate into the superconductor. Each vortex carries a paramagnetic flux quanta, so the vortex self energy in a magnetic field *H* is reduced by $H\Phi_0$. The Gibb's free energy per unit length of the vortex line is given by,

$$G = \varepsilon - H\phi_0 \tag{1.28}$$

where, ε is the vortex self energy, H and Φ_0 are having the usual meaning as described earlier. The single vortex core is described by a tubular structure in a superconductor which is having a small core region of characteristic length ξ over which the order parameter ψ is suppressed. It has also a circulating supercurrent over the characteristic length of λ from the vortex core and each vortex carries a flux quantum of Φ_0. The vortex self energy is given by,

$$\varepsilon \cong \frac{\lambda^2}{2\mu_0}\left(\frac{\phi_0}{2\pi\lambda^2}\right)^2 \int_{\xi}^{\lambda} \frac{2\pi r}{r^2} dr = \frac{\phi_0^2}{4\pi\mu_0\lambda^2} \ln\frac{\lambda}{\xi} \tag{1.29}$$

The vortices are energetically favorable for G<0 and lead to the condition,

$$H > H_{c1} = \frac{\varepsilon}{\phi_0} \tag{1.30}$$

Using equation (1.29) in (1.30) one finally obtains,

$$B_{c1} = \frac{\phi_0}{4\pi\lambda^2}\left(\ln\frac{\lambda}{\phi_0} + 0.5\right) \tag{1.31}$$

The factor 0.5 in the parenthesis of equation 1.30 appears due the hexagonal vortex lattice arrangement in the superconductor.

1.1.3.3.1.G Surface Critical Field (B_{c3})

The solution of GL equations is strictly valid only for an infinite sample. In case of a semi infinite sample in the half space x > 0 and the applied magnetic field is parallel to the sample surface, the solution of linearized GL equation with the additional boundary condition that there is no current perpendicular to the surface of the sample is given by Saint-James and de Gennes

[18] They find that $B_{c3} = 2.39kB_{c2}$ where k is the Ginzburg-Landau parameter. For Type II superconductors ($k > 1/\sqrt{2}$) this relation becomes $B_{c3} = 1.69B_{c2}$.

For a Type-II superconductor if the applied field is $B_{c2} < B < B_{c3}$, there exists a surface sheath of thickness ~ ξ in which the sample is still superconducting. In a long cylindrical sample with the applied field parallel to the axis of the cylinder the sheath will cover all the surface of the cylinder [18].

1.2 Basics of Superconducting Radio Frequency Cavity (SCRF)

1.2.1 RF Cavity Definition

The RF cavity is a metallic enclosure having opening for beam passage and supports a particular electromagnetic mode of interest (TM_{010}) for the acceleration of the charged particle beam during the passage through the cavity.

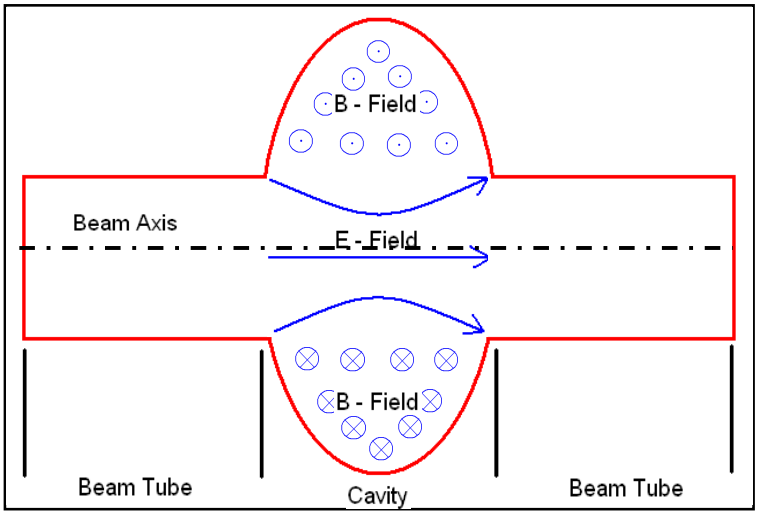

Fig.1.8 Typical single cell cavity geometry with field lines of TM_{010} mode and also shows the particle acceleration direction.

When microwave power is filled inside the cavity structure the electric and magnetic field distribution for accelerating TM_{010} mode is shown in Fig.1.8.

The eigenmodes and the field distributions of the RF cavity shown in Fig.1.8 are obtained from that of a circular waveguide by imposing additional boundary conditions at the closed ends [19]. The need for axial electric field (E_z) for beam acceleration means that only the TM_{nml} modes are of interest, where the indices *n*, *m*, and *l* are associated with the azimuthal, radial and axial degrees of freedom, respectively. The cavity modes are labelled as monopole ($n = 0$), dipole ($n = 1$), quadrupole ($n = 2$), *etc.*, according to their degrees of azimuthal variation. The first TM mode, while cavity radius '*a*' is bigger than the cavity length ℓ, is the TM_{010} which has a resonant frequency (independent of ℓ).

$$f_0 = 2.405\frac{c}{2\pi a} \tag{1.32}$$

Therefore, the operation frequency should be chosen so this mode is the only one to appear and no other modes which could affect the particles trajectory are created in nearby frequency range. The TM_{010} mode has strong electric field along the cavity axis which is ideally suited for beam acceleration. Thus, the individual cells of accelerating structures usually operate in this mode.

1.2.2 RF Cavity Figures of Merit

1.2.2.1 Accelerating Voltage

The longitudinal electric field accelerates or decelerates a particle depending on the particle phase with respect to the RF. The voltage gained by the particle across the gap is given by [20],

$$V_c = \left| \int_0^{\ell} E_z\left(\rho = 0, z\right) e^{i\omega_0 z/c} dz \right| \tag{1.33}$$

where ℓ is the cavity length, and ω_0 is the frequency of the mode. The particle takes a finite time to traverse the cavity, leading to a reduction in energy gain which is characterized by a transit time factor

$$T = \frac{\int_0^{\ell} E_0 e^{i\omega_0 z/c} dz}{\int_0^{\ell} E_0 dz} \tag{1.34}$$

1.2.2.2 Stored Energy

For each mode in the cavity, the time averaged energy in the electric field is equal to that in the magnetic field. The stored energy is given by a volume integral

$$U = \frac{1}{2}\varepsilon_0 \int_{\upsilon} \left|\overrightarrow{E^2}\right| d\upsilon = \frac{1}{2}\mu_0 \int_{\upsilon} \left|\overrightarrow{H^2}\right| d\upsilon \tag{1.35}$$

1.2.2.3 Surface Resistance and Power Dissipation

Since, real metals have finite conductivity, RF fields at sufficiently high frequencies penetrates a finite depth into the conductor. The current density is exponentially decreasing into the metal. The surface impedance of the metal is given by,

$$R_s = \sqrt{\frac{\mu\omega}{2\sigma}} \tag{1.36}$$

where, δ is known as the skin depth which is defined as,

$$\delta = \sqrt{\frac{2}{\mu\omega\sigma}} \tag{1.37}$$

The power dissipated in the cavity walls due to the surface resistance is given by the surface integral,

$$P_c = \frac{1}{2} R_s \int_S \left| \overrightarrow{H^2} \right| ds \tag{1.38}$$

1.2.2.4 ***Quality Factor***

The stored energy in the cavity decays exponentially

$$U(t) = U_0 e^{-t/\tau} \tag{1.39}$$

where τ is the characteristic time constant dependent on the material. This figure of merit can also be expressed in terms of a quality factor, which is related to the power dissipation and is defined as

$$Q_0 = \frac{\omega_0 U}{P_c} \tag{1.40}$$

where U is the stored energy and P_c is the power dissipated in the cavity walls. The Q_0 is roughly 2π time the number of rf cycle it takes to dissipate the energy stored in the cavity.

1.2.2.5 ***Geometric Factor and Shunt Impedance***

The quality factor Q0 defined in equation (1.40) can be rewritten using equation (1.35) and (1.38) as [20],

$$Q_0 = \frac{\omega_0 \mu_0 \int_V \left| \overrightarrow{H^2} \right| d\upsilon}{R_s \int_S \left| \overrightarrow{H^2} \right| ds} \tag{1.41}$$

The Q0 is frequently written as,

$$Q_0 = \frac{G}{R_s} \tag{1.42}$$

where

$$G = \frac{\omega_0 \mu_0 \int_V \left|\overrightarrow{H^2}\right| d\upsilon}{\int_S \left|\overrightarrow{H^2}\right| ds} \tag{1.43}$$

is known as the geometry constant. The factor $\int_V \left|\overrightarrow{H^2}\right| d\upsilon \Big/ \int_S \left|\overrightarrow{H^2}\right| ds \propto a \propto \frac{1}{\omega_0}$ [21]. Using this fact in equation (1.43) we see that the geometry factor depends on the cavity shape but not its size. The parameter G therefore is very much useful for comparing different cavity shapes, irrespective of their size and wall materials.

Another figure of merit of a cavity which is the shunt impedance given by,

$$R_a = \frac{V_c^{\,2}}{P_c} \tag{1.44}$$

which measures the efficiency the accelerating voltage for given dissipation. A more meaningful quantity is the ratio of shunt impedance to the quality factor

$$\frac{R_a}{Q_0} = \frac{V_c^{\,2}}{\omega U} \tag{1.45}$$

This quantity is independent of the cavity material and the field amplitude and is a measure of the efficiency of the accelerating voltage for a given stored energy.

1.2.3 RF Superconductivity

1.2.3.1 RF Critical Magnetic field

In the absence of any external magnetic field the normal to superconducting state phase transition is of second order. Whereas in the presence of external magnetic field it is a first order phase transition associated with the latent heat and it requires nucleation centers. Depending

upon the nucleation centers available a metastable superheated superconducting state ($H>H_c$) or a subcooled normalconducting ($H<H_c$) state can appear [22].

In case of Type-II superconductor which is of our interest for the present thesis, it is possible for the Messsiner state to persist metastably above Hc1. The dependence of superheating critical field with the GL parameter k has been calculated numerically by solving the GL equations and the dependence is shown in Fig.1.9. The derived analytical expressions for different k value are shown below [23,24,21],

$$H_{sh} \approx \frac{0.89}{\sqrt{k}} H_c, k << 1,$$

$$H_{sh} \approx 1.2 H_c, k \approx 1, \tag{1.46}$$

$$H_{sh} \approx 0.75 H_c, k >> 1.$$

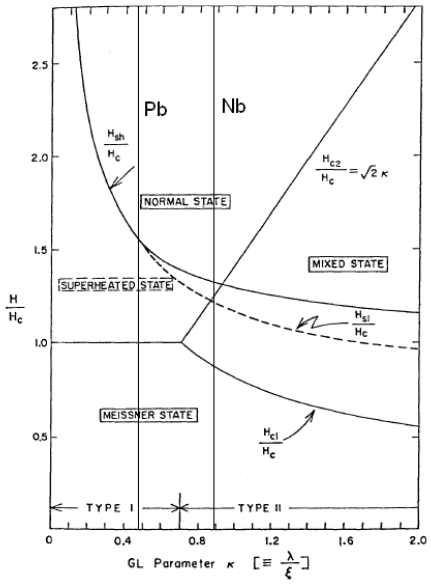

Fig.1.9 Phase diagram of the superconductor for the Meissner, superheated, mixed and normal state [21].

1.2.3.2 Microwave surface resistance

1.2.3.2.1 BCS resistance

Based on BCS theory [11], the superconducting electrons, which are Cooper pairs below T_c, shield the normal conducting electrons from the electromagnetic field so that no power is dissipated. But, for alternating current at microwave frequencies, since RF surface resistance is zero only at T = 0K, the Cooper pairs have inertia and thus only imperfectly shield the applied field. Accordingly, the time-varying electric field can accelerate or decelerate the normal electrons, leading to power dissipation and a resistance which depends on the density of normal conducting electrons and the frequency of the alternating current. For temperatures $T < T_c/2$, the superconducting BCS [25] surface resistance can be well described by,

$$R_{BCS}(T,f) = A\frac{f^{f}}{T}\exp\left(\frac{-\Delta(0)}{K_B T}\right) \tag{1.47}$$

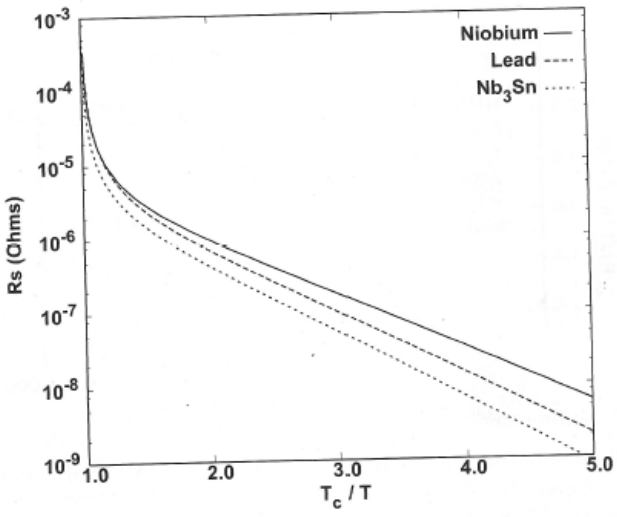

Fig.1.10 Theoretical surface resistance at 1.5 GHz of lead, niobium and Nb_3Sn as calculated from program [26]

where Δ is the superconducting gap, K_B is the Boltzman constant. The coefficient A is a complex function of material parameters such as the coherence length ξ_0, the electron mean free path, the Fermi velocity v_F and the London penetration depth $\lambda_L(0)$. J. Halbritter [26] has written a computer program to calculate R_{BCS} and fit the experimental results. The results of calculated R_{BCS} for niobium, lead and Nb_3Sn by Halbritter's program is shown in Fig.1.10. A convenient expression of R_{BCS} for niobium considering T<Tc/2 and f<< 1000 GHz is given by [21],

$$R_{BCS}(ohm) = 2\times10^{-4}\,\frac{1}{T}\left(\frac{f}{1.5}\right)^2 \exp\left(-\frac{17.67}{T}\right) \tag{1.48}$$

R_{BCS} is due to Joule heating of thermally activated quasi-particles by the RF electric field induced by the TM_{010} magnetic parallel to the cavity surface. For 1-2 GHz frequencies $\hbar\omega << \Delta$ of Nb cavities and the screening supercurrent density is localized in a narrow surface layer determined by the static London penetration depth $\lambda \sim 40nm$ [6]. It is therefore required to control surface impurities like grain boundaries and oxide structures within the *~10-20 nm* scales of rf field penetration in order to minimize the *R*s value in Eqn.1.48. For niobium, it is about $9\cdot10^{-5}\Omega K/(GHz)^2$. Therefore the BCS resistance at 1.3 GHz is about *600nΩ* at *4.2K* and about *10 nΩ* at *2K* [26,27].

1.2.3.2.2 Residual resistance

The experimental measurements show that the surface resistance (R_{surf}) also contains a temperature-independent term, the residual resistance R_0: $R_{surf} = R_{BCS}(T,f) + R_0$

The mechanisms that control R_0 are not well understood, though several possibilities have been proposed and investigated [21, 28-29]. The residual resistance is usually dominated by lattice

imperfections, foreign material inclusion, chemical impurities, trapped magnetic flux, adsorbed gases etc. [30-34].

1.2.3.4. Limitations in the Superconducting Niobium Cavity Performance

Presently high purity niobium is the material of choice for superconducting RF cavities. Their performance is decided by the dependence of the quality factor Q_0 with the accelerating field E_{acc}. The ideal and the practical performance of a typical SRF cavity is shown in Fig.1.11. The ideal performance of the cavity is not only governed by the field independent BCS resistance but also shows a field dependent drop and hence a Q-slope is observed until the cavity quenches at the theoretical critical magnetic field. The observed loss mechanisms within the RF penetration depth of the cavity are classified by low field losses and high field losses. In the low field regime the losses are due mainly to the residual losses. The low field losses may occur due to the flux trapping, adsorbed gases, resistive particles etc. whereas in the medium to high field regime the losses are due to multipacting barriers, thermal breakdown, field emission etc.

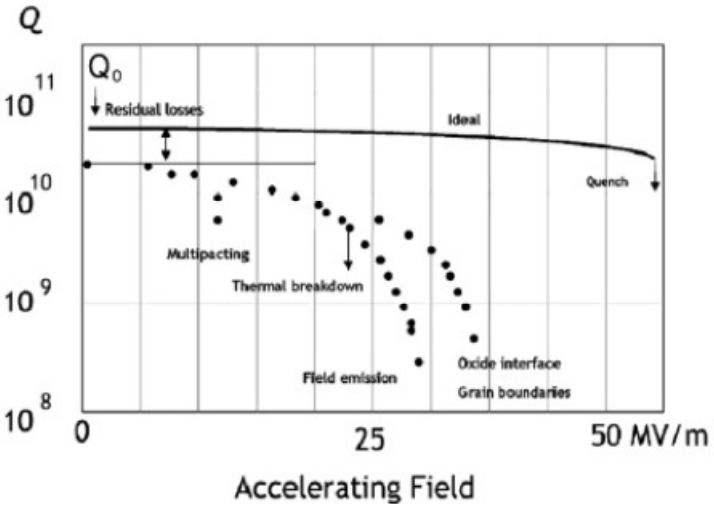

Fig.1.11 A summary of the performance limitations of an SRF cavity. The maximum theoretically expected accelerating field is 50MV/m when the surface magnetic field reaches the peak RF critical field of ~200mT for niobium. [21,35]

Chapter 2

Motivation for the Present Research

Superconducting Radio Frequency (SRF) cavity performances have been continually improved for past three decades to achieve reproducible quality factor of 10^{10} and accelerating fields (E_{acc}) of 30-35MV/m. The present approach for the fabrication of superconducting radio frequency (SRF) cavities is to roll and deep draw sheets of polycrystalline high-purity niobium. Jefferson Laboratory pioneered the use of large-grain/single-crystal Nb directly sliced from an ingot for the fabrication of single-crystal high-purity Nb SRF cavities [36].The large grain/single crystal niobium has several potential advantages over the polycrystalline niobium [37] and has become a viable alternative to the standard fine grain (ASTM grain size>6), high purity (RRR $\geq$ **250**) niobium for the fabrication of high-performance SRF cavities for particle accelerators. Single crystal or large grain material promises the following potential advantages [37]:

1. Reduced costs.
2. Comparable performance
3. Very smooth surfaces with buffered chemical polishing(BCP), no electro polishing(EP) necessary
4. Possibly elimination of "in situ" baking because of "Q-drop" onset at higher gradients
5. Possibly very low residual resistances (high Q's), favoring lower operation temperature less "cryo power" and therefore lower operating costs
6. Higher thermal stability because of "phonon-peak" in thermal conductivity

7. Good or better mechanical performance than fine grain material (e.g. predictable spring back.)

8. Less material QA (eddy current/squid scanning)

The fabrication steps for the niobium sheets in case of polycrystalline niobium and Fig.2.1 shows the steps in ingot niobium production are shown in Fig.2.1 and Fig.2.2.

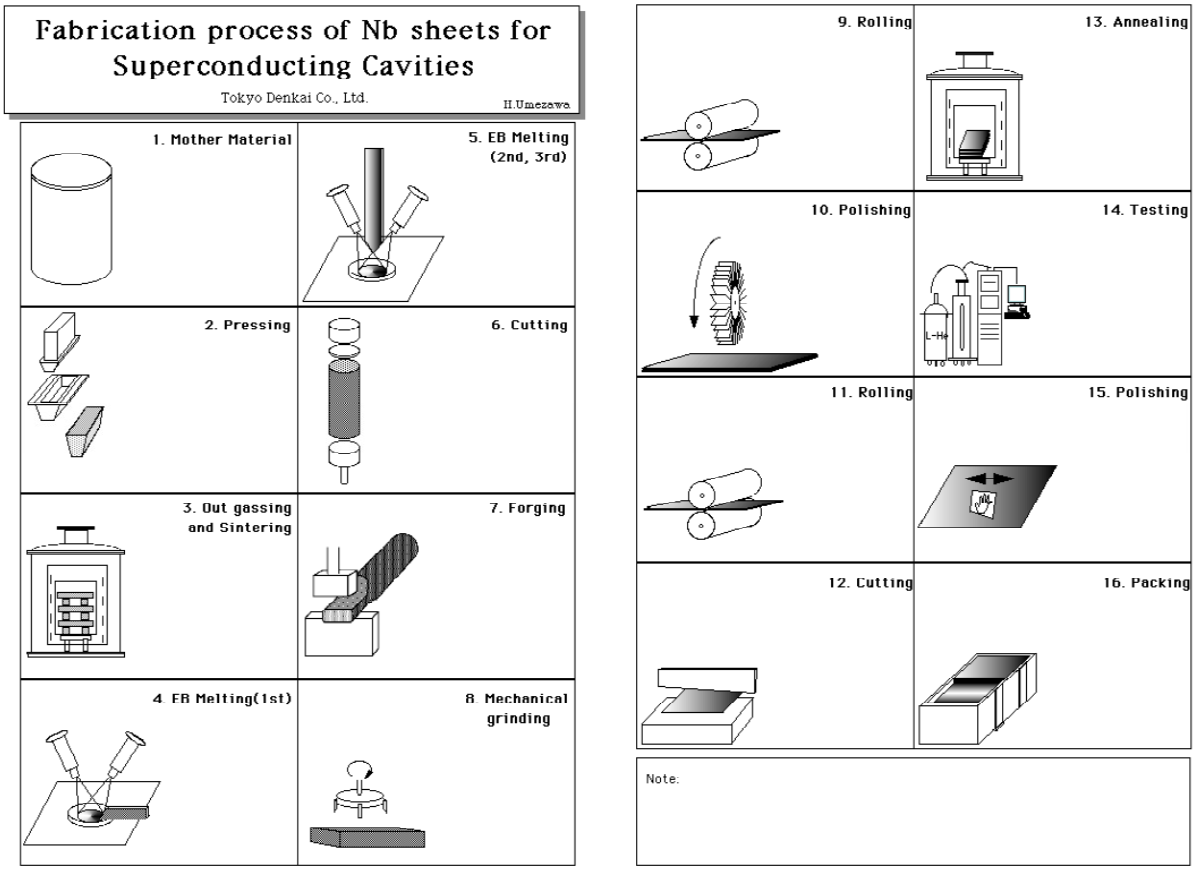

Fig.2.1: Fabrication steps of polycrystalline Niobium sheet [Courtsey: Tokyo Denkai Co. Ltd.]

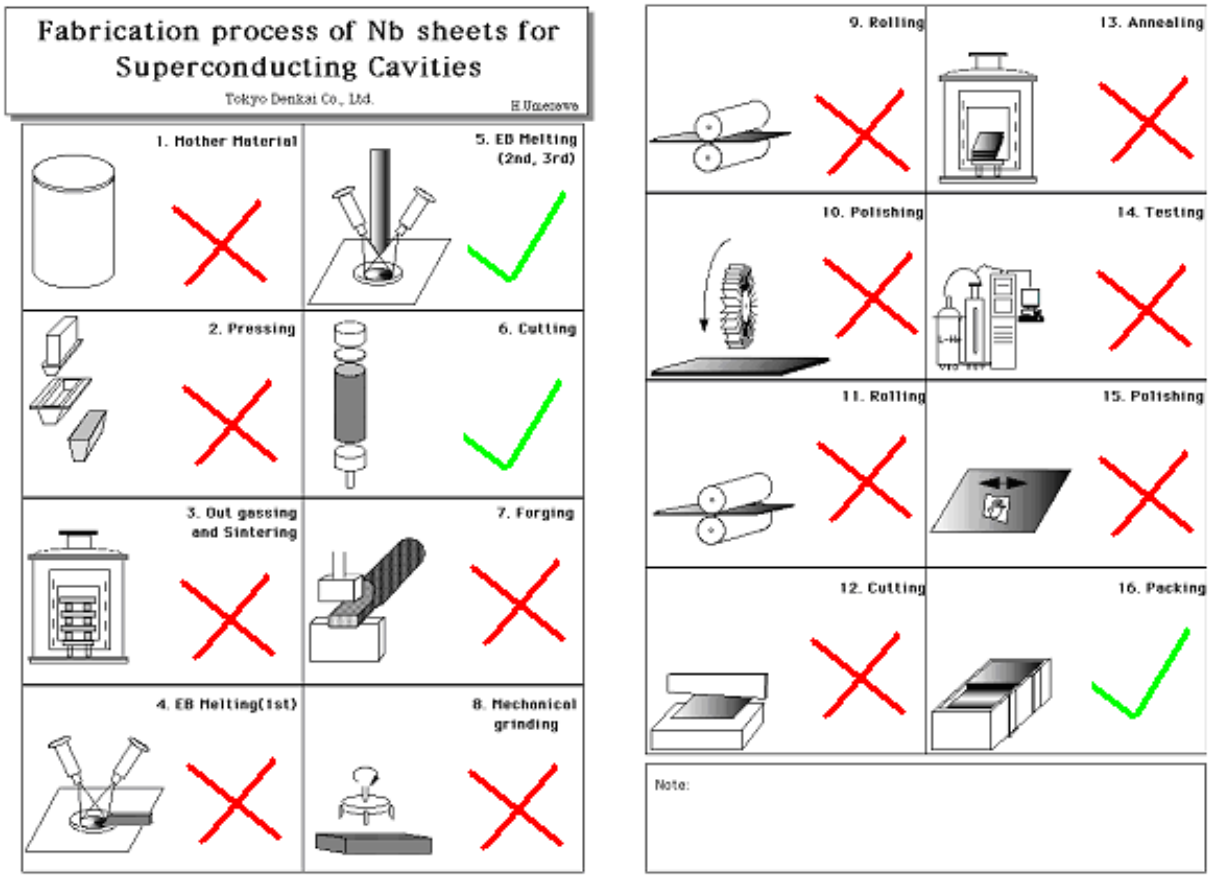

Fig.2.2: Fabrication steps of Ingot Niobium sheet

It is obvious that in case of ingot niobium all the steps are omitted except the EB melting, cutting and final packing. Hence a great reduction of cost in the sheet fabrication process is possible for the ingot niobium technology. This has motivated us to do a further study on large grain niobium.

Because of the potential advantages of large grain material, the interest in investigating material properties with different surface treatments will help to understand the cavity performance behavior with the same surface preparation.

Present day SRF cavity performance is greatly enhanced by a low temperature bake at around 120^0C. During the baking the cavity is kept connected to vacuum pump and a ultra high vacuum (UHV) is maintained inside the cavity. The in-situ baking essentially removes the high field Q-drop. The significant improvement of cavity performances after the low temperature baking is shown in Fig.2.3. [38, 39-41].

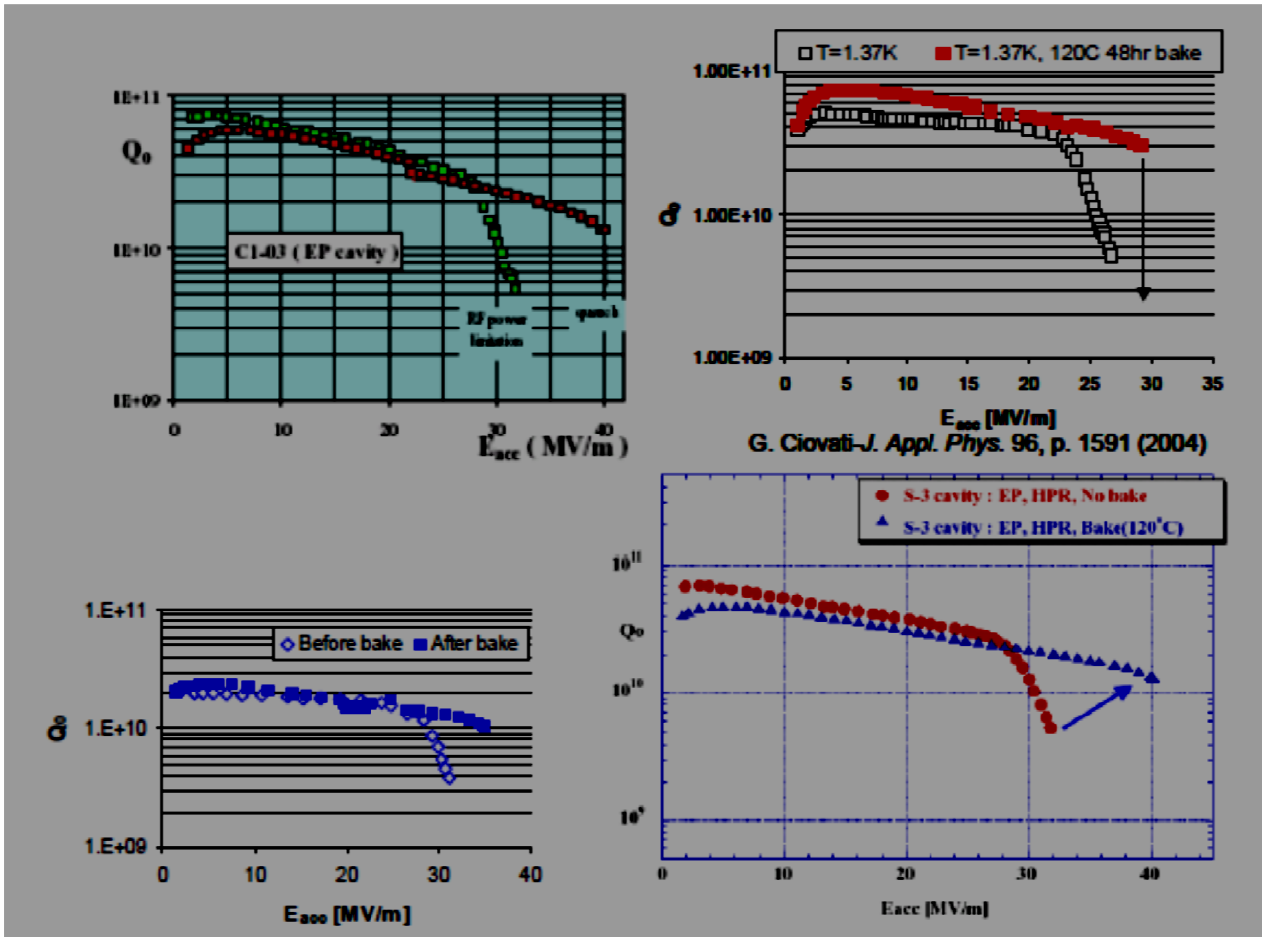

Fig.2.3 Examples of Q-drop before baking and its removal after baking. [Figure taken from P. Bauer et.al "Review of Q-drop in SRF cavities" TD-05-56, January 2006]

The baking effect on R_{BCS} is found to be a long term effect [42] and has also a saturation time after that there is no further improvement in R_{BCS} [43]. After removal of a the surface layer as thin as ~80 nm, the performance of a baked cavity restores back to that of an unbaked cavity [43,44].

In order to understand the low temperature baking effect in large grain niobium sample, we have studied the surface magnetization behaviour while varying the baking temperature from 100 – 140^0C. The recent study of AC susceptibility measurement [45, 46] shows that the B_{C3}/B_{C2} ratio changes with LTB. This motivated us to conduct a similar kind of study for large grain material.

Also the thermal conductivity of the niobium material plays an important role in SRF cavity performance. The higherthe thermal conductivity, the better is the heat removal efficiency and hence improved cavity performance. Since large grain material has less number of grain boundaries, the scattering rate of phonons with the grain boundaries is reduced. So a phonon contribution starts appearing below 3K and subsequently a phonon peak is reached. So to the first view it seems that large grain niobium cavity will have great advantage at 2K operation because of the phonon peak. It also motivated me to study the large grain niobium thermal conductivity after different surface treatment of the samples.

Finally the large grain cavities are made and their performance is evaluated in vertical test at 2K.

Chapter 3

Investigation of the Thermal Conductivity of Niobium in the Temperature Range 1.8-5 K

A cavity made of large grain or single crystal niobium operating below 2 K may have a better thermal stability due to the reduction of phonon scattering by grain boundaries (causing the so-called "phonon-peak"). Many measurements have shown that the scattering of phonons and electrons with the fluxoids decreases the observed thermal conductivity [47,48]. At low temperature (T<<Tc) ,for instance, in niobium between the temperature 1.8-3K k_{ph} montonically increases due to the decrease of scattering of phonons with the electrons. This is due to the electron decoupling resulting from the condensation into Cooper pairs. The thermal conductivity in the mixed state has been measured in previous studies [47-51]. They showed that with the increasing magnetic field in the mixed state more and more fluxoids enters the superconductor and as a result both electron and phonon mean free path (mfp) decrease.

3.1 Present Work

Present work consisted of thermal conductivity measurements of large grain niobium samples in the Meissner state and in the mixed state in the temperature range 1.8 – 5 K and for magnetic fields up to the surface critical field, H_{c3}. Also the effect of initial trapped vortices (field-cooled states) on the Meissner and mixed state conductivity of type II superconductor was studied. The results show that when the sample is cycled through Tc, with no external field applied, the sample re-gain the Meissner state and the thermal conductivity has the same value as with no trapped flux. The zero field thermal conductivity data has been fitted with the semi empirical

parametrization of *F. Koechlin and B Bonin* [52]. The results for the specimen with the trapped vortices are interpreted with phonon-vortex scattering, using the qualitative model of *Vinen et.al* [48].The thermal conductivity as function B in the mixed state is analyzed with the *Houghton-Maki* theory [58].

3.2 System Design

A system to measure the magnetization curve and the thermal conductivity of the cylindrical sample rod of diameter 6 mm and 120 mm long was designed and built. The schematic of the system and the picture of the sample rod is shown in Fig.3.1[61]. A heater made with constantan wire glued on a Cu block with Epoxy is clamped near the base of the sample. Two calibrated Cernox resistors are soldered with indium on two small Cu blocks which are clamped to the rod at a distance of about 40 mm. A pickup coil (< 200 turns, 0.29 mm diameter Cu wire) is inserted in the middle of the sample, between the two Cernox resistors. The sample is clamped on a Cu block which is inserted in a copper tube and sealed with indium wire. A stainless steel 2 ¾" Conflat flange was brazed on the other end of the tube. The tube is bolted to a "T" section where a flange with feed-through connectors is bolted on the side.

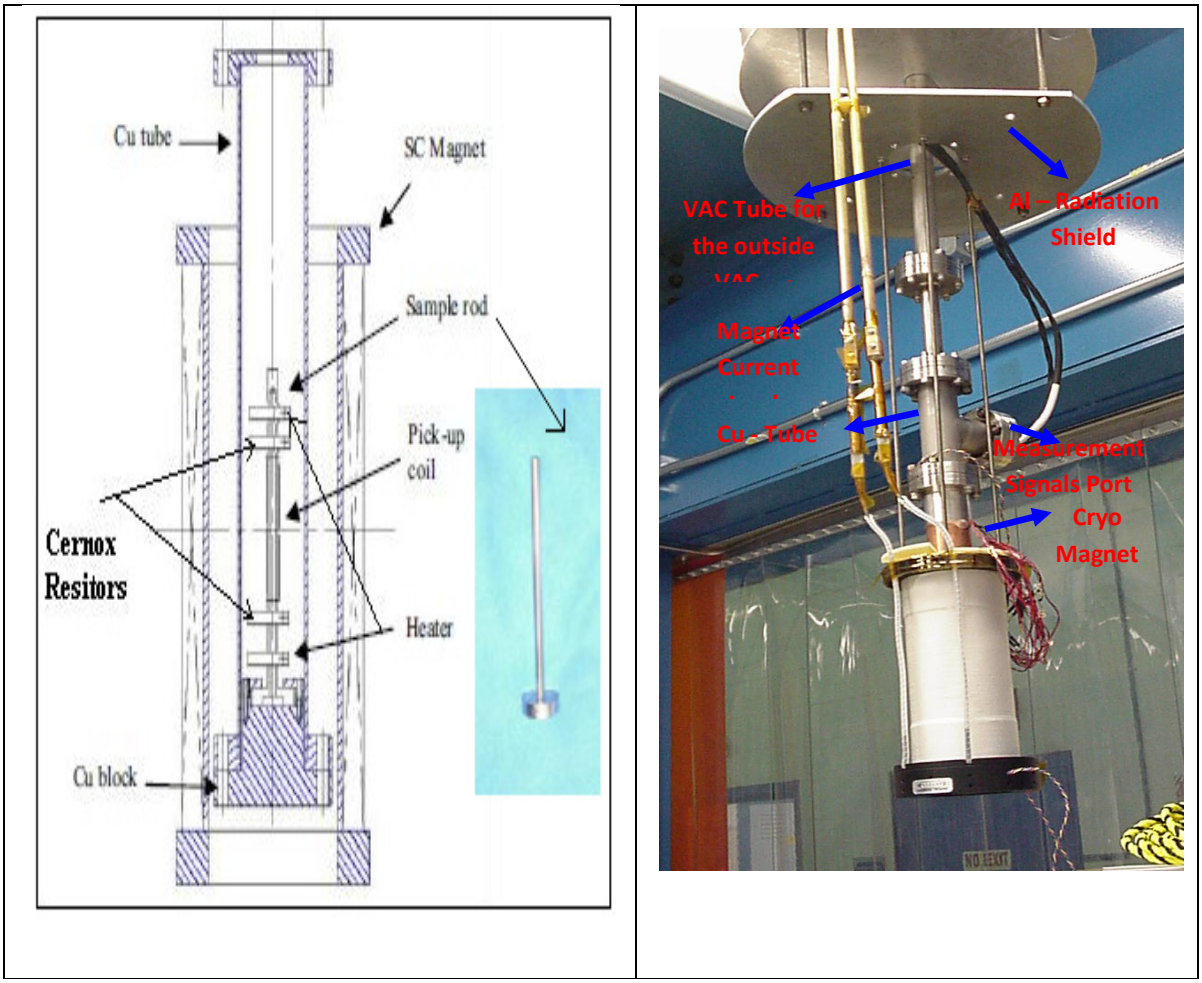

Fig.3.1 Schematic of the system (left) and the actual (right) assembled system before inserting in liquid helium dewar for measurements of superconducting properties of the sample and picture of the sample rod.

The assembly is bolted to the vacuum line on a vertical test stand (the pressure in the Cu tube is $< 10^{-5}$ mbar at 4.3 K). Some heat shields were inserted in the vacuum line to minimize radiation losses. A superconducting magnet up to 1 T (0.1% field homogeneity over the sample length) made by Cryomagnetics surrounds the Cu tube carrying the sample.

3.3 Measurement Methods

The thermal conductivity as a function of the average temperature of the sample is calculated using Fourier's law where the power supplied to the heater, P, the temperature difference, ΔT, the distance d between the two Cernox, and the cross-sectional area of the sample A are measured:

$$k = \frac{P}{\Delta T}\frac{d}{A} \tag{3.1}$$

The heater power and the sample temperature are controlled with a LakeShore 332 Temperature Controller.

The magnetization of the sample as a function of the applied field is obtained by linearly ramping the current in the superconducting magnet (the field-to-current ratio is 12.9 mT/A) at a rate of about 0.1 A/s while measuring the voltage from the pick-up coil with a Keithley 2182 nanovoltmeter. The magnetization is calculated from the following formula [59].

$$M\left(B_a\right) = \frac{-1}{1-N_D}\int_0^{B_a} \frac{V\left(B_a^{'}\right)-V_n}{V_S-V_n} dB_a^{'} \tag{3.2}$$

where V_n and V_s are the voltages in the normal and superconducting state respectively and N_D is the demagnetization factor, estimated to be about 0.007 for our samples. A Power Ten power supply (0-10 V, 0-100 A) controlled by an American Magnetics 412 Programmer, remotely controlled by a PC, provides the current to the superconducting solenoid. For calibration purposes, we also measured the critical field B_c as a function of temperature for an Indium rod

(99.99% purity) made by melting the Indium in a stainless steel mold. The data, showed in Fig.3.2 , were fitted with the classical formula

$$B_C(T) = B_C(0)\left(1 - \frac{T^2}{T_C^2}\right) \tag{3.3}$$

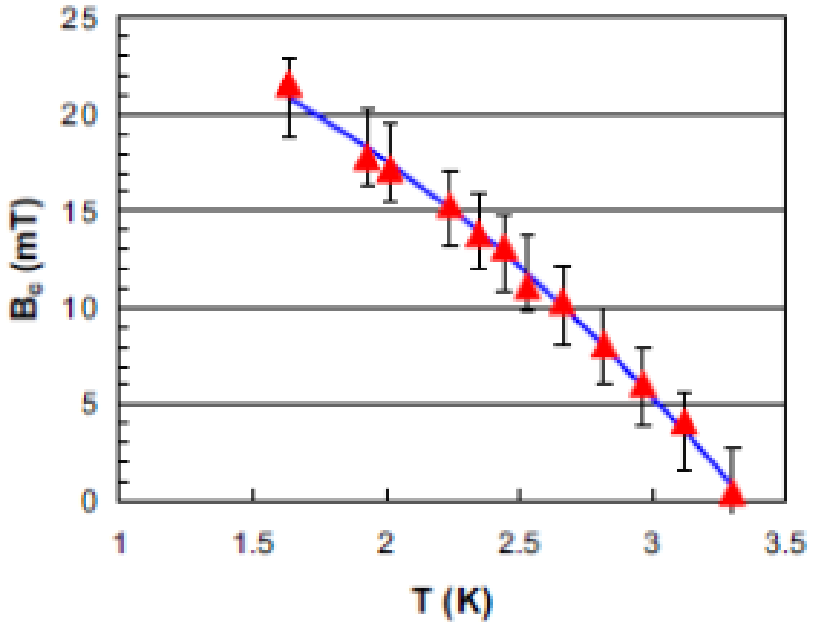

Fig. 3.2: Critical magnetic field as a function of temperature measured on a Indium rod, 99.99% purity. The solid line is a least-square fit with Eqn. (3.3). and resulted in T_c = 3.35±0.03 K and $B_c(0)$ = 270□±2 mT, in good agreement with published data[16].

3.4 Zero field Temperature Dependence of the Thermal Conductivity

The thermal conductivity k is a sum of contributions from electrons and phonons, $k=k_{es}+k_{latt.}$. The electron heat conduction in the superconducting state is reduced because the electrons which have condensed into Cooper pairs do not contribute to any disorder or entropy transport any more. The remaining fraction of electrons which contribute to heat transport decreases exponentially with decreasing temperature. According to BRT theory [52,53],

$$K_{es}/K_{en} = R(y) \qquad R(y) \le 1 \tag{3.4}$$

where, $R(y) = (f(0))^{-1}[f(-y) + y\ln(1+\exp(-y)) + y^2/(2(1+\exp(y)))]$ and $y = \Delta(T)/K_B T = (\Delta(T)/K_B T_c)(T_c/T)$. The approximation $y \cong \alpha T_c/T$ is valid if $T/T_c \le 0.6$.

Finally *f(-y)* is defined as, $f(-y) = \int_0^\infty \frac{z\,dz}{1+\exp(z+y)}$ with $f(0) = \pi^2/12$.

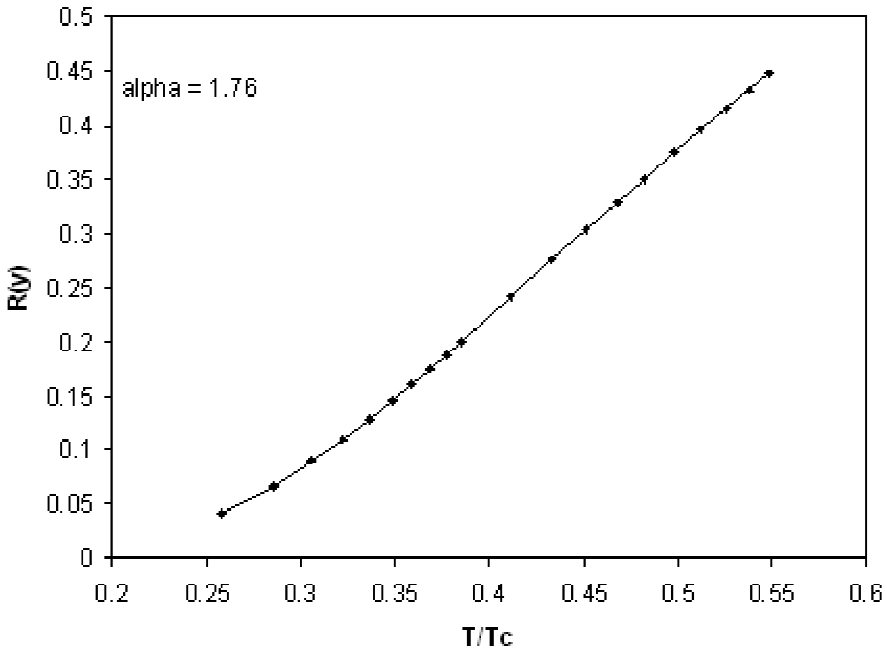

Fig.3.3 The ratio of $K_{es}/K_{en} = R(y)$ as a function of reduced temperat**ure,** $T/T_c = \alpha/y$ (within the experimental temperature range)

Here, T_c, is the superconductor critical temperature, Δ (T), the superconductor energy gap and $\alpha \approx 1.76$ in the BCS theory, but may take values in the range $1.75 \le \alpha \le 1.95$ because of strong coupling effects. The ratio $K_{es}/K_{en} = R(y)$ is plotted as a function of T/T_c taking $\alpha \approx 1.76$ in Fig.3.3 within the experimental temperature range 1.8-5K used for our experiments.

The lattice thermal conductivity is limited by the different scattering mechanism of phonons with point defects, dislocations (line defects), grain boundaries, sample walls, and electrons. The general expression for lattice conductivity is $k_{latt.} = \frac{1}{3} C_v \cdot v^2 \cdot \tau$ where 1/τ is the total scattering rate of phonons from different scattering mechanisms, C_v is the specific heat per unit volume and v is the average velocity of the carriers of thermal energy. The resultant lattice thermal conductivity taking into account the phonon scattering by the electrons and by the crystal boundaries is given by,

$$K_{latt.,s} \cong \left[\frac{1}{\exp(y) D T^2} + \frac{1}{B l_{ph} T^3} \right]^{-1} \tag{3.5}$$

Where, D and B are two constants and l_{ph} is the phonon mean free path and for our large grain niobium sample it is the smallest sample dimension as the grain size of the sample was bigger than the diameter of the sample rod. The total heat conductivity of the superconducting metal is obtained by adding the electron term $K_{es}(T)$ and the lattice term $K_{latt.,s}(T)$. This of course is valid for temperatures T lower than the critical temperature, because $y = \Delta(T) / K_B T$ is defined only in this domain,

$$K_s(T) \cong R(y) \left[\frac{\rho_{295K}}{L \cdot RRR \cdot T} + A \cdot T^2 \right]^{-1} + \left[\frac{1}{\exp(y) D T^2} + \frac{1}{B l T^3} \right]^{-1} \tag{3.6}$$

Where L is the Lorentz constant, A is the coefficient of momentum exchange with the lattice vibrations, D is the coefficient of momentum exchange with the normal electrons and B is a constant which depends on the material and mechanism of scattering. In order to obtain $K_s(T)$ using this model, it is necessary to give experimental values to three variables: temperature T,

residual resistivity ratio RRR and the phonon mean free path l_{ph}. On the other hand the theoretical parameters A, L, α, B, D are obtained by fitting these five parameters to the experimental results. The RRR value is generally determined by the well known relationship established by Padamsee [21], $RRR = 4\ k_{s,4.2K}$. But to determine the RRR value in our studies we have measured the thermal conductivity at 4.2K in normal (k_{en}) and superconducting state (k_{es}) and then used the following procedure to have the correct value of the measured RRR. The standard formula of RRR is replaced by RRR = δ $k_{s,4.2K}$, where δ is defined by $\delta = \rho_{295K}/R(y)LT$. To calculate the RRR value we take ρ_{295K} = 1.44x10^{-7} Ω-m, $L = 2.45\ x10^{-8} WK^{-2}$, T =4.2K and R(y) is experimentally determined using Eqn.3.4. It is found that the value of the parameter δ is 4.7 in case of BCP cleaned samples whereas for the heat treated samples it varied from 4.2-4.5.

Experimental thermal conductivity measurement data for four different samples named as A0, B0, C0 and D0 and A1, B1, C1 and D1 are shown in Fig. 3.4 and Fig. 3.5. The corresponding RRR values are shown in the insets of Fig.3.4 and Fig.3.5. The RRR values for the samples are calculated using the empirical formula $RRR = 4x\ K_{4.2}$, where $K_{4.2}$ is the thermal conductivity at 4.2K. The samples A0,B0,C0 and D0 are degreased ultrasonically after the EDM wire cut and then about 180μm are etched away from all the samples surface by buffered chemical polishing (BCP- 1:1:1, HF+HNO_3+H_3PO_4). After the first set of measurement all the samples are degassed in a vacuum furnace at 600^{0}C for 10 hour in a vacuum better than 10^{-6} Torr. Then a light BCP (1(HF):1(HNO_3):2(H_3PO_4)) is carried out on all the heat treated samples to remove about 20μm. This set of samples is named as A1, B1, C1 and D1 respectively.

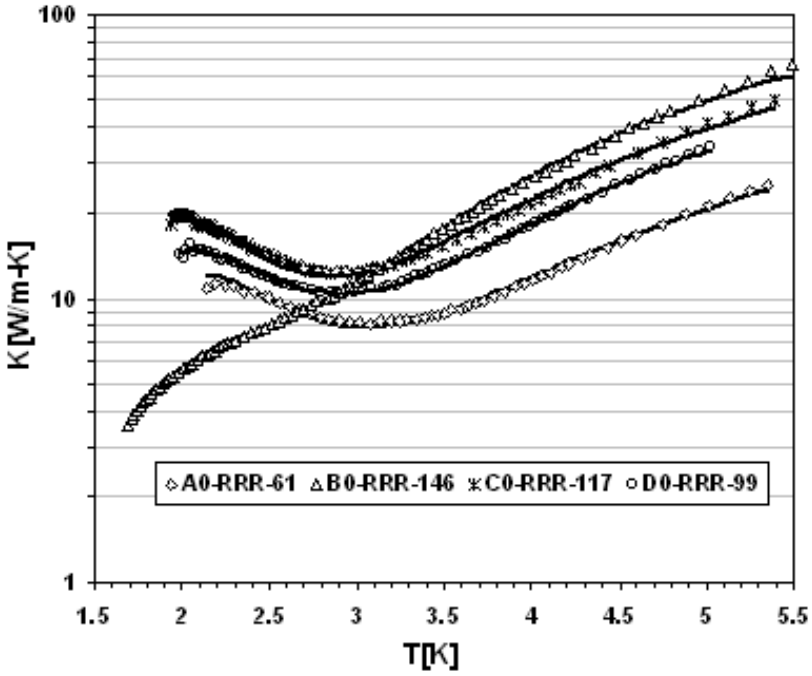

Fig.3.4 Experimental thermal conductivity data for 180 µm buffered chemical polished Niobium samples from four different ingots. Solid lines are the fitting curves.

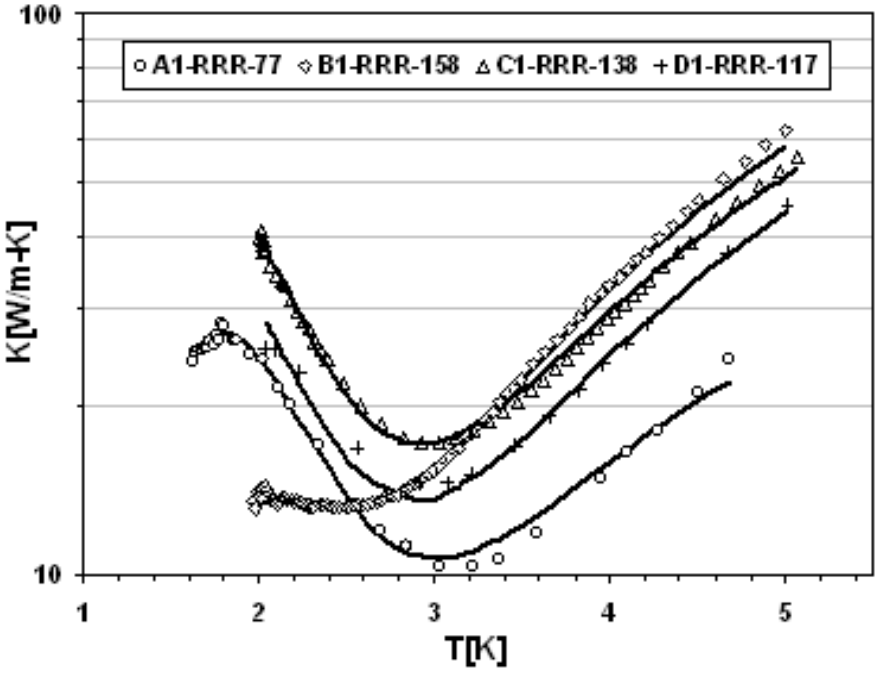

Fig.3.5 Experimental thermal conductivity data for 600^{0}C heat treated Niobium samples from four different ingots. Solid lines are the fitting curves.

Table 3.1 Theoretical fitting parameters of the thermal conductivity data.

Parameters → / Samples ↓	A	A	1/D	B
A0	1.87	5.03E-05	482	1.02E+03
B0	1.78	3.05E-05	523	3.78E+02
C0	1.81	4.07E-05	348	2.02E+03
D0	1.86	2.97E-05	423	1.24E+03
A1	1.86	1.00E-05	402	3.01E+03
B1	1.77	7.00E-07	299	1.06E+03
C1	1.80	1.00E-06	237	6.32E+03
D1	1.86	1.64E-05	289	2.33E+03

The experimental curves were fitted with the above model taking $L = 2.45 \times 10^{-8} WK^{-2}$ and the theoretical parameters $\boldsymbol{A, \alpha, B, D}$ obtained from the fitting curves are listed in Table 3.1.

The resultant error in k calculation is $\left\langle \left(\Delta k / k \right)^2 \right\rangle^{1/2} \cong \mathbf{6\%}$. The experimental fit parameters are in good agreement with theoretical parameters reported in Ref. [52]. Table 3.1 shows that the BCS gap parameter α doesn't change in all four samples before and after the 600^0C degassing. The 600^0C, 10 hour degassing is given to remove interstitial hydrogen and mechanical stress relaxation. Thus 600^0C degassing has no effect on the BCS electron-phonon coupling constant, $\lambda \sim N(\varepsilon_F).V$, where $N(\varepsilon_F)$ is density of states for normal electrons at Fermi energy and V is matrix element of scattering interaction. It suggests that some other scattering mechanism such as

electron-defect is responsible for the change in thermal conductivity after 600^0C heat treatment. The parameter $\boldsymbol{B \propto 1/a_0}$ increases after the degassing, where a_0 is the lattice constant. The increase in B implies that the lattice constant a_0 decreases and hence the interstitial hydrogen concentration reduces which plays a role in the lattice parameter expansion when it is trapped at the tetrahedral positions of the BCC niobium lattice.

The temperature dependence of thermal conductivity of sample C1 in superconducting state K_s and in normal conducting state K_n is plotted in Fig.3.6. The solid line which fits the normal state data points is obtained from the first term on the right hand side of Eqn.3.6 excluding the *R(y)* term. The parameter *A* is the best fit value as shown in Table 3.1 for the sample C1 and $L = 2.45 \times 10^{-8} WK^{-2}$, $\rho_{295} = 1.45 \times 10^{-7}$ and $RRR = 138$ are used as material constants for the fit in

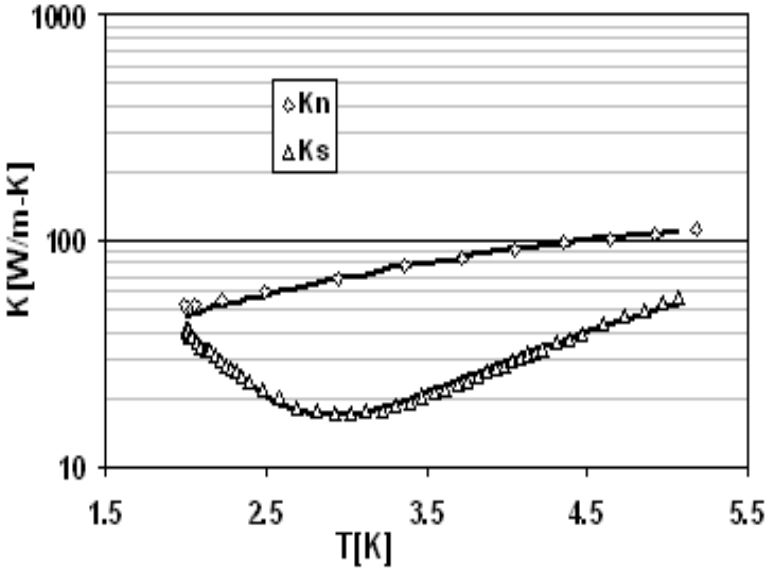

Fig. 3.6: Thermal conductivity data in normal and superconducting state for the sample C1. Solid lines are the fitting curves with Eqn.3.6.

superconducting state. So the fit parameters are in well agreement for both the normal state and superconducting state data. As a result this model can be applied to calculate the electronic and phonon conductivity in normal and superconducting sate.

3.5 Field Dependence of Thermal Conductivity

The core of the trapped flux line is represented by a region of radius ξ, the GL coherence length, within which the modulus of the order parameter, $\Delta(r)$, is significantly reduced. Within this core the magnetic field and the superfluid velocity are large enough to cause depairing, so that we expect to find bound excitations that are localized within the core. From the studies of *Caroli et al* [54], for clean materials with large GL parameter k, it was confirmed that except for an energy gap ~ Δ_∞/E_F, where Δ_∞ is the BCS energy gap in the Meissner state and E_F is the Fermi energy, the density of states is similar to that in a normal metal cylinder of radius ξ. The effect of magnetic field in the materials of smaller k_{GL} (λ_L/ξ) has been studied by *Hansen* [55] and by *Bergk and Tewordt* [56]. They found that the small gap may disappear, but the density of states remains of the same order of magnitude.

The properties of these excitations (for small and large k_{GL}) are quite different from those of normal electrons: coherence factors are generally different, and group velocities along the flux lines are expected to be much smaller than those of the normal electrons. The low group velocity means that the contribution of the bound excitations to the thermal conductivity (measured parallel to the flux lines) should be very small. In addition to these bound excitations there will be unbound excitations. The unbound excitations behave as BCS quasiparticles at distances larger than the penetration depth from the vortex core. Near the flux lines they will be modified as they interact with the magnetic field, the superfluid velocity, and the modulation of $\Delta(r)$. This

interaction will cause scattering among quasiparticles which in turn will reduce the electronic thermal conductivity in the mixed state due to the trapped flux lines in the material at favorable locations. In the Meissner state, phonons interact with the electronic excitations, and this interaction plays an important role in thermal conduction in the Meissner state of a superconductor at fairly low temperatures. When the magnetic flux is trapped within the material, phonons will again interact with the bound excitations in the core. The strength of this interaction can be calculated from the Ref. of *Caroli et al* [54], taking into account much higher frequencies for the thermally excited phonons.

Before presenting the experimental results a theoretical review of the field dependence of the phonon and electron conductivity is discussed below.

i) At low inductions (H<<Hc2) and at low temperature (T<<Tc) the phonons are scattered by a random array of vortices and these behave as if they were cylinders of normal metal [57,58].The qualitative expression of the phonon conductivity as a function of B is given by,

$$\frac{K_{ph}(0)}{K_{ph}(B)} = 1 + \sigma \frac{B}{H_{C2}} \frac{K_{ph}(0)}{K_{ph}^{n}} \tag{3.7}$$

where σ is the average scattering diameter of a vortex line for the thermal phonons (σ ~ 0.5). Similarly the electronic thermal conductivity as a function of B is given by,

$$\frac{K_{e}(0)}{K_{e}(B)} = 1 + \frac{l_{e} a B}{\Phi_{0}} \tag{3.8}$$

where l_e is the mean free path of electrons in zero field, Φ_0 is flux quanta and a is the effective scattering diameter of a vortex line for the free excitations.

ii) At large inductions i.e. close to H_{C2} and at low temperature, the field dependent thermal conductivity has been analyzed by *Houghton-Maki* [58]. They have determined the thermal conductivity when (a) the temperature gradient is parallel to the applied magnetic field and (b) the temperature gradient is perpendicular to the applied magnetic field. The result of Houghton-Maki for the temperature gradient parallel to the applied magnetic field is given by,

iii)

$$\frac{\Delta K\|}{K_e^n} = -6\mu\left[\left(1-\mu^2\right)J_1 - \left(\frac{1}{4}\pi - \mu\right)\right] \tag{3.9}$$

where, $J_1 = \int_0^{\pi/2} \frac{\cos\theta}{\cos\theta+\mu} d\theta = \frac{\pi}{2} + \frac{2\mu}{\sqrt{1-\mu^2}} Tanh^{-1}\left[\frac{\mu-1}{\sqrt{1-\mu^2}}\right]$ and μ is the transport coefficient given by, $\mu = 2\sqrt{\pi}\frac{\Delta^2}{\hbar^2 k_c v_F^2} l_e$ in which k_c is the reciprocal lattice vector of the vortex lattice and v_F is the Fermi velocity, Δ is the order parameter and l_e is the electron mean free path and $\Delta K\|$ is the difference between the normal and superconducting state electronic thermal conductivities.

The experimental thermal conductivity measurement of the sample-A1 and C1 with and without the trapped vortices is shown in Fig.3.7. The bulk magnetization measurement allows us to get the values of remnant magnetization for those samples. The bulk magnetization measurement for A1 and C1 is shown in Fig.3.8. The magnetization curves show that the trapped magnetic flux in A1 and C1 is 58 and 80 mT, respectively. Fig.3.7 shows that the effect on the electronic part of

the thermal conductivity by the scattering of electrons with the vortex cores is negligibly small. Whereas the phonons are strongly scattered causing an

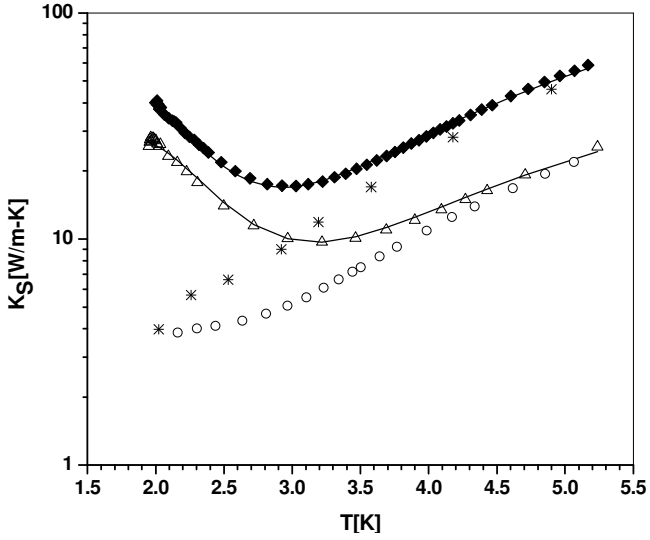

Fig.3.7 Plot of k_S versus T, ■ C1-Zero field, *C1-Trapped flux 81 mT, Δ A1-Zero field, ○ A1-Trapped flux 60 mT, solid lines are the fitting curves of Eq. (6).

almost zero contribution to the net thermal conductivity. The field dependence of phonon and electronic conductivity of Eqn.3.7 and 3.8 are used to interpret the thermal conductivity results with trapped vortices for the sample A1 and C1. K^n_{ph} is being calculated from the Eqn. 3.5 in case of normal metals using the value of the parameters D and B from the Table 3.1.

The phonon conductivity in the normal sate for A1 and C1 are *0.01* and *0.017 W/m-K* respectively. The value of electron mfp l_e is calculated using the expression $\mathbf{1/\rho = 2e^2 S_F l_e / 3(2\pi\hbar)^3}$, where S_F is the area of the Fermi surface in momentum space in the first Brillouin zone and ρ is the electrical resistivity. A value of

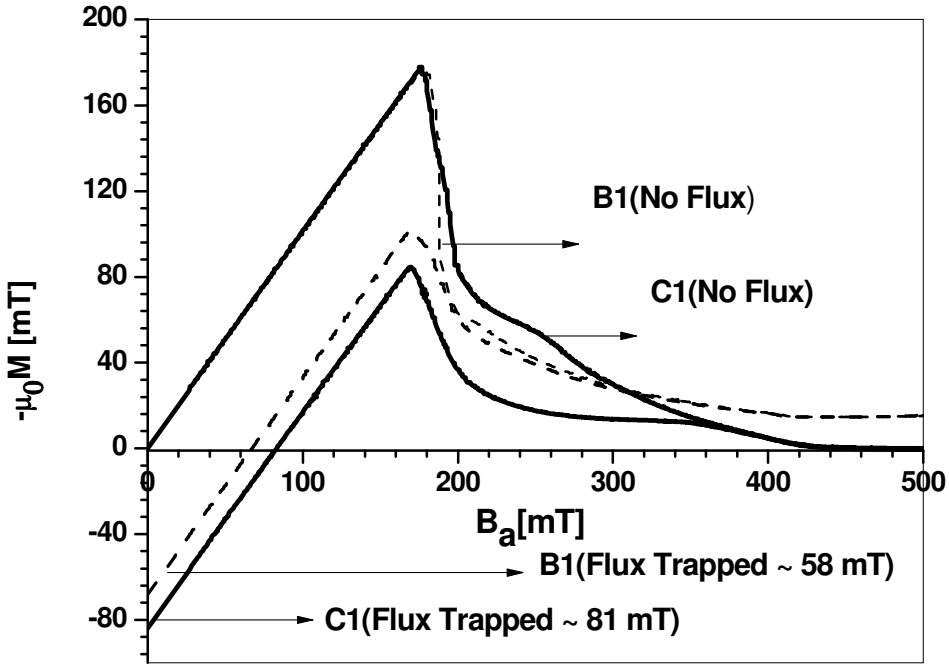

Fig. 3.8 Magnetization curves at T = 2K with and without remnant magnetization for ---- A1, —— C1.

$S_F = 2.23 \times 10^{-47}$ kg^2m^2/sec^2, the value for ρ are 2.37×10^{-9} and 1.12×10^{-9} Ω-m are used for A1 and C1 to calculate the electron mfp. The thermal conductivity model defined in Sec. III gives a reasonable fit of the experimental data points as shown in Fig.3.9, when corrected using Eqn.3.7 and 3.8 to take into account the presence of trapped vortices .The error in k calculation is $\left\langle (\Delta k/k)^2 \right\rangle^{1/2} \cong 6\%$. Fig.3.9 shows that the deviation of the theoretical curve from the experimental data increases with the increase of trapped flux which signifies that the other mechanisms, such as inter vortex tunneling and collective mode excitations of the flux line lattice play a role at higher fields. As the flux lines act as normal metal cores randomly distributed over the sample cross section, they can be treated as point like scattering centers to the thermally excited phonons and BCS quasi-particles. The thermal conductivity results of sample A1 and C1 with trapped

vortices are fitted with Eqn.3.9 taking into account that the vortex cores are randomly distributed point like scattering centers. The fitting parameters in presence and absence of trapped vortices are summarized in Table 3.2.

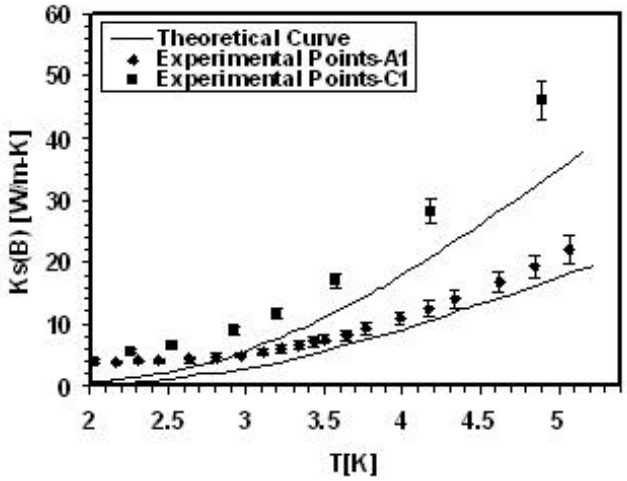

Fig.3.9 Effect of trapped vortices on the superconducting state thermal conductivity in sample A1 and C1. Solid lines represent the qualitative theoretical model by *Vinen et.al.* at low inductions and at low temperature.

Table 3.2 Theoretical fitting parameters in presence and absence of trapped flux lines

Parameters	Sample A1		Sample C1	
	Zero Flux	Trapped Flux (58mT)	Zero Flux	Trapped Flux (81mT)
α	1.86	1.78	1.78	1.70
L	2.45×10^{-8}	2.45×10^{-8}	2.45×10^{-8}	2.45×10^{-8}
A	1.00×10^{-5}	1.77×10^{-4}	1.00×10^{-6}	7.94×10^{-5}
1/D	402	1216	216	758
B	3.01×10^{3}	3.35×10^{2}	6.32×10^{3}	2.63×10^{2}

From Table 3.2 we can see that the gap parameter α and *the* coefficient of momentum exchange of electrons with the lattice vibration, *A*, decreases while the coefficient of momentum exchange of phonons with the electrons, *D*, increases in the presence of trapped vortices. The parameter $\boldsymbol{A \propto N^{2/3}}$ and the parameter $\boldsymbol{D \propto N^{-2}}$, where *N* is the effective number of conduction electrons per atom. As the vortices are trapped inside the superconductor the effective number of conduction electrons reduces because of the bound excitations within the vortex core. The reduction in the gap energy α is due to the low energy excitations close to the vortex core. The energy gap of these excitations is very small and is given by $\varepsilon_0 \sim \Delta_0^2/E_F$. So the effective energy gap will be $\Delta_{eff} \sim (\Delta_0 - \varepsilon_0)$. Taking $E_F = 0.00018 m_0 c^2 = 91.8$ for niobium and Δ_0=*1.86(A1) and 1.78 (C1)* from the experimental fit data of the zero trapped vortex sample, we get ε_0 *~0.04 (A1) and 0.034(C1)* leading to an effective energy gap of Δ_{eff} *~1.82 (A1) and 1.74(C1)*. This simple explanation gives an error of 2.4% for the fit parameter α. The variation of thermal conductivity with the applied magnetic field for the sample B1 with and without trapped vortices at 2K is shown in Fig.3.10.

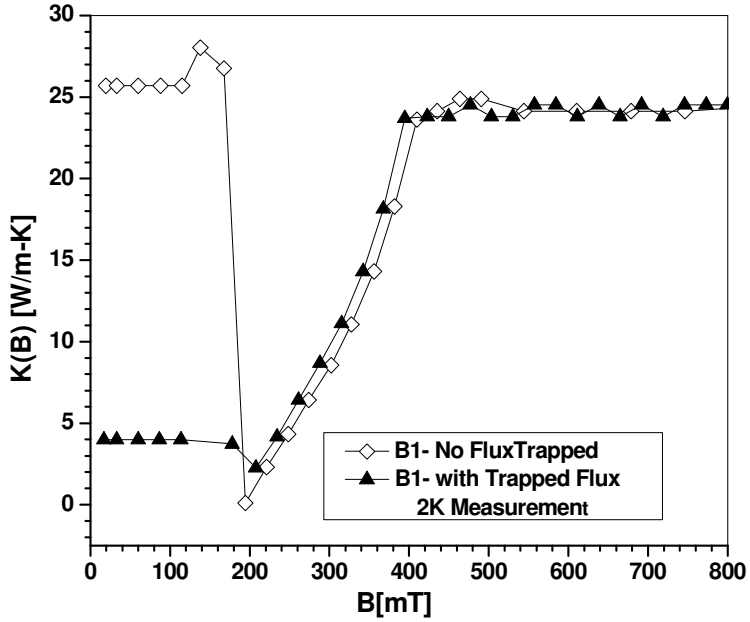

Fig.3.10 Field dependence of the thermal conductivity with and without trapped vortices measured with the field parallel to the heat flow direction at 2K.

We can see that the value of H_{C1} and H_{C2} are independent on the sample condition from the point of view of trapped vortices. Both the curves are showing the same behavior in the mixed state. In the mixed state the phonon contribution is negligibly small; it is the electronic contribution which increases with the increasing magnetic field as more and more quasiparticles start contributing to the thermal conductivity. Eventually as the applied field reaches H_{C2}, the bulk of the superconductor is in the normal state while the surface remains in the superconducting state to an extent of the order of coherence length ξ_0. The figure shows a constant thermal conductivity between H_{C2} and a value of applied magnetic field beyond the third critical field H_{C3}. So we couldn't find any effect of the surface sheath on the measured thermal conductivity, as expected. Above H_{C2} the specimen shows the thermal conductivity behavior of the normal metal. But there is marked difference of the measured thermal conductivity data in the region $\mathbf{0 \leq H \leq H_{c1}}$ for

the sample with and without trapped vortices. No magnetic flux enters the samples up to the first flux penetration at 180 mT. Below H_{c1}, the difference between the thermal conductivity values of the two curves in Fig.3.10 is due to the strong scattering of phonons by the vortex cores as explained earlier.

At large inductions and at low temperature the field dependent thermal conductivity is represented by the Houghton-Maki theory described by the Eqn.3.9. A plot of μ versus $\Delta k/k_e^n$ is shown in Fig.3.11.

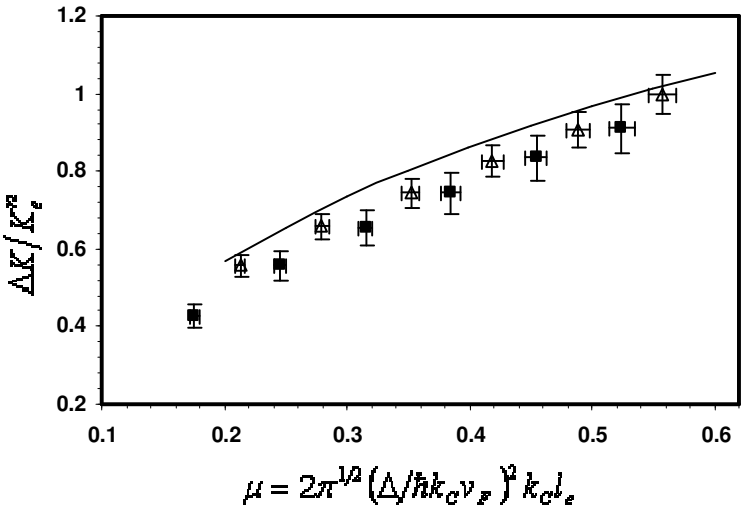

Fig.3.11 $\Delta k/k_e^n$ as a function of μ in sample B1. (Δ) Sample B1 without any trapped flux in zero field, (■) sample B1 with an initial remnant magnetization of about 58 mT, solid line is the theoretical curve of Houghton-Maki.

Fig.3.11 shows that when there are trapped vortices in zero field, the experimental data points for $\mathbf{0.2 \le \mu \le 0.6}$ lie below the theoretical curve as well as the baseline measurement data in zero field without the trapped vortices. This might be due to the additional contributions from the bound excitations in the form of tunneling. Although the exact cause is not yet clear but there is definitely an additional contribution to the thermal conductivity in case of initial remnant

magnetization. A future experiment with different remnant magnetization at zero field and the corresponding thermal conductivity measurement will produce a systematic deviation from the Houghton-Maki theory and the evidence for this new contribution to the thermal conductivity can be established.

Finally, the measurements of the thermal conductivity of sample C1 after zero-field cooling, after the applied magnetic field was cycled from zero up to H_{c2} and then back to zero, and after warming-up the sample above T_c followed by zero-field cooling is shown in Fig.3.12. The remnant magnetization after cycling the applied magnetic field is about 81mT.

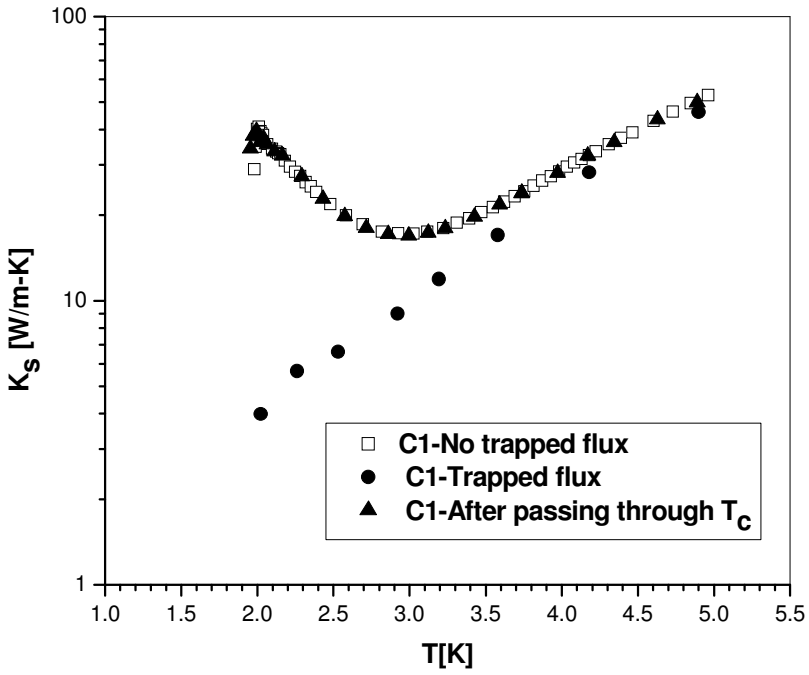

Fig.3.12 Plot of thermal conductivity in superconducting state in zero remnant field, with remnant field and heating up the sample through T_c to exclude the flux lines to reproduce the zero field curve

As shown in Fig.3.12, the phonons are strongly scattered by the vortex cores. By raising the temperature of the sample above T_c(9.25K), the remnant magnetic field is homogeneously

distributed throughout the normal conducting sample. By lowering the temperature below T_c, the magnetic flux is expelled from the superconductor and a new thermal conductivity measurement reproduces the data obtained after the first measurement, in absence of any applied magnetic field.

3.6 Conclusion

The thermal conductivity as a function of temperature measured on large grain niobium samples in the Meissner state is well described by the model of Ref. [52] within the experimental error of $\pm 6\%$. The measurements clearly show the presence of a phonon peak at around 2K. One important observation is that the phonon peak is eliminated by the presence of trapped vortices due to the strong scattering of phonons with vortex cores. When the vortices are trapped inside the sample, the fit parameters indicate a reduction of the gap energy α due to the low energy excitations having very small energy gap ~ Δ_0^2/E_F close to the vortex core. Also the effective number of conduction electrons decreases due to the bound excitations in the vortex cores. The dependence of the thermal conductivity with the applied magnetic field for the samples with and without trapped vortices show the same H_{C1} and H_{C2} values as from the magnetization measurement.. Finally when the temperature of the samples is cycled above T_c, the thermal conductivity measured for the sample in absence of an applied magnetic field is restored. The temperature dependence of the thermal conductivity at low temperature and low magnetic field agrees qualitatively with the model of *Vinen et al*. In the vicinity of H_{C2} the thermal conductivity agrees quite well with *Houghton-Maki* theory for the virgin sample i.e without any trapped vortices. But if there is initial flux trapped within the sample, the measured thermal conductivity deviates from the Houghton-Maki theory and observed an increase in thermal conductivity in the

range of $\mathbf{0.2 \leq \mu \leq 0.6}$. Future experiments with different initial trapped vortices and subsequent measurement of the thermal conductivity in the range of $\mathbf{0.2 \leq \mu \leq 0.6}$ might help to interpret the deviation from the theory.

Chapter 4

Effect of Low Temperature Baking on Bulk Magnetization, Surface Magnetization and Penetration Depth

It has been known for quite some time that the low temperature baking (LTB) (100 – 140 ^{0}C) is a necessary final preparation stage to achieve high accelerating gradients in niobium RF cavity [62, 63]. To date there exist different models to understand the LTB effect on niobium RF cavity, although any of them is not complete in a sense which can explain all the experimental observations. At present there is an oxygen diffusion model [64] which takes into account the oxygen diffusion with LTB resulting in dilution of oxygen pollution over the penetration depth. Over the time as research progressed it has been found that there are other possibilities which can explain Q-drop and baking effect namely the mechanisms based on hot-spot [65], dislocations [66], interface tunnel exchange [67] and magnetic impurities [68]. A present study of B. Visentin [69] on niobium samples with positron annihilation spectroscopy has shown that there is an increase of vacancy site with the LTB in a length scale of about 120 nm from the surface and as explained this might be due to the dissociation of hydrogen-vacency complexes by baking followed by hydrogen diffusion.

In this chapter a systematic magnetization measurement and penetration depth study of poly crystalline and large grain niobium are presented. This study was carried out with the aim to understand the superconducting behaviour of the surface sheath and correlation of the surface sheath behaviour with different surface treatment like BCP, hydrogen degassing at 600^{0}C, post purification at 1200^{0}C, low temperature baking (LTB) in the range 100^{0}C – 140^{0}C. The same

experimental setup as described in chapter 3 was used to study the magnetization and penetration depth measurement.

4.1 Description of Samples

4.1.1 Large Grain Samples

Four samples were made from four different niobium ingots received from CBMM, Brazil. The Ingots named A, B, C and D has different RRR and different impurity contents. Samples are cut by wire EDM and then machined by lathe to a diameter of 6 mm and 120mm length. After machining, all the samples were degreased in ultrasonic bath with micro solution for 30 min. Table 4.1 shows the different surface treatments on the samples before each measurement.

Table 4.1 Surface treatments on samples A, B, C and D before each measurement. The number following the letter in the sample codes identifies the measurement number.

Measurement	Sample Code	Process
1st Set	A1,B1,C1,D1	BCP(1:1:1) to remove about 180 µm.
2nd Set	A2,B2,C2,D2	Degassed at 600^0C for 10 h at a vacuum $<10^{-6}$ Torr. Then degreased and BCP (1:1:2) to remove about 24 µm.
3rd Set	A3,B3,C3,D3	Degreased and baked at 100^0C for 12 hour at a vacuum $< 10^{-6}$ Torr.
4th Set	A4,B4,C4,D4	BCP (1:1:2) 10 µm and baked at 120^0C for 12 hour at a vacuum $< 10^{-6}$Torr.
5th Set	A5,B5.C5,D5	BCP (1:1:2) 10 µm and baked at 140^0C for 12 hour at a vacuum $< 10^{-6}$Torr.

4.1.2 Polycrystalline Samples

A fine grain sample (RRR ≥ 250) is cut by wire EDM and then machined by lathe to a diameter of 6 mm and 120mm length. After machining, the sample was degreased in ultrasonic bath with micro solution for 30 min. Table 4.2 shows the different surface treatments on the samples before each measurement.

Table 4.2 Surface treatments on the polycrystalline sample and named as a, b, c and d.

Measurement	Sample Code	Process
1st Set	a	The sample has been degreased, BCP ($HF:HNO_3:H_3PO_4$::1:1:1) for a total of 12 min. removing about 85 micron from the cylindrical surface, annealed at 600^0C for 10 hr at vacuum of 10^{-7} mbar, further BCP for 5 min. removing about 35 micron.
2nd Set	b	Sample 'a' was in atmospheric contact for about 9 days and then BCP was done for 5 min etching about 35 micron from the surface.
3rd Set	c	Sample 'b' is heat treated at 1250^0C in a vacuum furnace using titanium as getter. The heat treatment is done in following sequences, i) Temp is raised to 1250^0C in about 4 hr. and is held for 12 hr. ii) Temp is then lowered to 1000^0C at a rate ~ 0.2^0C/min. iii) After reaching 1000^0C the cooling to room temperature began & it took around 16 hr. iv) Max. Pressure at 1250^0C $\leq 10^{-4}$ mbar. Decrease to about $\leq 10^{-7}$ mbar before cool down. After the heat treatment BCP was done for 7 min removing a surface layer of about 50 micron.
4th Set	d	Sample 'c' was further cleaned by BCP for 10 mins. In two steps of 5 min each.

4.2 Bulk Magnetization Measurement

4.2.1 Result of Large Grain Niobium Samples

The bulk magnetization curves for the 1st and 2nd set of measurements are shown in Fig.4.1 and Fig.4.2. The results show that H_{C1} and H_{C2} are not affected by the 600^0C heat treatment. The results are presented in Table 4.3.

Table 4.3 DC magnetization measurement results for 1st and 2nd set of samples of large grain niobium.

Sample	$B_{C1,2K}$(mT)	$B_{C2,2K}$(mT)	$B_{C,2K}$(mT)
A	172	400	184
B	181	388	186
C	175	410	184
D	176	405	189

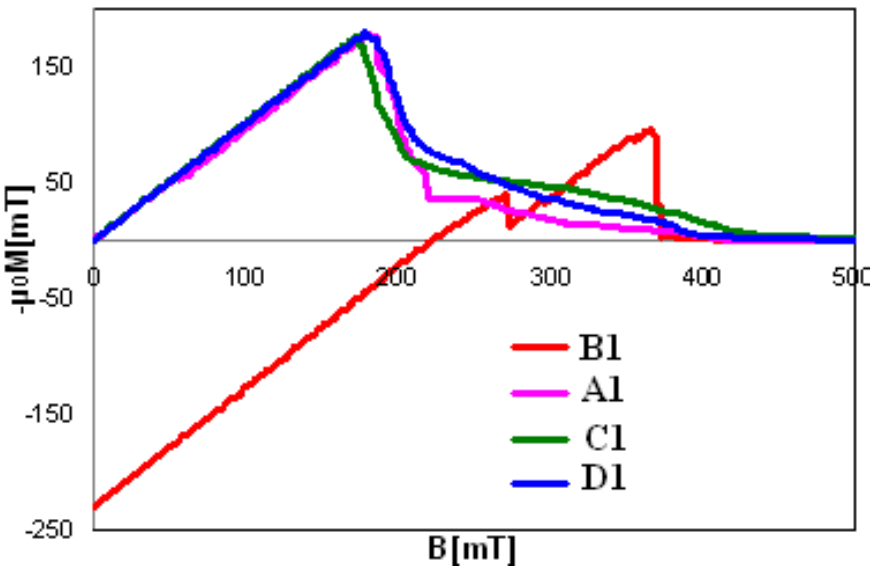

Fig.4.1 Magnetization curves of BCP samples at 2K.

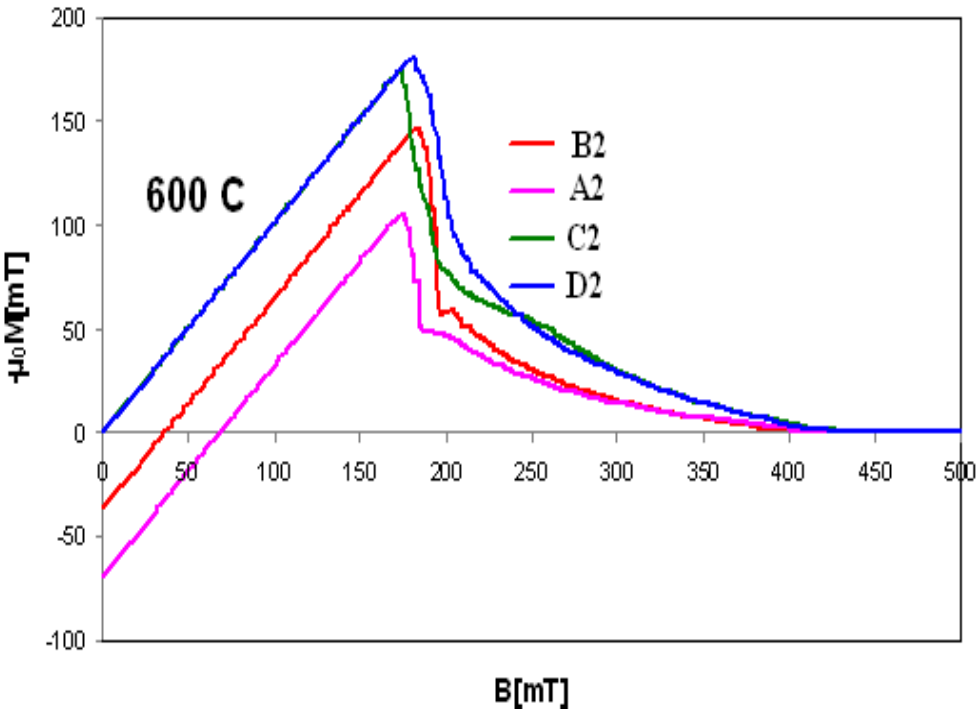

Fig.4.2 Magnetization curve of 600^0C heat treated samples at 2K.

The behaviour of the magnetization curve of sample B1 in Fig.4.1shows strong paramagnetic characteristics but after 600^0C heat treatment the paramagnetic behavior is reduced but still present. Sample A2 in Fig4.2 also show remnant magnetization at zero field. But for sample A2 before the measurement at 2K, one set of measurement has carried out at 4.2 K which didn't show any remnant magnetization. As discussed in the thermal conductivity measurement in chapter 3 the remnant magnetization prevails from the 4.2K measurement in case of sample A2. But the strong paramagnetic behavior of sample B1 is not clearly understood.

The magnetization curves in Fig.4.1 of the sample C1, D1 and in Fig.4.2 C2, D2 doesn't reach to zero above H_{C2} is due to the zero time offset of the magnetic field of the superconducting solenoid during ramp-up period. The offset value in all those curves from the zero level is about

5-7 mT. Also the linear fit of magnetic field as function of time is shown in Fig.4.3. It shows a zero point offset of 6 mT.

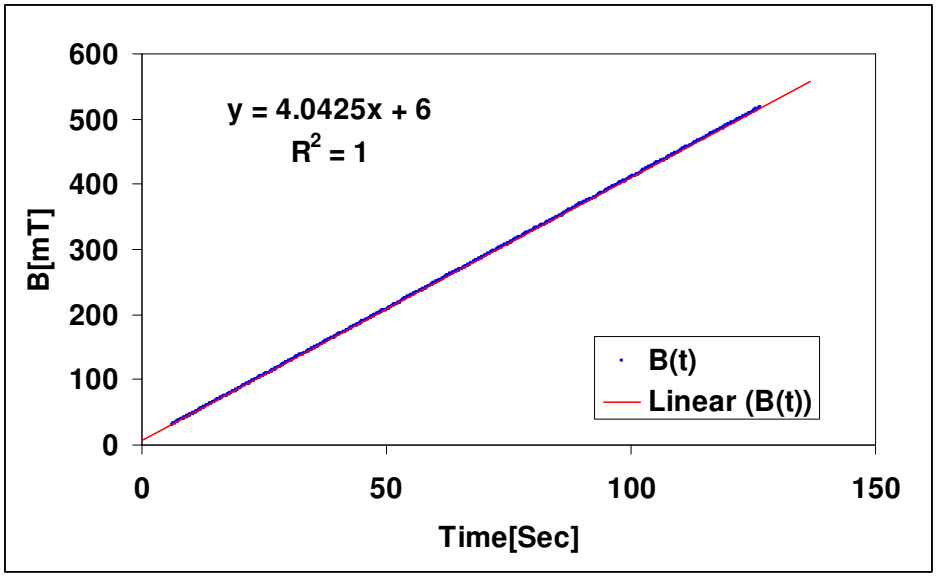

Fig.4.3 Ramp-up of magnetic field with Tin

4.2.2 Result of Fine Grain Niobium Samples

The magnetization measurement at 2K of fine gain samples are shown in Fig.4.4. The sample 'b' which has been hydrogen degassed at 600^0C for 12 hour shows H_{C1}=120 mT and H_{C2}=380 mT. Whereas the sample 'c' is post purified at 1250^0C shows H_{C1}=160 mT and H_{C2}=360 mT. The series of minima in the magnetization curve for both cases corresponds to vortices penetrating into the sample. The increase in lower critical field and the decrease in upper critical field after the 1250^0C post purification clearly indicate a decrease in the GL parameter κ. These results can be interpreted by the dependence of GL parameter κ with H_{c1}/H_c ratio at T/T_c=0.22 correspond to 2K temperature [70]. As the thermodynamic critical field is independent of κ so an increase of H_{C1} corresponds to decrease in GL parameter κ.

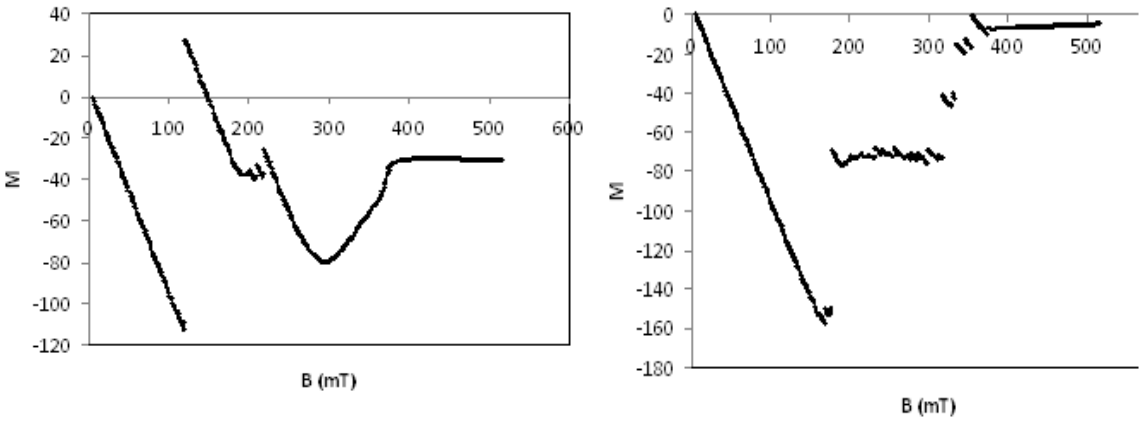

Fine grain sample 'b' **Fine grain sample 'c'**

Fig.4.4 Bulk magnetization measurement of fine grain sample 'b' and 'c' respectively

4.3 Surface Magnetization Measurement

4.3.1 Result of Large Grain Niobium Samples

4.3.1.1 Surface Pinning

By connecting the pick-up coil around the sample rod as part of a L-C oscillator, it is possible to measure the changes of the penetration depth as a function of the applied DC magnetic field by measuring the changes of the oscillator's resonant frequency f_0 (the base frequency is 270 kHz, sampling up to a depth ~10 μm) while slowly ramping up and down the magnetic field above H_{C3}. This method provides information about surface pinning and allows measuring the surface critical field B_{C3}.The irreversibility of the curve between B_{C1} and B_{C2} is an indication of surface pinning. The typical behavior of surface pinning measurements is shown in Fig.4.5. The value of the surface H_{C1} and H_{C2} remains constant with different surface treatments like BCP 180 μm, 600 C 10 hr. heat treatment and 100 C, 120 C, bake for 12 hr. in vacuum. But H_{C2} starts to

increase after 140 C baking. The data show that after low temperature baking the irreversibility reduces by a

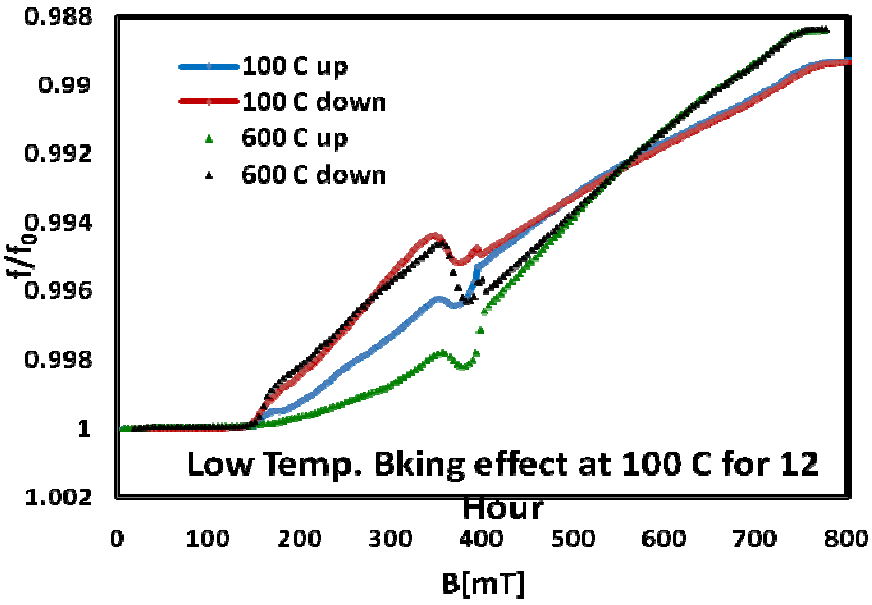

Fig.4.5 Surface pinning characteristics before and after the LTB.

significant fraction. This can be interpreted as a reduction of impurities near the metal surface. Similar pinning measurements at higher frequency would allow reducing the sampling depth and therefore would have higher sensitivity to impurities within the penetration depth in the superconducting state.

4.3.1.2 Effect of LTB on H_{c3}/H_{c2} ratio

In real superconductor (SC) the surface is contaminated by impurities, dislocations, grain boundaries etc. which decreases the mean free path (mfp). In Shmidt's model [71] the surface of the bulk SC is represented by a film of thickness *'d'* with GL parameter k_1 and the bulk SC is represented by k_2. The basic assumption in this model is that the surface layer and the bulk SC

have the same T_C and H_C. This model predicts that the ratio of H_{C3}/H_{C2} is enhanced when $d \leq \xi_0$ and is given by the following relation,

$$\frac{H_{C3}}{H_{C2}} = 1.67\left[1+\left(\frac{k_1-k_2}{k_1}\right)\sqrt{1.7}\,\frac{d}{\xi(T)}\right] \tag{4.1}$$

In order to apply this model in the region $T<<T_C$ it is required to take into account the nonlinearity of the microscopic theory. In this regard Hu and Korenman (HK) [72] derived the H_{C3}/H_{C2} ratio in the range $0 \leq T \leq T_C$ using Gorkov's gap equation. The ratio is given by,

$$\frac{H_{C3}}{H_{C2}} = 1.69C(t) \tag{4.2}$$

where,

$$C(t) = 1+0.614(1-t)-0.577(1-t)^{3/2}-0.007(1-t)^{2}+0.106(1-t)^{5/2} \quad \text{and} \quad t = \frac{T}{T_C}\ .$$

We apply Shmidt's model by multiplying Eqn. (4.2) by HK polynomial *C(t)* in order to extend its validity to $T<<T_C$. The final form of the equation which has been used to explain the experimental results is given by,

$$R = \frac{H_{C3}}{H_{C2}} = 1.67C(t)\left[1+\left(\frac{k_1-k_2}{k_1}\right)\sqrt{1.7}\,\frac{d}{\xi(T)}\right] \tag{4.3}$$

The temperature dependence of H_{C3}/H_{C2} has two independent sources. One which takes into account the nonlinearity of the microscopic theory and the other consider the effect of the surface film of thickness *'d'*. k_2 is calculated using the relation $H_{C2} = \sqrt{2}k_2 H_c$, where H_{C2} is the experimentally measured value and H_C is calculated by the following Eqn.

$$H_C^2 = 2\mu_0 \int_0^{H_{C2}} M(H)dH \tag{4.4}$$

and ξ[T] is calculated by using the relation $\boldsymbol{H_{C2} = \frac{\phi_0}{2\pi\mu_0\xi^2}}$.

Experimentally we measure the frequency as a function of applied magnetic field as discussed in the surface pinning measurement section. Since the contaminated surface layer thickness $\boldsymbol{d \leq \xi_0}$, so the vortices azimuthally collapse with each other when the surface critical field reaches $H_{C2,surf}$ value.

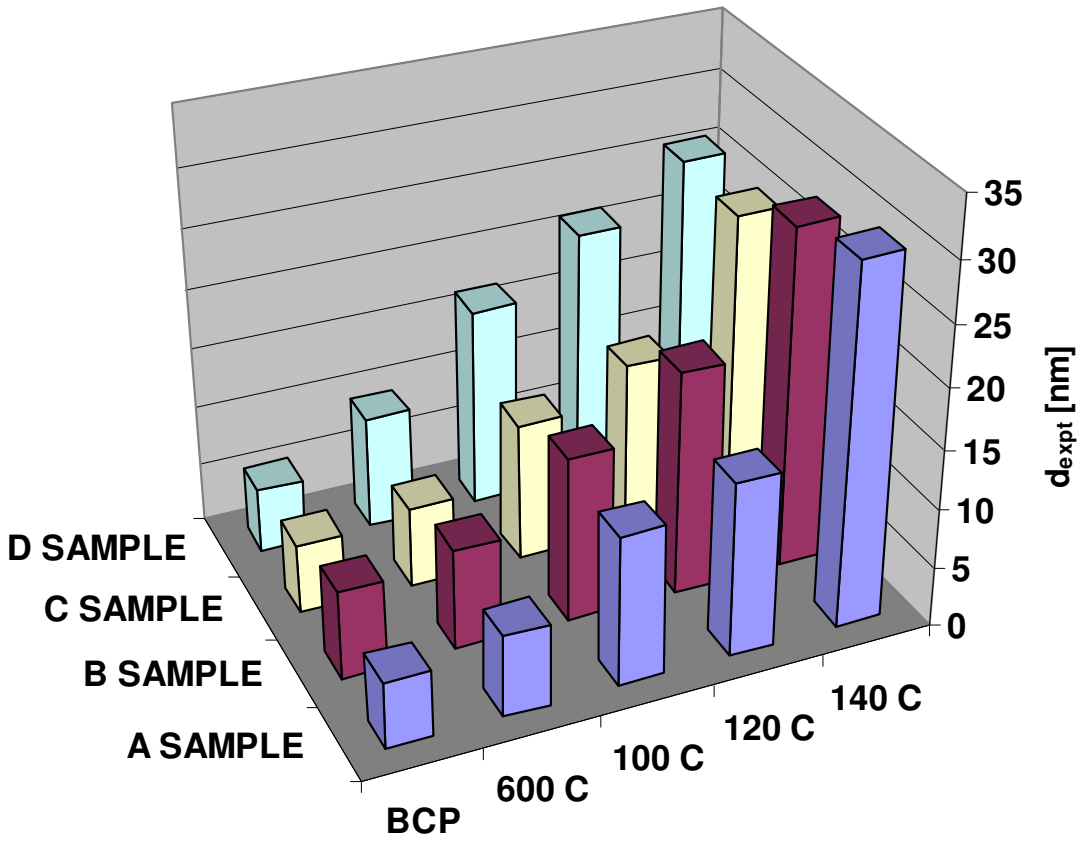

Fig.4.6 d_{expt} with different surface treatment.

As a result the change in penetration depth is very small and hence the transition at $H_{C2,\,surf}$ is not sharp enough to detect from the measured curve as shown in Fig.4.5. For the calculation of k_1 i.e for the surface layer $H_{C2,\,surf}$ was determined by $H_{C2,\,surf} = H_{C3}/1.67*C(t)$[45]. Since the basic assumption on the above model is that both the surface layer and the bulk superconductor has the same thermodynamic critical field H_C an T_C, so k_1 is evaluated using $H_{C2,surf}$ value.

The experimental results are tabulated in the Table 4.4. The result shows that with the increased baking temperature the contaminated layer thickness increases to an average of 5.8 nm, 9.5 nm and 19.6 nm at 100 C, 120 C, and 140 C baking temperature respectively. But at 140 C both the contaminated layer thickness and bulk H_{C2} increases which may be due to the partial dissociation of the Nb_2O_5 layer as explained in the oxygen diffusion model [73]. The histogram plot of pollution depth of all four ingots with the different surface treatments is shown in Fig.4.6.

Table 4.4 results of low temperature baking studies measured at 2K.

Sample	$B_{C1,surf}$ [mT]	$B_{C2,surf}$ [mT] Calculated	$B_{C3,surf}$ [mT]	R	d_{expt} [nm]
BCP(1:1:1) 180 µm					
A1	100	403	761	2.0	5.61
B1	120	372	703	1.93	7.35
C1	115	394	745	2.0	5.87
D1	104	378	714	1.98	5.46
600C 10 hour degassing at a vacuum < 10^{-6} torr, then BCP(1:1:2) to remove 24 µm					
A2	115	398	752	2.02	6.84
B2	122	379	716	2.01	8.45
C2	118	384	725	1.98	6.66
D2	113	379	717	2.01	9.44
Low temperature baking at 100 C in a vacuum <$5x10^{-7}$ Torr for 12 Hour					
A3	117	413	780	2.14	12.5
B3	113	395	746	2.15	13.8
C3	117	429	810	2.15	11.6
D3	111	408	772	2.2	16.7
Low temperature baking at 120 C in a vacuum <$5x10^{-7}$ Torr for 12 Hour					
A4	129	410	774	2.1	14.5
B4	130	383	724	2.12	18.7
C4	130	407	770	2.1	14.6
D4	131	403	762	2.17	21.4
Low temperature baking at 140 C in a vacuum <$5x10^{-7}$ Torr for 12 Hour					
A5	100	615	1162	2.76	30.1
B5	100	518	979	2.60	28.5
C5	100	595	1124	2.60	25.3
D5	104	556	1050	2.55	25.8

The oxygen diffusion model corresponds to a diffusion depth of 7.6nm, 19nm and 40 nm for a baking at 100 C, 120 C and 140 C for 12 hour duration. Except for the 100 C bake the experimentally derived surface layer thickness is about half of the oxygen diffusion depth calculated by the theoretical model. Also the first flux penetration i.e B_{C1} increases with the 100 C and 120 C baking for 12 hr. in vacuum. But it falls to 100 mT at 140 C baking. The general trend of the increase in pollution depth and the upper critical field at the surface with LTB is analyzed with a relation from. [74] valid at 4.2K [46],

$$c_0[at.\%] = 1.475 \cdot 10^{-3} \left(B_{c2}^{surf}\,[mT] - 276 \right) \tag{4.5}$$

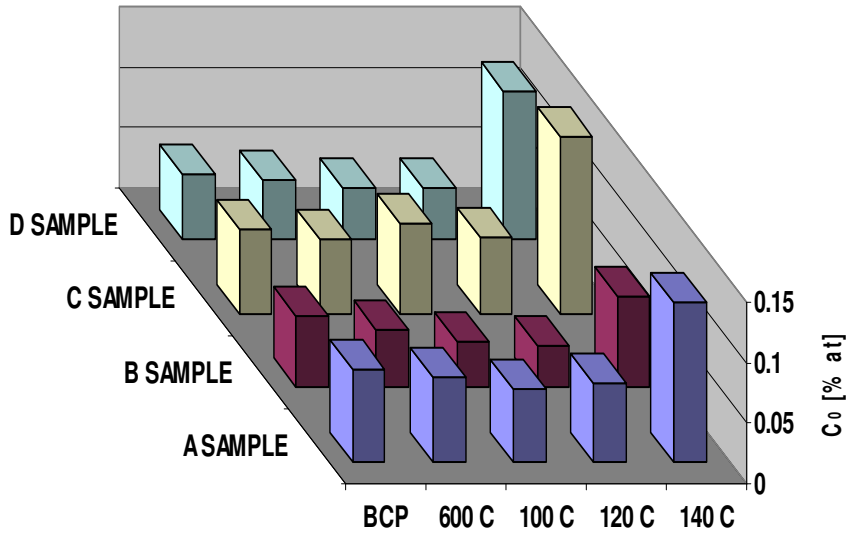

Fig4.7 Surface oxygen concentration [%at] with different surface treatment

Fig.4.7 shows the histogram plot of oxygen concentration change with different surface treatments on all four samples. The figures clearly show the oxygen concentration in the surface layer attains a minimum value in the temperature range of 100-120^{0}C. This might be one of the reasons that the bake around 120^{0}C improves the SRF cavity performance.

4.3.2 Result of Fine Grain Niobium Samples

The surface pinning measurement of the fine grain sample is conducted after each surface treatments. The details of the surface treatment are shown in Table-2. The test was started with the baseline frequency of 267 kHz for sample 'a'. A 30 nF external capacitor is being used during the experiment and it was fixed throughout each and every measurement. The decrease in frequency in all subsequent tests after the baseline measurement is due to the material removal of the sample in each step by BCP. As the material is removed the gap between the pick-up coil and the sample rod increases and hence inductance of the oscillator increases. The increase in inductance causes a down shift of the oscillator frequency. The measurement of the change in oscillator frequency with the increasing and decreasing magnetic field at 2K and 4.2K are shown in Fig.4.8 and 4.9 respectively. Fig.4.8 and 4.9 clearly shows that the irreversibility between H_{C1} and H_{C2} reduces in each step of purifying the fine grain samples. As described in section 4.3.1.1 this irreversibility is a direct consequence of the surface impurity and those impurities acts as a pinning centers. It obvious from 2K and 4.2K measurement the after the post-purification at 1250^0C the irreversibility almost vanishes. A subsequent BCP after 1250^0C in sample'd' further reduces the irreversibility area. The 1250^0C post purification was done using titanium as getter material and it forms a layer of titanium oxide as the Ti layer getters the oxygen from the bulk of the Nb towards the surface during the heat treatment. So the subsequent BCP after the post purification dissolves the titanium oxide and hence the irreversibility area reduces between H_{C1} and H_{C2}. Fig.4.10 shows how the surface oxygen concentration reduces as derived from eqn.4.5. It is clearly seen that the surface oxygen concentration significantly goes down after the 1250^0C post purification.

Sample 'a'

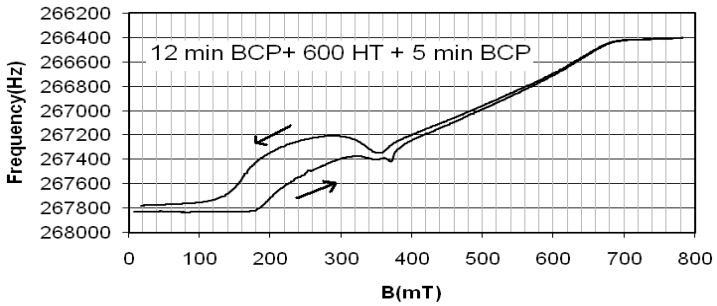

Sample 'b'

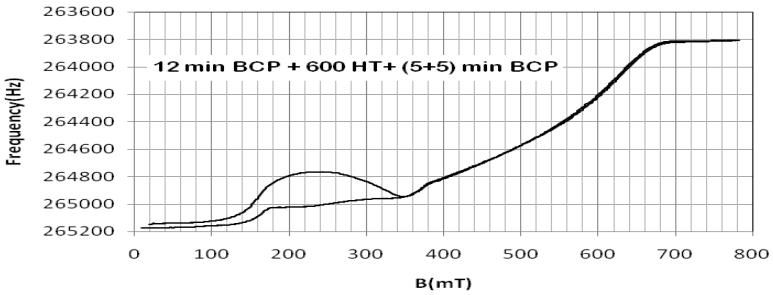

Sample 'c'

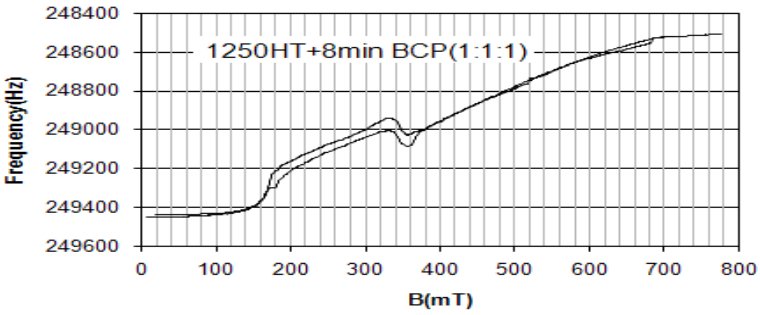

Sample 'd'

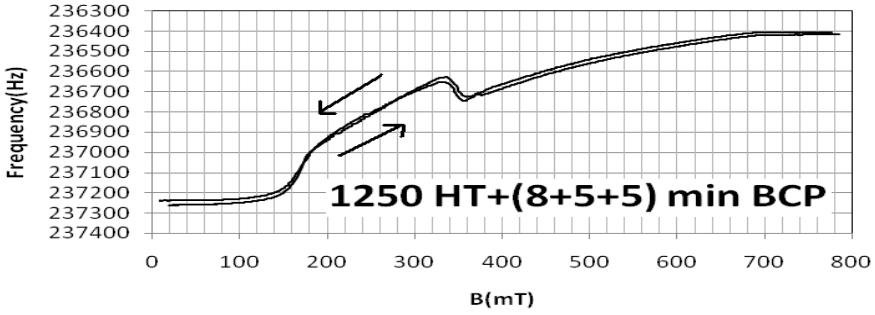

Fig.4.8 Surface pinning measurement at 2K

Sample 'a'

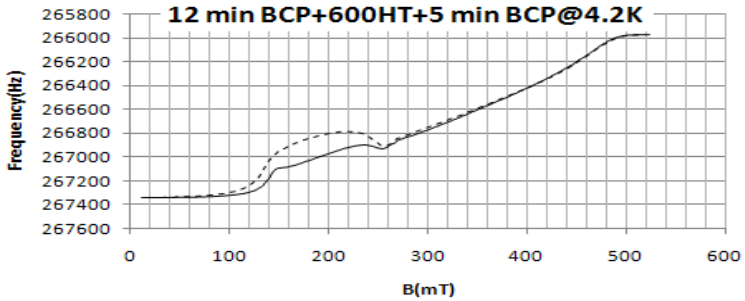

Sample 'b'

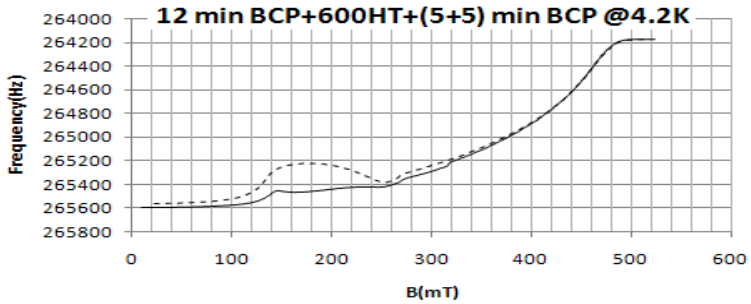

Sample 'c'

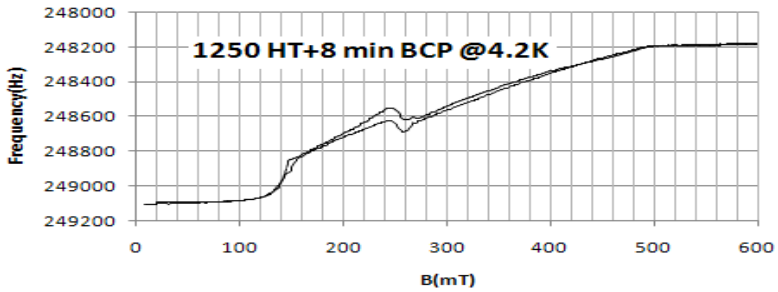

Sample 'd'

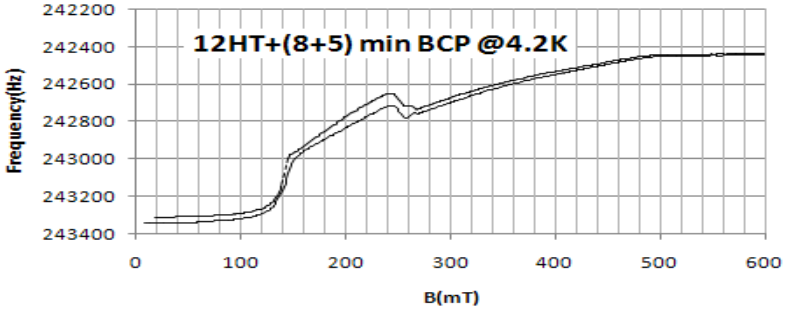

Fig.4.9 Surface pinning measurement at 4.2K

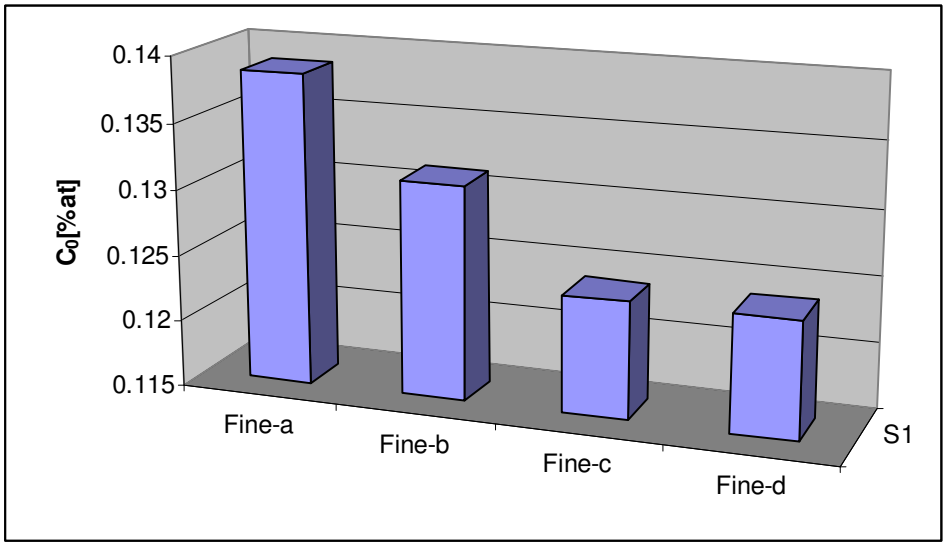

Fig.4.10 Surface oxygen concentration [%at] with different surface treatment in polycrystalline niobium sample.

4.4 Penetration Depth Measurement

4.4.1 Theory of the Experimental Determination of Penetration Depth

The experimental system used for the measurement change in penetration depth already discussed in chapter 3 and the method used is same as the Schawlow and Devlin method [75] and is described below.

The superconducting sample rod acts as a core for the pickup coil surrounding the niobium sample. The inductance of the pickup coil containing the niobium sample is proportional to the cross sectional area occupied by the magnetic flux lines. This includes the space between the coil and the sample rod, plus whatever distance the flux penetrates the sample. Once the sample is in superconducting sample i.e. the sample temperature is below the critical temperature T_c the magnetic flux only penetrates a certain distance from the surface of superconductor named as

penetration depth. The penetration depth is function of temperature of the sample ($T<Tc$). Hence with the change in temperature the penetration depth changes and thus the inductance of the assembly changes. The change in penetration depth is given by the following equations [75],

$$d\lambda = -(1/BR)(1/f^2)(df/f) \tag{4.6}$$

Where f is the oscillator frequency, R is the sample radius and B is constant determined by the relation $\frac{1}{f^2} = BR^2 + C$, where C is the interception of the straight line fit.

A plot of $1/f^2$ Vs R^2 is a straight line and the constant B is obtained from the slope of the curve. The value of B and the calibration curve is shown in Fig. 4.11.

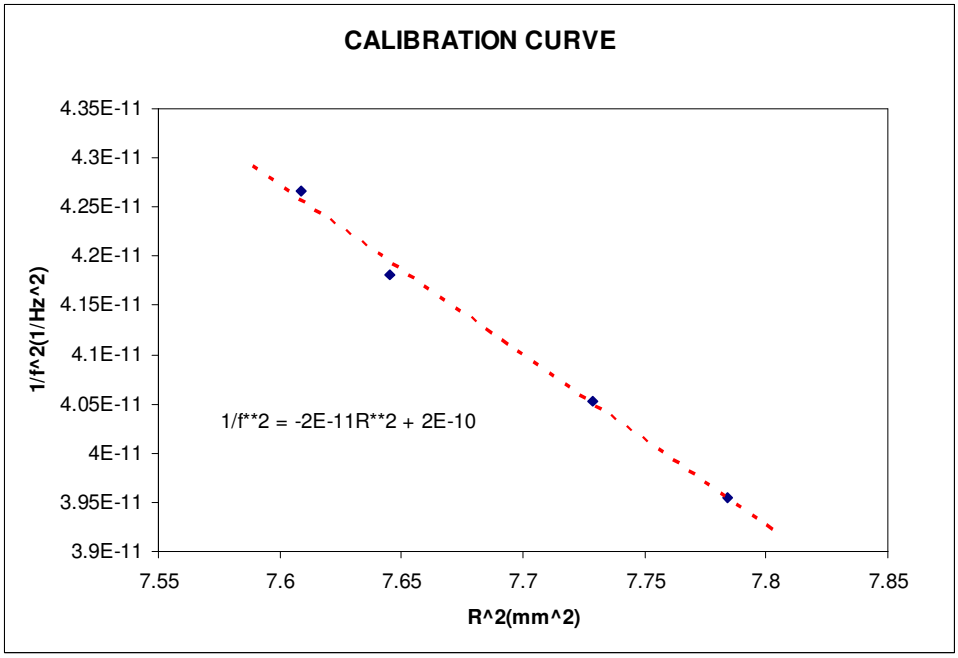

Fig 4.11: A plot of $1/f^2$ Vs R^2

4.4.2 Experimental Results and Effects of LTB

Fig.4.12 shows how the change in penetration depth (Δλ) depends on the parameter y = $1/\sqrt{\left[1-(T/T_C)^4\right]}$. The slope of λ(y) represents the penetration depth at 0 K in the two-fluid model. As the LTB temperature is increased the slope of $d\lambda/d\,y$ decreases till 120^0C. At 140^0C baking the slope $d\lambda/d\,y$ increases at a faster rate resulting in a dirtier surface with decreased mean free path (mfp). In 100 and 120 C the slope continuously decreases meaning that diffusion of surface impurities toward the bulk and dilution of impurity concentration. The faster increase of the slope at 140 C might be due to the partial Nb_2O_5 layer dissociation and thereby increasing the impurity concentration at the surface resulting in a lower mfp. The surface magnetization measurement in section 4.3.1.2 further corroborates this fact as the bulk H_{C2} starts increasing at 140 C baking. BCS theory predicts that Δλ as a function of y is linear. The present measurement shows that the dependence is not quite linear. All the measurements show that the Δλ(y) characteristics have two slopes one at lower temperature (~7K) and the other at higher temperature. As discussed in Ref. [76] the general equation of penetration depth λ (T) for all values of mfp l and taking into account the random scattering is given by,

$$\lambda = \pi\left\{\int_0^\infty \ln\left[1+q^{-2}K(q)\right]dq\right\}^{-1} \tag{4.7}$$

Where *K (q)* is obtained from the Fourier transform of the current density,

$$j(q) = -\left(\frac{c}{4\pi}\right)K(q)a(q) \tag{4.8}$$

where *a (q)* is the Fourier component of the vector potential. Intuitively from our experimental *Δλ(y)* measurement it can be said that the condition $l \leq \xi_0$ is satisfied as shown in Fig.4.12. The theoretical *Δλ –y* curves are plotted for $l \leq \xi_0$ as described in Ref.[76].The theoretical curves clearly shows that the mfp increases from 100^0C to 120^0C baking and reaching close to l= ξ_0. But these fits deviates at around y = 1.5 with a nonlinear slope till y =1 and deviation is large in BCP, 140 C surface treatments compared to other surface treatments like 600 C degassing, 100 and 120 C baking. As explained by Miller in Ref. (76) this deviation is determined by the parameter $2l/\pi\xi_0$ and the lower the value of this parameter the higher is the deviation in λ from the linear fit in the range of y = 1 to 1.5. The baking at120 C do not show any such nonlinear behavior in the range of y = 1 to 1.5.This qualitatively implies that the initial surface impurities diffuse towards the bulk and the addition of oxygen due to the Nb_2O_5 dissociation is negligibly small resulting in an overall increase of the mfp which in turn reduces the nonlinearity in the penetration depth curve.

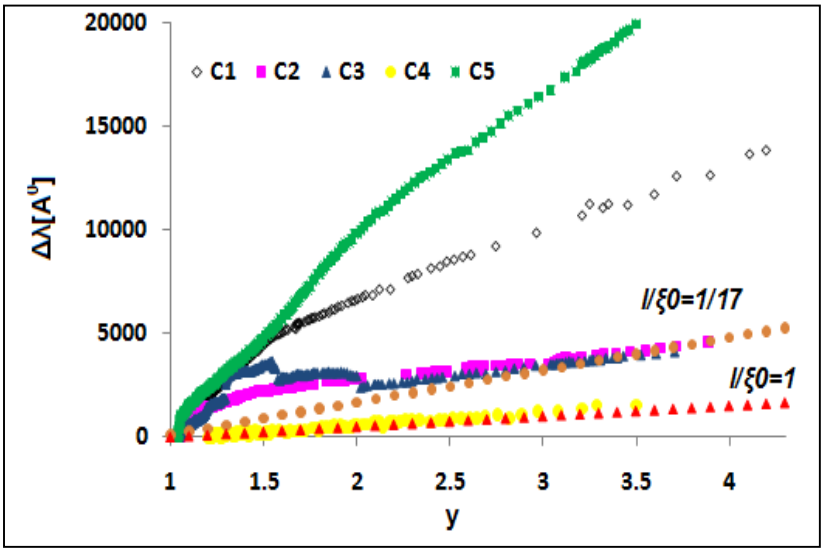

Fig.4.12 *Δλ(y)* measured on large grain sample C after different surface treatments.

4.5 Conclusion

The bulk properties of the large grain samples such as T_C, B_C, H_{C1} and H_{C2} were essentially unchanged with surface treatments such as BCP, LTB. Surface pinning measurement shows that the H_{C3} value increases with the increased LTB temperature, in agreement with the results in [45]. It also shows that the surface H_{C1} is lower than the bulk H_{C1} and that the highest surface H_{C1} was obtained after baking at 120°C for 12h. The irreversibility between H_{C1} and H_{C2} decreases significantly with the low temperature baking, thus a reduction in the surface pinning centers can be inferred. The ratio of H_{C3}/H_{C2} increases with the increased LTB temperature. The data has been analyzed with the Schmidt's model taking into account the low temperature correction to H_{C3}/H_{C2} ratio. The enhanced H_{C3}/H_{C2} ratio has been interpreted as the increased contaminated surface layer thickness. This fact is further corroborated by the penetration depth measurement.

The bulk magnetization measurement shows that the post purification treatment at 1250^0C increases the H_{C1} value and decreases the H_{C2} value. The surface magnetization measurement indirectly shows that the impurity on the surface layer of 10 μm continually reduces as the irreversibility area between the H_{C1} and H_{C2} reduces.

Chapter 5

Defect Depth Profiling by Positron Annihilation Spectroscopy

5.1 Experimental Setup

The positron beam facility at Radio Chemistry Division, BARC [77] provides monoenergetic positron beam of maximum 50 keV and with beam intensity of 10^4 positrons/sec. The positrons are obtained from β^+ decay of ^{22}Na isotope. ^{22}Na has many advantages namely, long half life (2.6 a); short biological life (3 d); relatively cheap; effective (> 90% in β^+ decay); easy to handle in water solution as ^{22}NaCl or $^{22}Na_2CO_3$. The decay β^+ of ^{22}Na is shown below and the decay scheme along with the energy distribution is shown in Fig.5.1.

$$^{22}Na \rightarrow {}^{22}Ne + \beta^+ + \nu_e + \gamma_{(1.27MeV)} \quad (5.1)$$

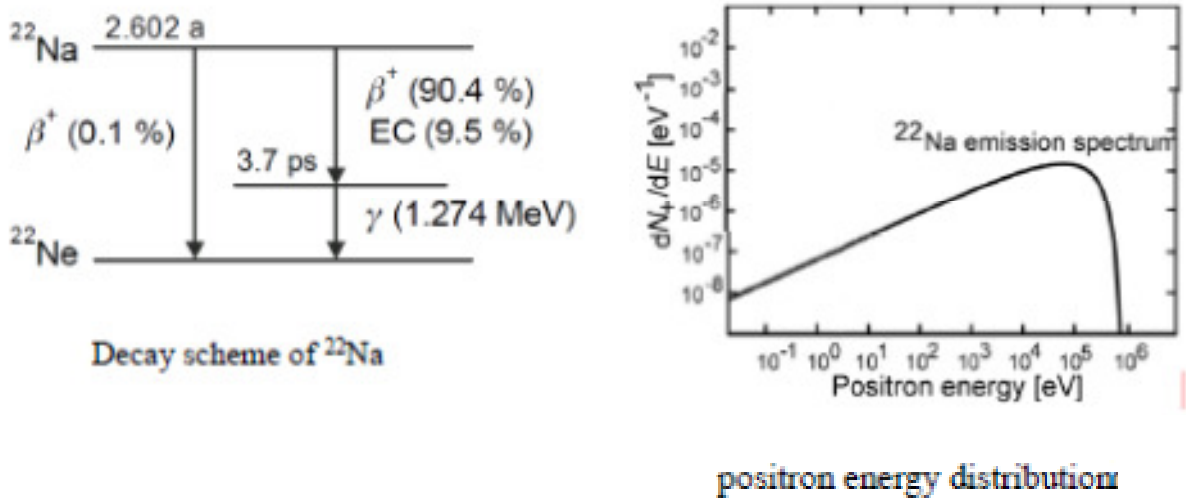

Fig.5.1 The decay scheme and the emission spectrum of ^{22}Na [78].

A study of the defect density as a function of depth was carried out using a slow positron beam. The experimental system is shown in Fig. 5.2. Positrons from a 50 mCi ^{22}Na source were moderated by a 1μm tungsten foil and guided to the target chamber with the help of electric and magnetic field. The acceleration was done by floating the target to the required voltage. The depth dependent Doppler broadening measurements were carried out in the energy range 200eV to 20.2keV. A high efficiency high purity germanium detector with a resolution of 2.0 keV at 1332 keV photopeak of ^{60}Co was used for Doppler broadening measurements and approximately half a million counts were acquired under the 511 keV photopeak at each energy. The ratio of counts within ~ 2.0 keV energy window centered at 511 keV to the total photo peak area was used to evaluate the *S*-parameter. Similarly *W*-parameters were evaluated by taking the ratio of counts within ~ 5.0 keV energy window in the high momentum region to the total peak area.

Fig.5.2 Slow positron beam facility at RCD, BARC

Two parameters $S=A_S/A_0$ (sharpness) and $W=A_W/A_0$ (wing) usually characterize the annihilation line shape. A_S, A_W, A_0 are respectively the central, the lateral and the total area of the annihilation line as shown in Fig.5.3. In the case where positrons are trapped in vacancies their lifetime is increased and the annihilation is preferentially done with valence electrons (small momentum), due to a lack of core electrons (high momentum), giving a smaller Doppler shift and a narrow line (Fig.5.3). Although that annihilation line is the superposition result of free and trapped positrons, S (W) plot gives specific information on a defect-rich sample (S↑, W↓) [79].

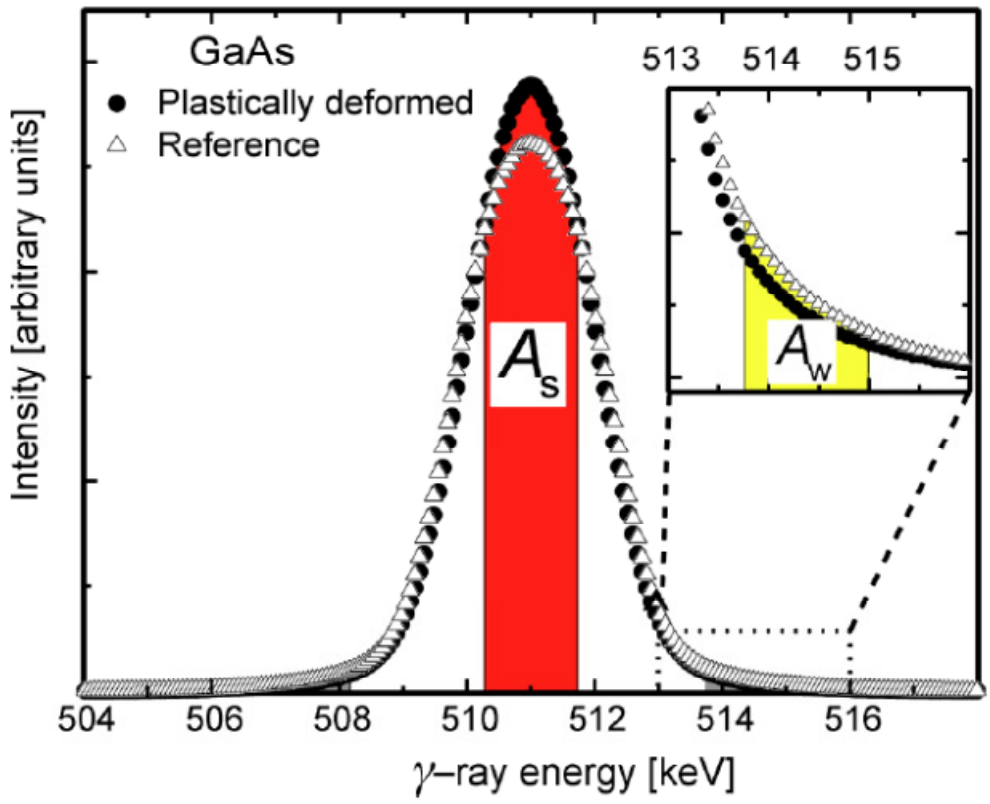

Fig.5.2 Doppler broadening spectrum of positron annihilated gamma radiation [78]

The implantation profile of mono-energetic positron beam as a function of implantation depth and the mean implantation depth as a function of positron beam energy is given by the following equations and named after Makhov [78],

$$P(z,E)=\frac{mz^{m-1}}{z_0^m}\exp\left[-\left(\frac{z}{z_0}\right)^m\right] \tag{5.1}$$

With,

$$z_0=\frac{AE^{\alpha}}{\rho\Gamma\left(1+\frac{1}{m}\right)} \tag{5.2}$$

Parameters A and α are material dependent; ρ is the mass density and Γ the gamma function. The mean implantation depth z_m and Makhov profiles are plotted in Fig.5.3 and Fig.5.4 with these parameters for niobium: A=2.95 μg cm^{-2} $keV^{-\alpha}$, α=1.7 and ρ=8.57 g cm^{-3}.

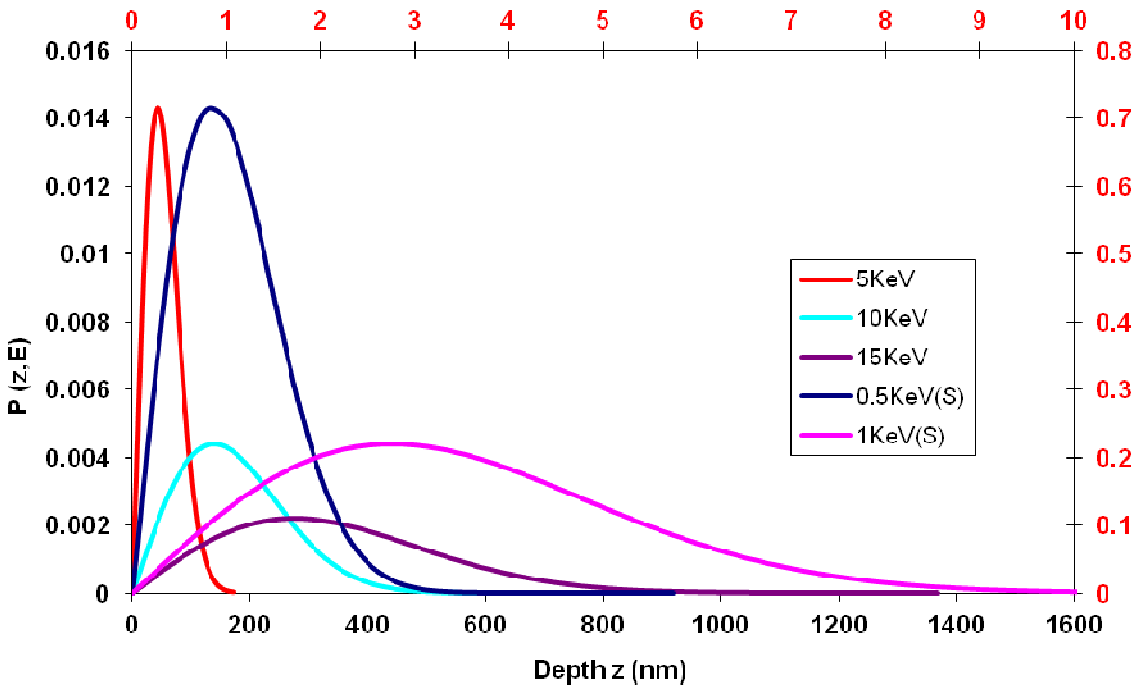

Fig.5.3 Makhov profiles of positron penetration in Nb for different beam energies.

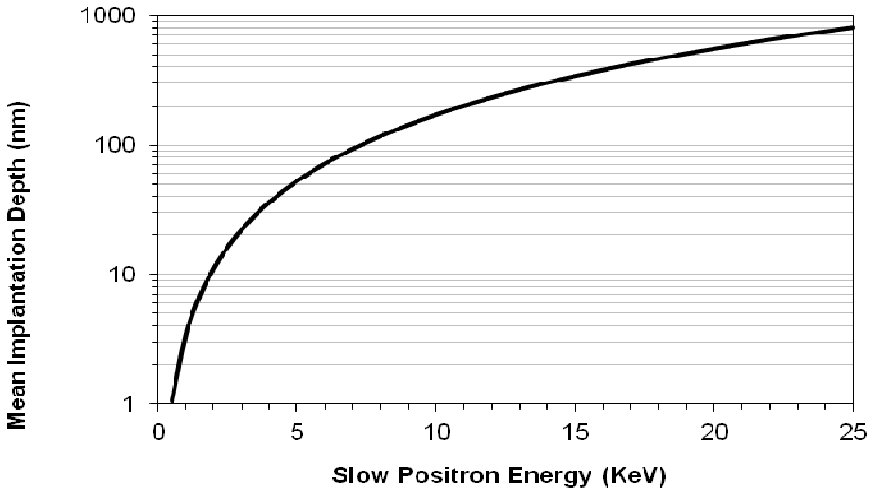

Fig.5.4 Mean implantation depth in niobium

5.2 Large grain niobium samples and treatments

Ingot- B from CBMM was cut by wire EDM to a size of 1mm x 1mm square with a thickness of 3 mm. Then the sample was treated in two steps as described below.

A. The sample was first chemically polished with a mixture of HF, HNO_3, H_3PO_4 in a volumetric ratio of 1:1:1. About 180 μm is removed from the outer surface of the specimen.

B. In the second phase of the experiment the sample was heat treated at 600 ^{0}C for 10 hour in a vacuum of the order of 10^{-5}Torr. This was done to degas the hydrogen from the sample.

6.3 Experimental Results and Discussions

The slow positron beam depth profiling on BCP sample (Ingot B) and on the heat treated sample (Ingot B) are carried out in the positron beam energy range of 200 eV to 20.2 keV. The maximum energy of 20.2 keV corresponds to a mean implantation depth of 471 nm and this mean-implantation depth is very much greater than the London penetration depth of 50nm. The S parameter measurement of the BCP sample and the heat treated sample is shown in Fig.5.5 and Fig.5.6.

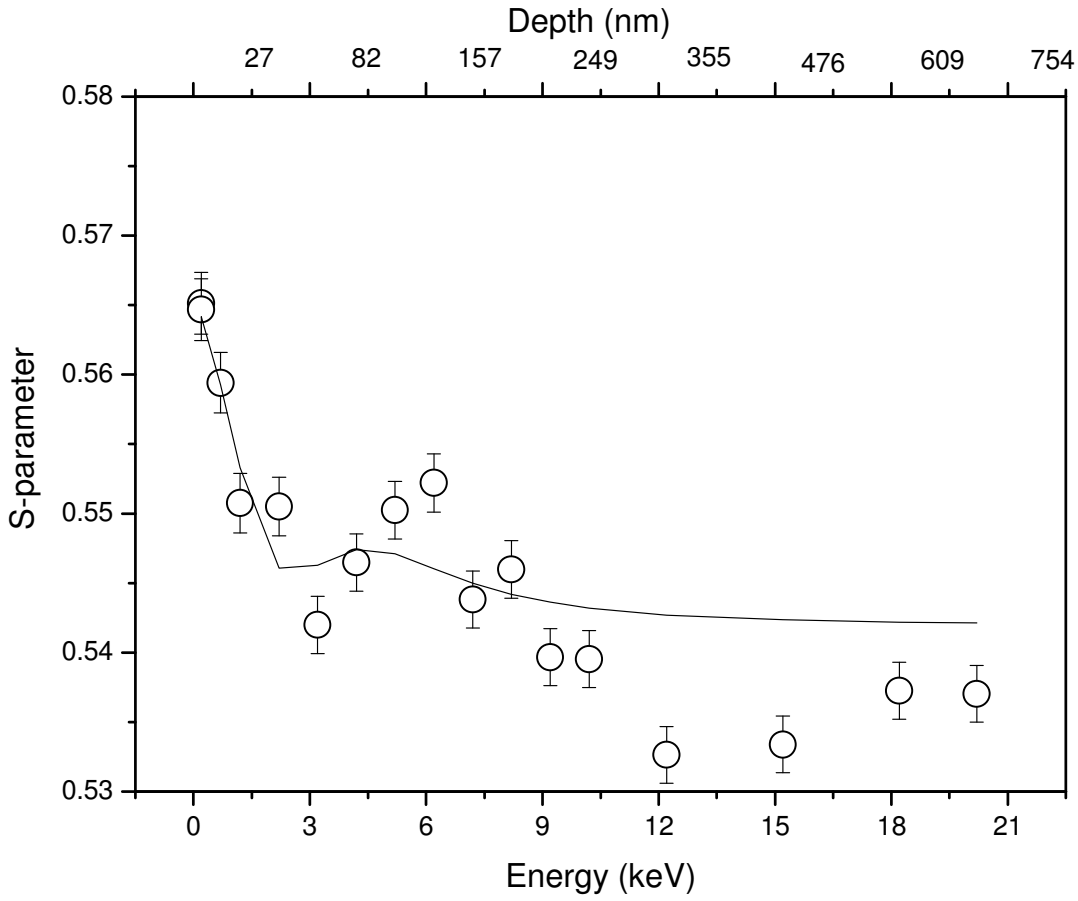

Fig.5.5 Variation S parameter with the positron beam energy vis-à-vis the defect depth of the BCP sample

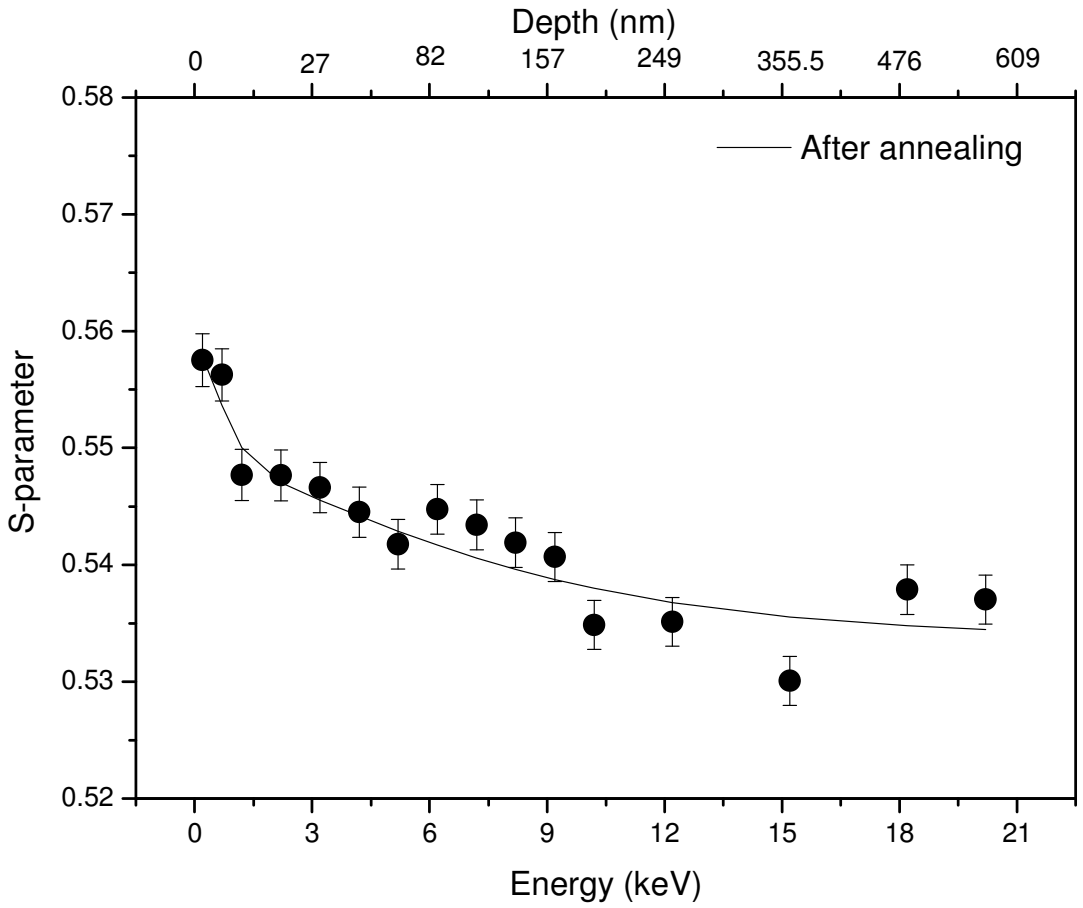

Fig.5.6 Variation S parameter with the positron beam energy vis-à-vis the defect depth of the 600^0C heat treated sample

The line shape parameter or the S parameter dependence on the positron energy is fitted with the VEFIT software package. The three layer fitting of the chemically polished sample showed a surface layer of 79 nm thick has the diffusion length of 65 nm, from 79 nm to 100nm layer has a diffusion length of 0.5 nm and the bulk of the sample have a diffusion depth of 7.4 nm. After annealing it shows a surface layer of 10 nm with diffusion length 39.4 and the bulk is having a diffusion length of 139 nm. The thermal positrons behave as free charge carriers and can be described by diffusion theory, presented below [80]. The positron diffusion length is,

$$L = \left(6D\tau\right)^{1/2} \tag{5.3}$$

where *D* denotes the positron diffusion constant and τ the lifetime in the lattice. Typical diffusion lengths are of the order of 100 nm, which corresponds to a few hundred atomic layers [84–87]. Trapping centres such as neutral or negatively charged vacancy defects have deep bound positronic states, and hence act as efficient "drains" for the diffusive positron, decreasing the diffusion length and affecting the lifetime [80,88]. Eventually, annihilation takes place with one of the electrons.

It has been observed that after annealing the diffusion length decreases within a surface layer of 10 nm which implies an increase in the defect density at the surface layer. But in the bulk of the Nb sample an increase in diffusion length suggest the overall reduction in defect density. So the vacancy rich surface layer is much smaller than the RF penetration depth of 50 nm. It is well known that the 600^0C heat treatment is to remove the hydrogen from the bulk of the niobium. This might be due to the hydrogen degassing which when comes out of the specimen leaves open volume defect within the sample. Hydrogen in a perfect Nb lattice occupies tetrahedral interstitial positions [89]. Vacancy represents a potential well for hydrogen and trapping of hydrogen in a vacancy was observed [90-92]. Thus, the hydrogen lowest energy sites are changed in Nb crystal containing vacancy. During the BCP Hydrogen is absorbed by the niobium surface from the aqueous solution by the following mechanism [93],

$$\boldsymbol{6\,Nb + 10\,HNO_3 = 3\,Nb_2O_5 + 10\,NO + 5H_2O}$$

and

$$\boldsymbol{Nb_2O_5 + 10\,HF = 2\,NbF_5 + 5\,H_2O}$$

then

$$3Nb + 5\,HNO_3 + 15\,HF = 3\,NbF_5 + 5\,NO + 10\,H_2O$$

Any vacancy in the perfect niobium lattice is more favorable for the hydrogen atoms to accumulate.

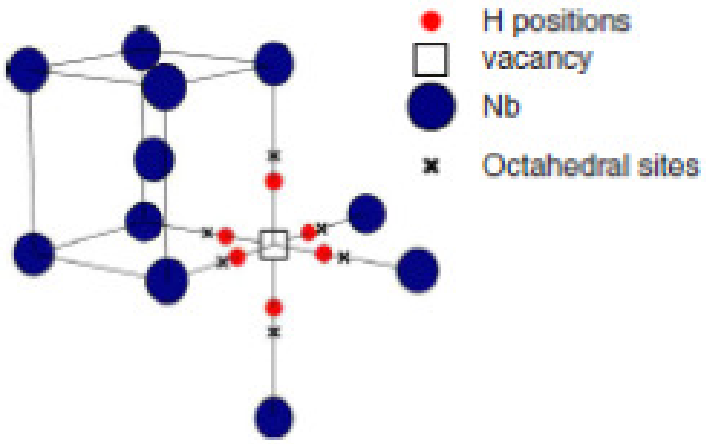

Fig.5.7 Schematic drawing of six crystallographically equivalent positions of hydrogen trapped in the vacancy site [94]

A pictorial representation of the single hydrogen trapped around a niobium vacancy is shown in Fig.5.7. The hydrogen absorbed during the BCP form a hydrogen vacancy complex in Nb. So during 600^0C annealing when hydrogen comes out from the bulk of the material it exposes the vacancy sites. Hence this could be a probable explanation of enhanced vacancy sites after the 600^0C annealing. So it could be expected that during LTB since there is no dissociation of the Nb_2O_5 dielectric layer more vacancy sites are exposed as the surface hydrogen vacancy complexes migrates towards the bulk [79].

Chapter 6

Design, Fabrication and RF test of β=0.49, 1050 MHz Single Cell Fine Grain and Large Grain Elliptical Cavity

6.1 Introduction

A high current proton linear accelerator (linac) is an integral part of ADSS. This linac (1 GeV, 30 mA) essentially consists of three parts, the low energy, the intermediate energy and the high energy. In the low energy part protons are accelerated through RFQ and CC-DTL to 10-20 MeV. The front end (linac injector) is comprised of an ion source and radio frequency quadruple (RFQ) accelerator. The ion source is supposed to deliver high brightness beams (intensity, emittance, stability). The RFQ includes RF electric transverse focusing bunches and can accelerate the beam from about 100keV to few MeV. These structures are well suited to keep the beam quality (longitudinal and transverse) at high intensity. After this the beam passes trough CC-DTL which provides acceleration up to 10-20 MeV. The intermediate section makes use of CC-DTL and CCL up to 70-100 MeV. These structures are normal conducting drift tube linac structures. In the high energy part, RF superconducting elliptical cavities accelerate protons up to 1 GeV. Superconducting cavities have many advantages over their normal conducting counterparts. As the superconductor has low surface resistance (~ $n\Omega$), only a little energy is required to achieve high accelerating fields. Nearly all the high frequency power available can be used to accelerate the particles. Second advantage comes from the geometry of the cavities. The iris opening is large in the low frequency regime. Therefore, the interaction - via so called wakefields - with the particle beam is smaller than the normal conducting higher-frequency accelerators. The bore radius with large aperture helps in the removal of higher ordered and trapped modes from the

beam tube. This is to limit the extent of particle oscillations, which are resonantly driven by bunch core oscillations induced by the mismatch in the linac. Hence, the accelerated proton preserves its beam quality at the end of the accelerator.

In the high energy section (> 100 MeV) of an ADSS accelerator, superconducting elliptical cavities accelerate protons up to 1 GeV [95]. After the successful completion of the Spallation Neutron Source (SNS) in the USA, the superiority of superconducting (SC) linacs over normal conducting ones is well accepted in the accelerator community to accelerate proton beams efficiently with velocity relative to the speed of light and β of about 0.5 [96]. Short, independently phased SC resonators with large velocity acceptance are also ideal for the efficient acceleration of the beams with different mass-to-charge ratio. SC cavities are ideal for low current beams, where efficiency is dominated by RF losses. In the high beam loading limit (~100mA), NC and SC linacs have comparable efficiency. Even for low- β□□ proton beams SC linacs can also be cost effective. In the studies for the EURISOL, 5 mA cw proton driver [97], a comparison between NC and SC option between 5 and 85 MeV was carried out. The results of the studies showed a similar construction cost.

6.2 Measurement of Mechanical properties of large grain niobium

Large grain niobium has many potential advantages over fine grain material. During the production of ingot niobium it is slowly cooled and as a result of that several large crystals are formed at the middle surrounded by small size crystal of niobium around the periphery. As grain boundary are preferred locations for the segregation of interstitial impurities, the critical field might be locally reduced. Furthermore, differential etching for different crystal orientations result in,a “step” along the grain boundary which could lead to a geometric magnetic field

enhancement and a premature quench. These may limit the final cavity performance. In any case, a great advantage of large grain material is the low production cost with respect to fine grain material. The cells of the cavities are formed by deep drawing of a flat circular plate. During deep drawing a strain differential is created along the cavity contour. Their magnitude depends on yield stress, the accumulated plastic strain and the hardening behaviour [98]. In this study the uniaxial tensile stress were carried out on four different ingot materials received from CBMM, Brazil.

6.2.1. Experimental System

The experimental system used for the uniaxial tensile test is shown in Fig.6.1. It is ATS make uniaxial tensile test measurement system having following measuring accuracies.

A. Strain measurement accuracies ±2%. The strain rate can be varied from 10^{-6} S^{-1} to 10 S^{-1}.

B. Stress measurement accuracies ±1%.

C. Percentage elongation accuracies ±1%.

Prior to mounting the sample in test fixtures strain gauges were attached to each sample with M-bond adhesive 610. In the experiment the strain gauges being used are precision strain gauges Wk-00-125BB-350. They have a resistance of 350±0.3% Ω, gauge factor of 2.02±1.0% and transverse sensitivity of -1.9±0.3% at 24^0C.

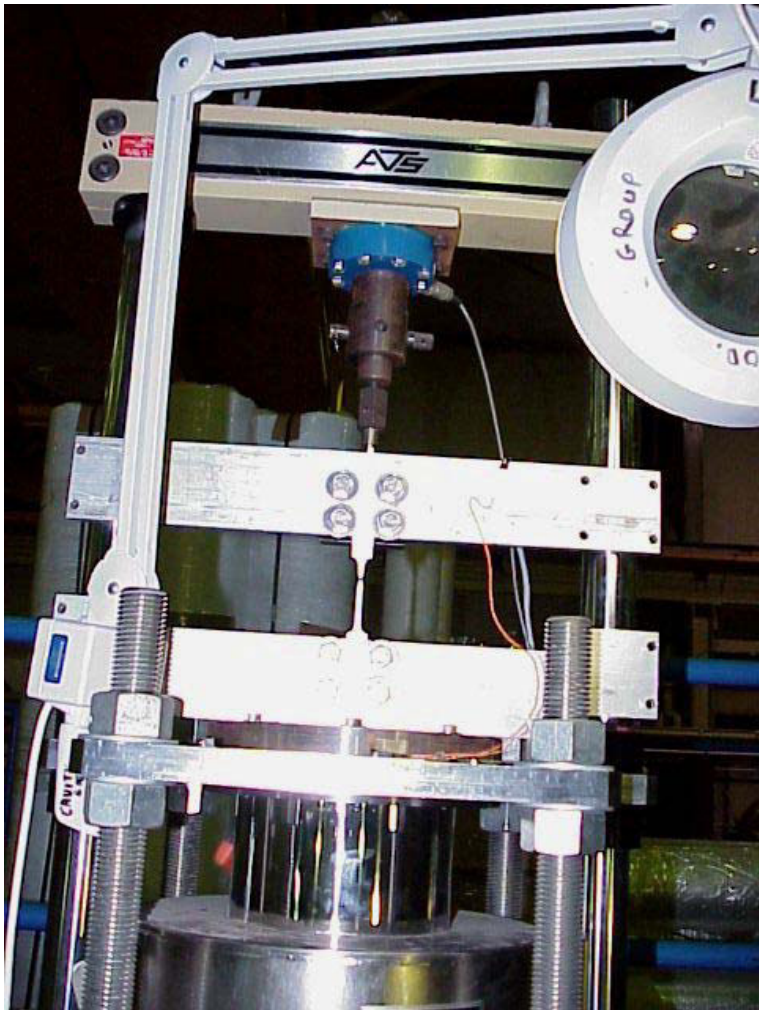

Fig.6.1 Photograph of the experimental setup for the mechanical measurement

Four different ingots are received from CBMM, Brazil. They are having a RRR value of 61, 146, 117 and 99 and named ingot A, B, C and D respectively. From each ingot three sets of samples are cut by wire EDM for tensile test. All three samples of a respective ingot are given different purification treatment. The first sample of a respective ingot is given the ultrasonic degreasing for 30 minutes followed by buffered chemical polishing (BCP-1:1:1) of 180μm. The second one is given a ultrasonic degreasing for 30 minutes followed by buffered chemical polishing (1:1:1) for 20 minutes in two steps of 10 minutes each resulting a removal of material of 120 μm and

finally a heat treatment at 600^0C for 10 hour in a vacuum furnace at a vacuum level better than 10^{-6} mbar. The last sample after ultrasonic degreasing and material removal of 120 μm by BCP(1:1:1) is heat treated at 1200^0C for 2 hour in a vacuum furnace at a vacuum level better than 10^{-6} mbar. The size and the profile of the tensile sample cut for the mechanical measurement is shown in Fig.6.2. The details of the sample are shown in Table 6.1.

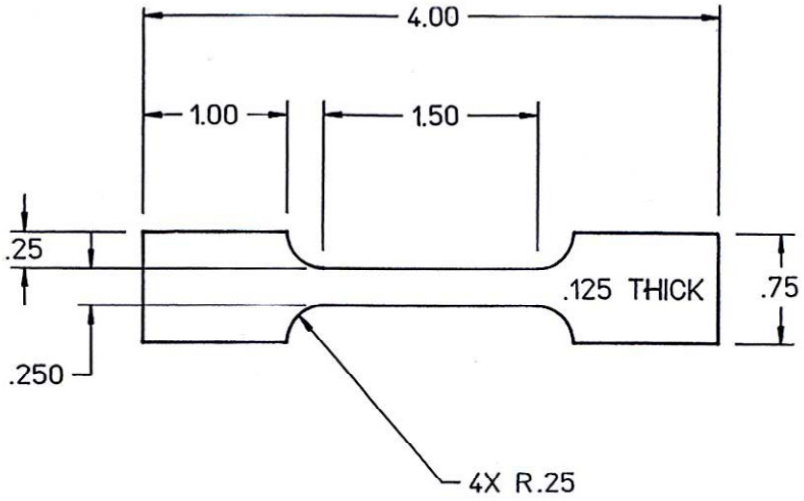

Fig.6.2 Tensile test sample geometry (all the dimensions are in inch)

Table 6.1 Summary of mechanical samples

Samples	Process	RRR
A0	Ultrasonic degreasing 30 min+BCP (1:1:1) 180 μm	61
B0		146
C0		117
D0		99
A1	Ultrasonic degreasing 30 min+ BCP (1:1:1) 120 μm + 600^0C 10 hour heat treatment in a vacuum furnace (≤10^{-6} mbar)	77
B1		158
C1		138
D1		117
A2	Ultrasonic degreasing 30 min+ BCP (1:1:1) 120 μm + 1200^0C 2 hour heat treatment in a vacuum furnace (≤10^{-6} mbar)	Not measured
B2		
C2		
D2		

6.2.2. *Measurement Results*

Stress – strain curve showing yield point, drop of yield point, and plastic flow regime with different treatment like 180 μm BCP, 600^0C heat treatment, and 1200^0C heat treatment is shown in Fig.6.3. No significant change in yield strength is observed after 600^0C hydrogen degassing. It was reported in ref [98] that after BCP the yield strength drops because of hydrogen absorption and the material become soft, but in the present measurement after 600^0C degassing no significant decrease in yield strength is observed. But after 1200^0C heat treatment yield strength reduces for all ingots which are matching with the measurements reported in ref [98]. The load variation with percentage elongation plots for different surface treatments is shown in Fig.6.4. The measured mechanical properties by uniaxial tensile test along with the vicker's hardness values measured during hardness testing is shown in Table 6.2.

From Table 6.2 it is seen that the Vickers hardness doesn't change with various surface treatments for the large grain ingots. But after 600^0C heat treatment it is seen that the % elongation reduces before it reaches to ultimate strength. This is happening because as hydrogen comes out the material turns much harder and its % elongation decreases before it breaks up.

Hence all these mechanical measurements doesn't show up any drastic change in the property but within the experimental error all the properties remain same after various treatments except the change in yield strength after 1200^0C heat treatment.

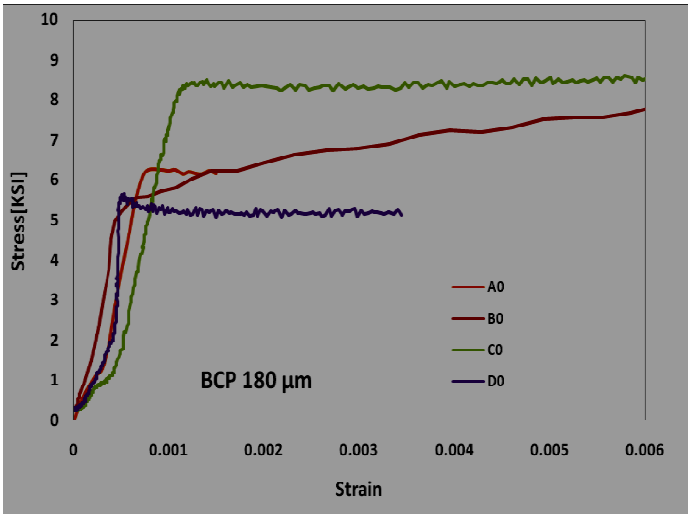

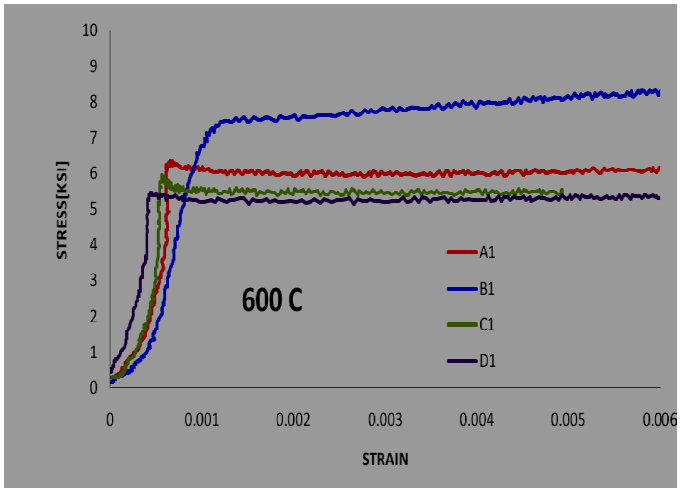

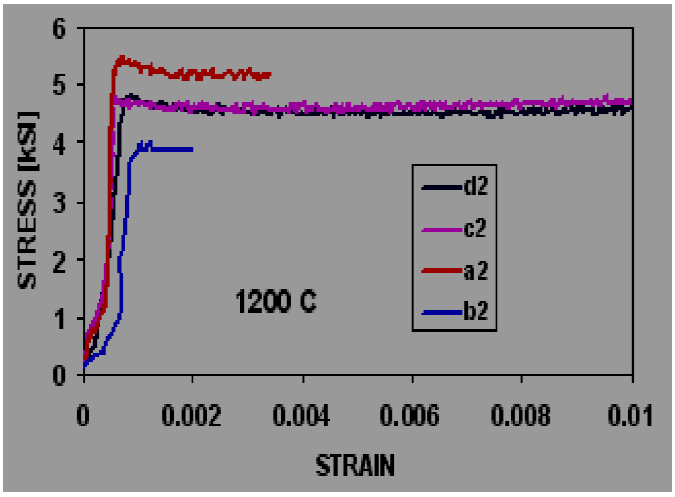

Fig.6.3 Stress Vs Strain curves of the large grain niobium with various treatments.

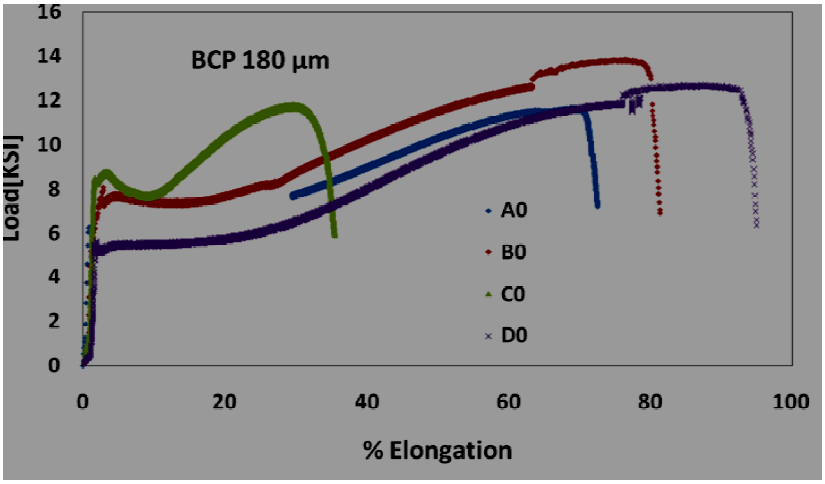

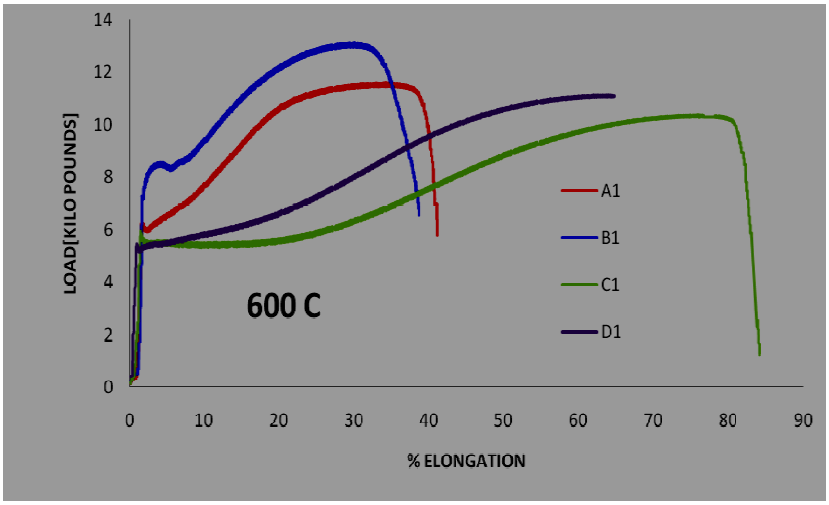

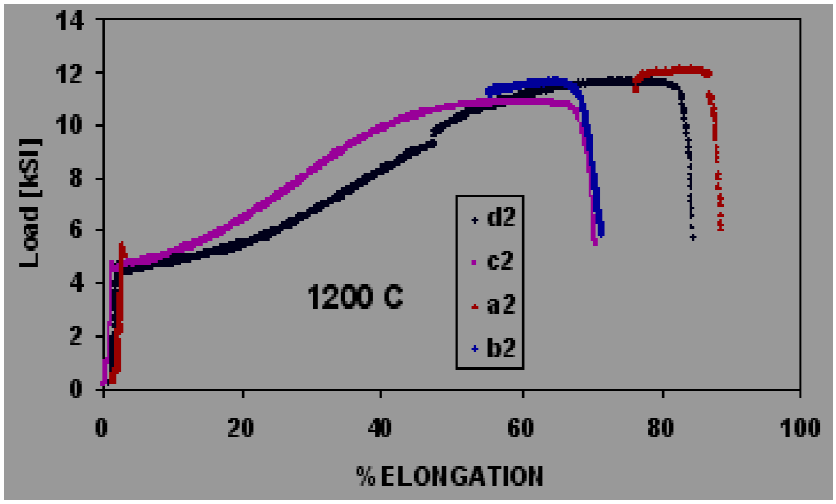

Fig.6.4 Load Vs % elongation plots of the large gain niobium samples with various treatments.

Table 6.2 Values mechanical properties measured after various surface treaments in Large grain niobium.

Sample	Yield Strength[KSI]0.2%	Tensile Strength[KSI]	% Elongation	RRR Measured	Hv
A0	**6.270**	**11.530**	**72**	**61**	**44.6**
B0	**5.6**	**14**	**80**	**146**	**45.6**
C0	**8.4**	**12**	**35**	**117**	**46.6**
D0	**5.7**	**12.4**	**95**	**99**	**47.7**
A1	**6.246**	**11.468**	**44**	**77**	**43.5**
B1	**7.214**	**13**	**43**	**158**	**45.3**
C1	**5.902**	**10.597**	**86**	**138**	**46.1**
D1	**5.421**	**11.04**	**73**	**117**	**45.3**
A2	**5.4**	**12**	**87%**	**X**	**46.5**
B2	**3.8**	**11.4**	**67%**	**X**	**53.3**
C2	**4.8**	**10.5**	**68%**	**X**	**48.3**
D2	**4.7**	**11.3**	**83%**	**X**	**47.5**

6.3 Cavity design

RF parameters of 1050 MHz, β= 0.49 single cell Elliptical cavity was optimized using 2D cavity tuning code SUPERFISH and 3D High Frequency Simulation code CST Microwave Studio for possible use in a High Current Proton Accelerator [99,100]. The low energy section of the ADS accelerator was designed for 350 MHz and therefore it was decided to build the superconducting accelerator section with the third harmonic of 350 MHz i.e. 1050 MHz.

6.4 Optimization of cavity shape variables

The cross section of the right half of an elliptical cavity is shown in Fig.6.5.a. As we see the Fig.6.5.a bore radius is R_b, the cavity diameter is D. The full cavity length is $L = \beta_g\lambda/2$, where the subscript g stand for "geometrical." The cavity includes a circular dome of radius R_c, a sloping straight segment at angle α_w from the vertical, an ellipse near the iris with semiaxes b_I and a_I, and a flat segment of length F_I at the iris. The flat segments at the equator and at the iris are optional (i.e., they can have zero length). The cavity shape optimization of 1050 MHz, β = 0.49 single cell cavity is reported in ref. [99].

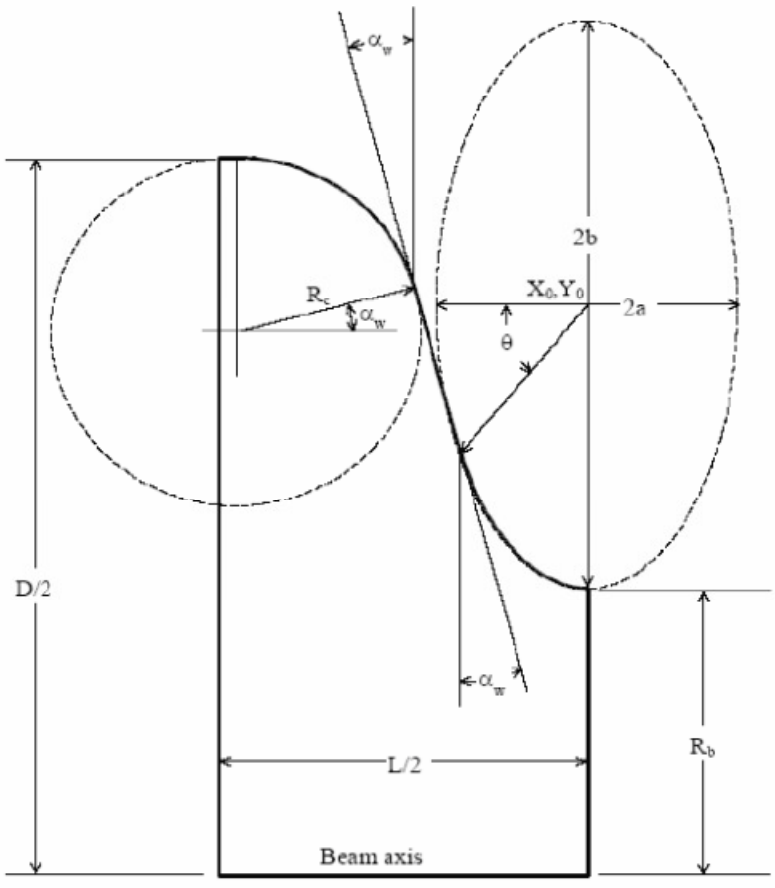

Fig.6.5-a: Symmetric half cavity shape and parameters.

Cell length L is fixed as it determined by β_g value and the design frequency as $L = \beta_g\lambda/2$. But there is a big difference of E_{pk}/E_{acc} between cavities with different β_g values. E_{pk}/E_{acc} depends on β_g value of the cavities. Higher β_g cavity has lower E_{pk}/E_{acc}. The cavity diameter D is used in frequency tuning. Its effects on the cavity electromagnetic characteristics and mechanical properties are insignificant. The final cavity shape after optimization was achieved by varying the dome radius, wall angle, iris ellipse ratio and the bore radius. The variation of E_{pk}/E_{acc} and B_{pk}/E_{acc} with wall angle when the dome radius (R_D), Iris a/b and the bore radius were 2cm, 0.7, 3.9 cm, respectively is shown in Fig.6.5-b.

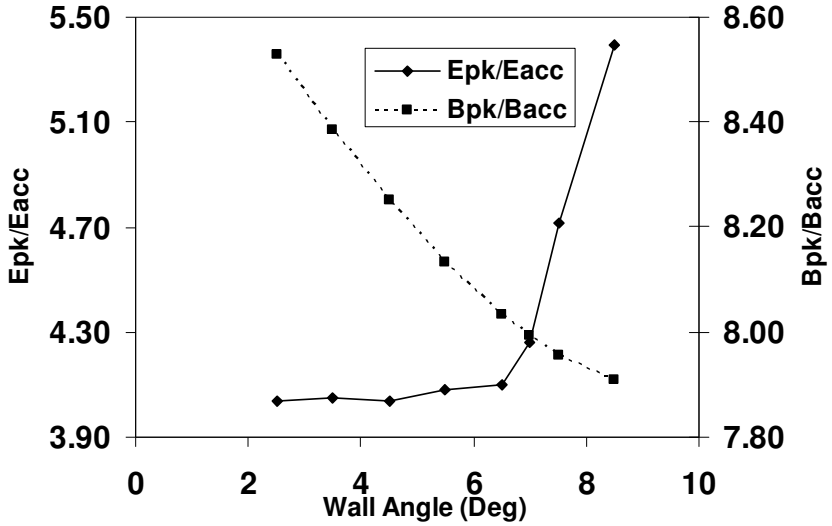

Fig.6.5-b Variation of E_{pk}/E_{acc} and B_{pk}/B_{acc} with the wall angle.

The minimum E_{pk}/E_{acc} was at 6.5^0 wall angle and the B_{pk}/E_{acc} had shown a continuous reduction with the wall angle.

The variation of E_{pk}/E_{acc} and B_{pk}/E_{acc} with iris ellipse ratio is shown in Fig.6.6. For any cavity geometry and parameters, the iris aspect ratio has an optimum value that minimizes the peak electric field with marginal influence on the other electromagnetic parameters.

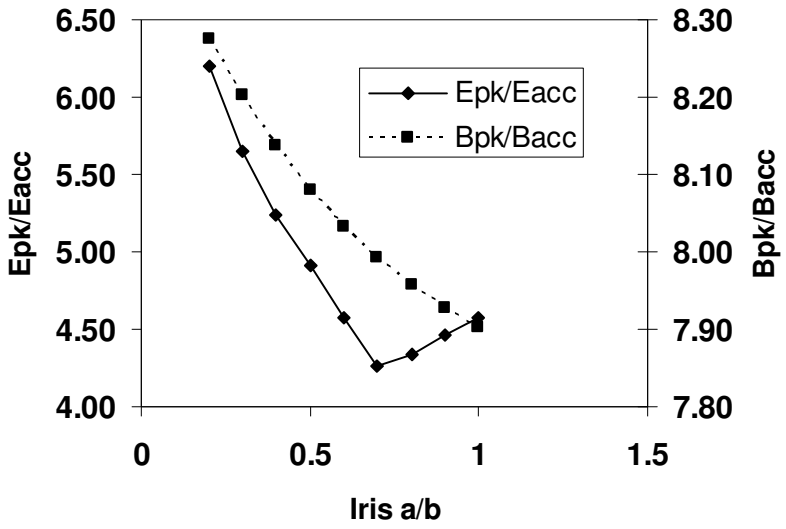

Fig.6.6 Variation of E_{pk}/E_{acc} and B_{pk}/E_{acc} with iris ellipse ratio.

So the iris ellipse a_I / b_I allows to find a local minimum for the peak surface electric field. It was observed that for wall angle 6.5^0, E_{pk}/E_{acc} was minimum at $a_I / b_I = 0.7$. There was a geometrical limitation arises from the radius of curvature in the region of cavity iris. The smallest radius was estimated as 2-3 times larger than a cavity wall thickness.

Bore radius was an important parameter with respect to cavity optimization. It was found that E_{pk}/E_{acc} and B_{pk}/E_{acc} increases with bore radius. The effective Shunt Impedance ZT^2 decreases with R_b and also power dissipation increases with R_b. So a smaller bore radius R_b is preferable. Actually, bore radius R_b should be considered in conjunction with beam dynamics calculations, because, a larger R_b may decreases beam loss and avoids higher order mode trap. For a multi-cell cavity design R_b is determined by the inter-cell coupling. In present case it is 3.9 cm.

In our design the shunt impedance was optimized with the wall angle. The shunt impedance maximized at an wall angle of 6.5^0 and the variation of shunt impedance with the wall angle is shown in Fig.6.7.

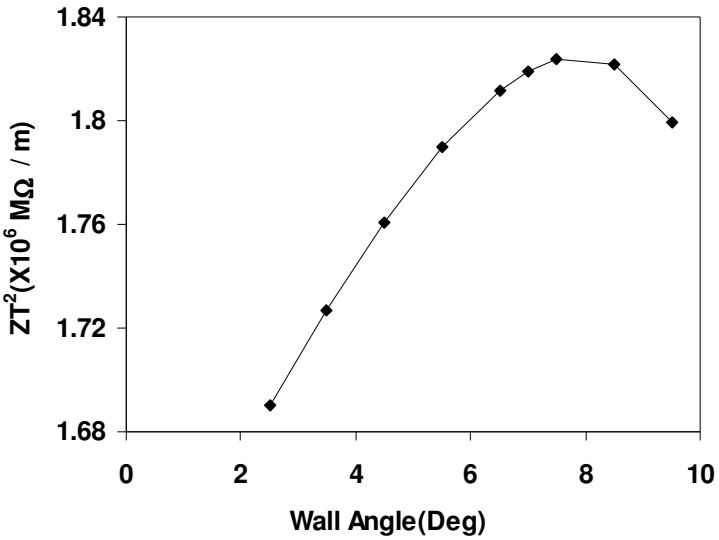

Fig.6.7 Variation of shunt impedance with the wall angle.

6.5 Design parameters of the single cell cavity

A drawing of the single-cell cavity of 1050 MHz, β=0.49 is shown in Fig.6.8, along with the electric field and magnetic field distribution calculated by SUPERFISH and CST-MWS.

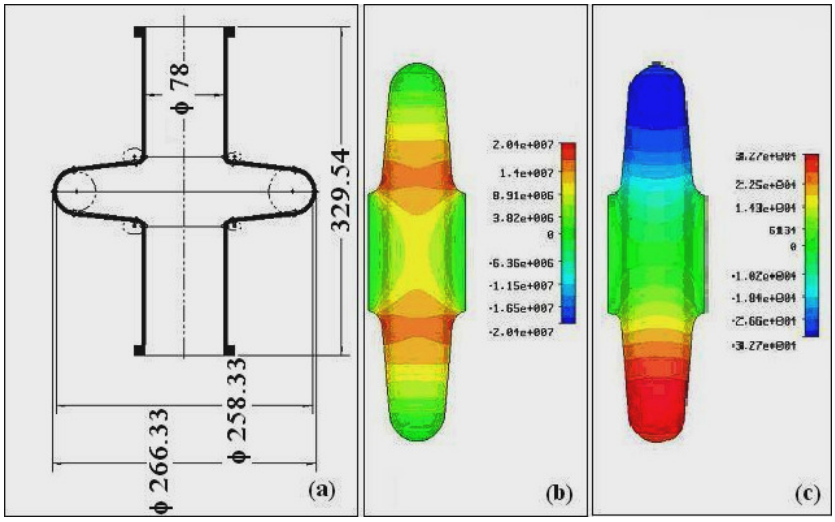

Fig.6.8 (a)Drawing of the 1050 MHz, β=0.49 cavity, (b) Electrical field distribution in TM_{010} mode, (c) Magnetic field distribution in TM_{010} mode.

Our design was compared with the INFN-TRASCO and RIA design [101]. Normally the INFN-TRASCO design adopts an elliptical iris and the shape of elliptical equator whereas in our case the equator shape was circular and the iris shape was elliptical similar to RIA design.

The main cavity parameters of our design are summarized in Table 6.3 and compared with the INFN-TRASCO and RIA design.

Table 6.3 1050 MHz, $\beta = 0.49$ Single Cell Cavity Parameters

Parameters	Present Design	TRASCO Design	RIA Design
Frequency (MHz)		1050	
Geometrical β		0.49	
Iris Radius (cm)		3.9	
Cavity Diameter (cm)		25.833	
Dome Aspect ratio	1	1.6	1.0
Iris Aspect Ratio	1.43	1.3	1.45
Wall Angle (Deg.)	6.5	5.5	6.5
Wall Distance [mm]	7.37	7.0	8.5
r/Q (Ω)	9.19	9.46	9.04
Geometry Factor G (Ω)	141.91	147.387	135.675
E_{peak}/E_{acc}	4.26	4.44	3.98
B_{peak}/E_{acc} (mT/(MV/m)	8.02	7.78	8.37

The above table shows the design comparison with RIA and TRASCO. Actual RIA design was with frequency 805 MHz and geometrical beta 0.47 and TRASCO was with frequency 704.4 MHz and geometrical beta 0.47. In the above table both the RIA and TRASCO design were scaled for frequency 1050 MHz and geometrical beta 0.49, keeping the iris radius same as our

present design(3.9 cm). The present design was very close to the design of those other two cavities. Their prototypes reached their performance specs. In our design the ratios of the peak fields to E*acc* was in between the values of the TRASCO cavity, designed to minimize B*p*/E*acc*, and the RIA cavity, designed to minimize E*p*/E*acc*.

6.6 Fabrication and preparation for RF test

6.6.1 Fabrication

Two prototype single cell Niobium cavities were fabricated with the designed parameters mentioned in Table 6.3. One of the cavities was made from fine grain (grain size ~ 50 μm) niobium sheet of RRR > 250 and the other one was made of the large grain niobium of RRR ≥ 96 received from CBMM, Brazil [102]. The disks for the large grain cavity were sliced directly from the ingot by wire electro-discharge machining. A suitable set of dies were made out of 6061 aluminium to form the cavity half cells from niobium sheet of thickness 4 mm. The schematic and the parts of the different components of the dies are shown in Fig.6.9. The half cells were deep drawn followed by the required machining at the equator and the iris region. All the defects, machine marks were removed by mechanical buffing followed by ultrasonic degreasing and buffered chemical polishing (BCP) ($HF:HNO_3:H_3PO_4$ = 1:1:1 (by volume)). About 30μm from the inner surface of the cavity half cells was removed. The beam tubes for both the cavities were fabricated from a fine grain Niobium sheet of low RRR by rolling and electron beam welding (EBW) along the length of the tube. Then the half cells were EB welded with the respective beam tubes. No difficulties were faced in welding of fine grain beam tubes with the large grain half cells. Finally, equator welding was carried out to form the single cell.

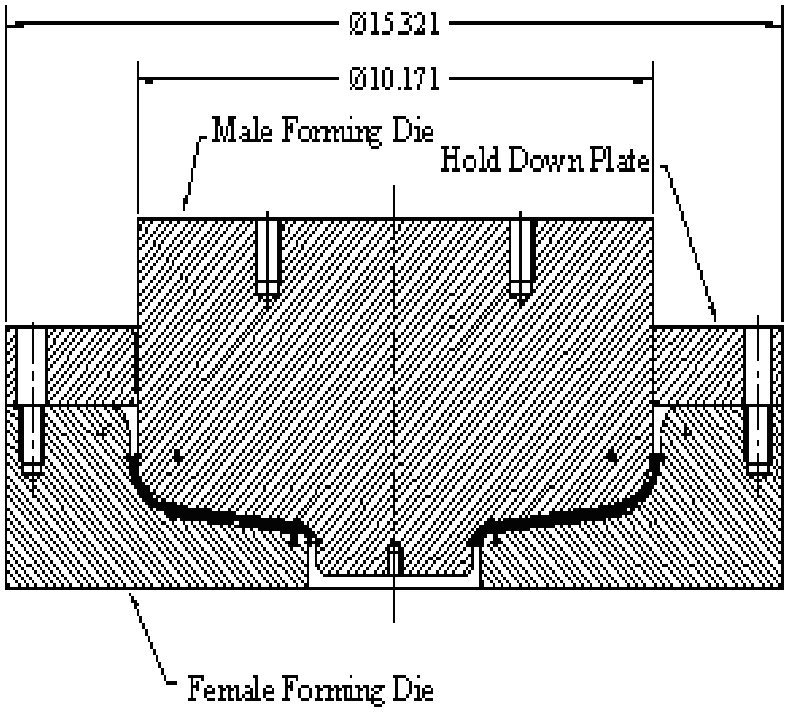

(a)

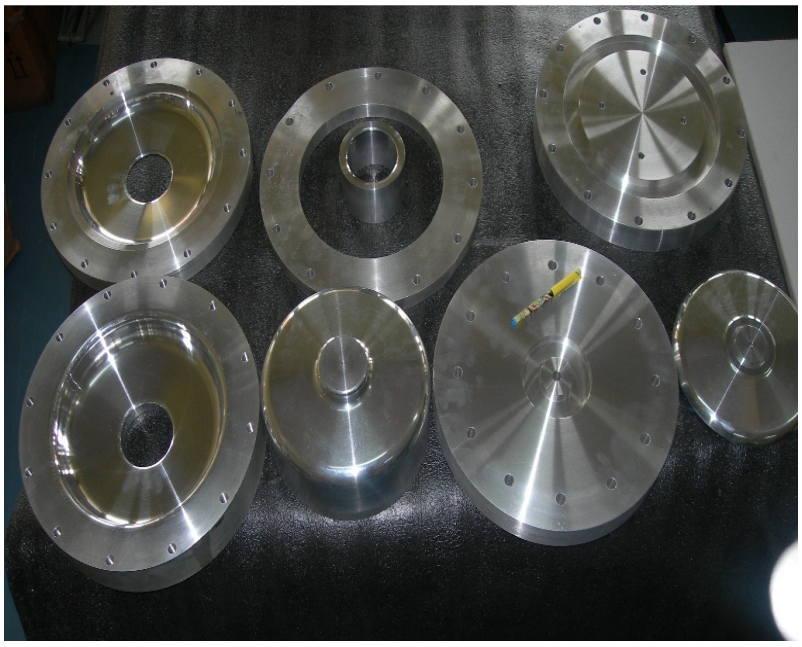

(b)

Fig.6.9 (a) Schematic of the forming die for the 1050 MHz, 4mm thick cavity(dimensions in the figure is in inch), (b) Different parts of the forming die.

6.6.2 Preparation for RF test

Both the cavities were pre-processed with the standard cavity preparation for RF test at 2 K. First, the cavities were degreased for 20 minutes ultrasonically with micro-90 solution followed by buffered chemical polishing (BCP 1:1:1) to remove about 150 μm from the cavity inner surface. Then they were heat treated at 600^0C for 10 hour to degas H_2 introduced during the wire EDM and chemical etching. After the heat treatment a light BCP was carried out to remove about 24 μm followed by high pressure rinsing at 80 bar for 1 hour and dried in class-10 clean room for overnight. End flanges with pump-out port and RF ports were assembled to the cavities using indium wire as vacuum seal and attached to the test stand and pumped overnight to a vacuum level of $1.8X10^{-9}$. Finally, the cavity test stand was inserted in a vertical cryostat and cooled to 2 K with liquid helium. The vacuum at 2 K was $5X10^{-9}$.

The necessary input and output coupling antenna were fabricated from OFHC copper rod of diameter 6.2 mm.

6.7 RF test

6.7.1 RF test setup

The schematic of VCO – PLL system used for the vertical test of cavity at 2K is shown in Fig.6.10-a [103] and the photograph of the actual LLRF control is shown in Fig.6.10-b. Superconducting cavities having a bandwidth of the order of 1 Hz (for 1 to 1.5 GHz cavities), in order to keep the cavity at resonance a phase locked loop (PLL) based control is used to track the cavity resonance and change it accordingly by the voltage control oscillator(VCO). There are

four basic blocks in the system. These are the transmitted power network, the power meter

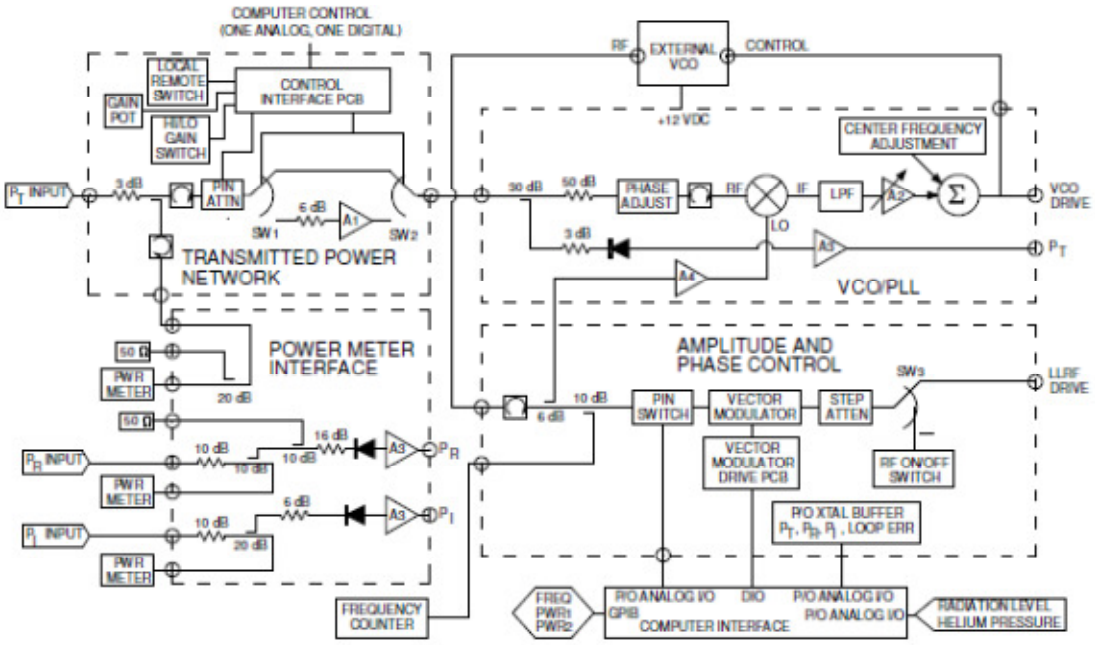

Fig.6.10-a: Block diagram of the LLRF for the cavity testing

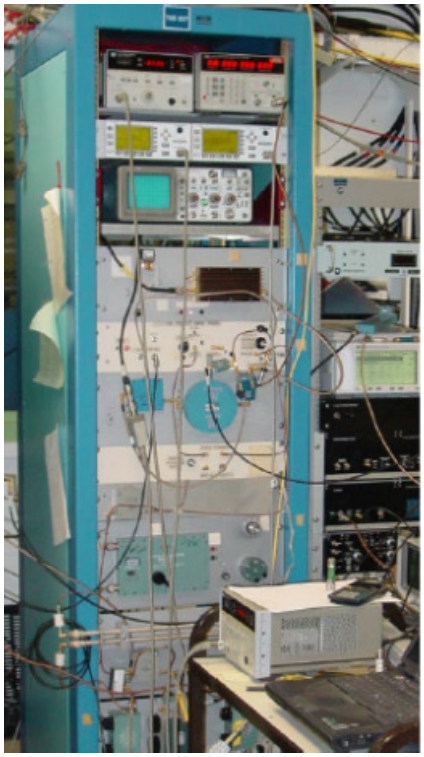

Fig.6.10-b Photograph of the LLRF system for the cavity test.

interface circuit, the VCO-PLL network and the amplitude and phase control network. It is an automated system that can be operated in manual mode.

In the measurement of variation of Q_0 with electric field near the critical coupling, the dissipated power is calculated as the forward power minus the sum RF power leaving the system as reflected and transmitted power. The error in dissipated power is given by [103],

$$\frac{\Delta P_d}{P_d} = \sqrt{\frac{(\Delta P_i)^2 + (\Delta P_r)^2 + (\Delta P_t)^2}{(P_i - P_t - P_r)^2}} \tag{6.1}$$

Where,

P_d = Power dissipated in the cavity, P_i = Incident power, P_t = transmitted power, P_r = Reflected power.

When β = 1, it is seen that the $\Delta P_r = 0$ hence error ΔP_d minimum. Another source of error is the error in Q_{ext} value of the transmitted probe during high field measurement. So the final error in Q_0 and E field measurement are given by the following relations,

$$\frac{\Delta Q_0}{Q_0} = \sqrt{\left(\frac{\Delta Q_{ext}}{Q_{ext}}\right)^2 + 4\left(\frac{\Delta P_d}{P_d}\right)^2}$$

$$\frac{\Delta E}{E} = \frac{1}{2}\sqrt{\left(\frac{\Delta Q_{ext}}{Q_{ext}}\right)^2 + \left(\frac{\Delta P_d}{P_d}\right)^2} \tag{6.2}$$

In our measurements β was 0.3 corresponding to an error $\Delta P_d/P_d = 4\%$ and $\Delta Q_{ext}/Q_{ext} = 10\%$. So a final error in Q_0 measurement is 13% and the error in E-field measurement is 6% respectively.

6.7.2 *Fine grain cavity test result*

The single cell fine grain niobium RF cavity test result is shown in Fig.6.11. As it is depicted in the figure, the low field Q was$1X10^{10}$. Also it was found that the Q_0 value decreased from

$1X10^{10}$ to $7X10^{9}$ up to E_{acc} =8MV/m. The test was carried out using two probe antennas, one for the input power and the other for the transmitted power. The Q_{ext} value for the input and output couplers were $3.28X10^{10}$ and $2.07X10^{13}$ respectively. The high power RF test was limited by the input RF power source (15 W). No multipacting or field emission was observed up to E_{acc} value 8MV/m.

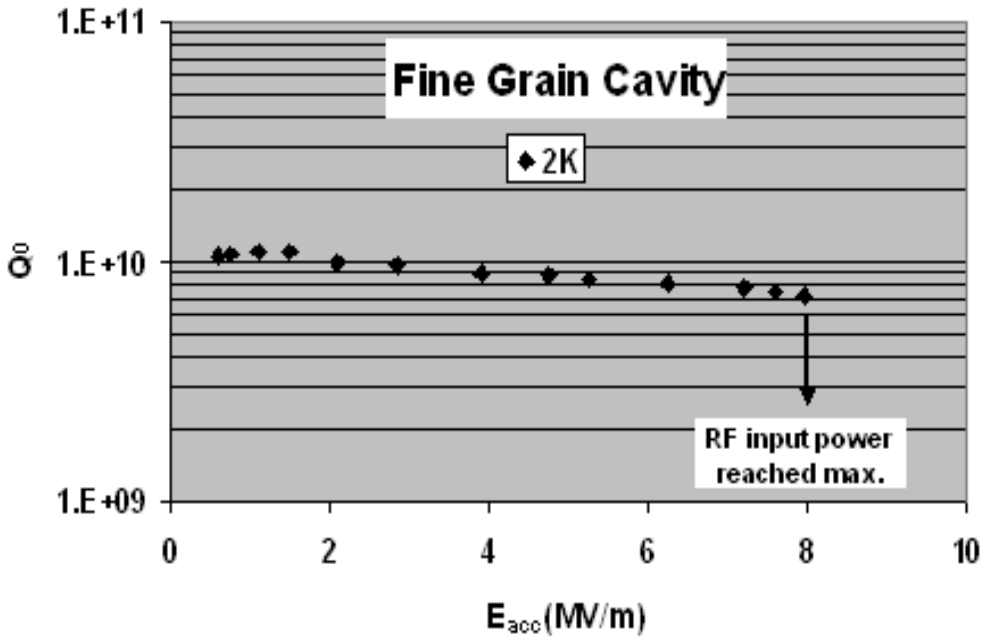

Fig.6.11 Q_0 vs E_{acc} in TM_{010} mode of 1050 MHz, $\beta = 0.49$ fine grain single cell cavity.

6.7.3 Large grain cavity test results

Similar test was carried out with the large grain cavity at 2 K and at 1.75 K . The Q_0 vs. E_{acc} curve for the large grain cavity is shown in Fig.6.12. The low field Q value was $9.89X10^{9,}$ similar to the results of the polycrstalline cavity. But the cavity quenched at about 6 MV/m both at 2K and 1.75K measurements. This was not unexpected because after the chemical etching of the cavity, lots of pits were observed in different locations of the surface and appeared to be aligned along a definite trajectory. The length of these trajectories were as long as 5 cm in few

places. Similar “pitting” after chemical etching was found on a 1.5 GHz single-cell cavity made of large grain niobium from CBMM [104]. Thermal maps measured during high-power RF test at 2 K revealed “hotspot” locations to be correlated with high density of the pits. The analysis of samples cut from the cavity showed evidence of pit formation along dislocation lines in the material.

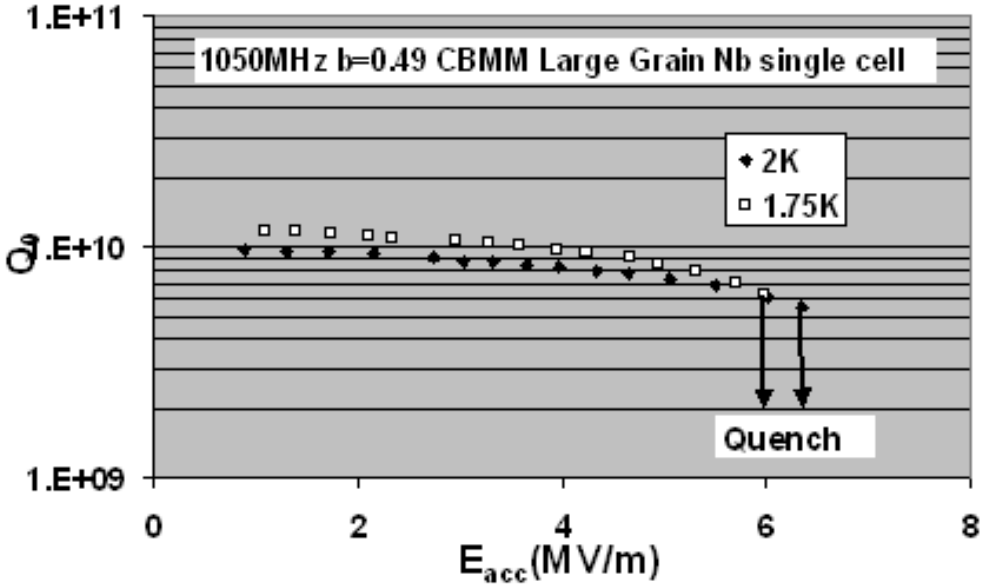

Fig.6.12 Q_0 vs E_{acc} in TM_{010} mode of 1050 MHz, $\beta = 0.49$ large grain single cell cavity.

The low field (~ 10 mT) surface resistance as a function of the He bath temperature was measured and the data were fitted [105, 106] with the sum of the temperature independent residual resistance, R_{res} and the Bardeen-Cooper-Schrieffer (BCS) surface resistance. The fitting parameters were the normal electrons mean free path, l, the energy gap at 0 K divided by the critical temperature, Δ/kT_c, and residual resistance R_{res}. The critical temperature (T_c =9.25 K), coherence length (ξ=39 nm) and the penetration depth at 0 K (λ= 42 nm) were considered as material constants for niobium. A plot of R_s as a function of 1/T is shown in Fig.6.13. The fit

parameters showed a residual resistance of 11 nΩ, the energy gap of 1.93 and normal electrons mean free path of 132 nm.

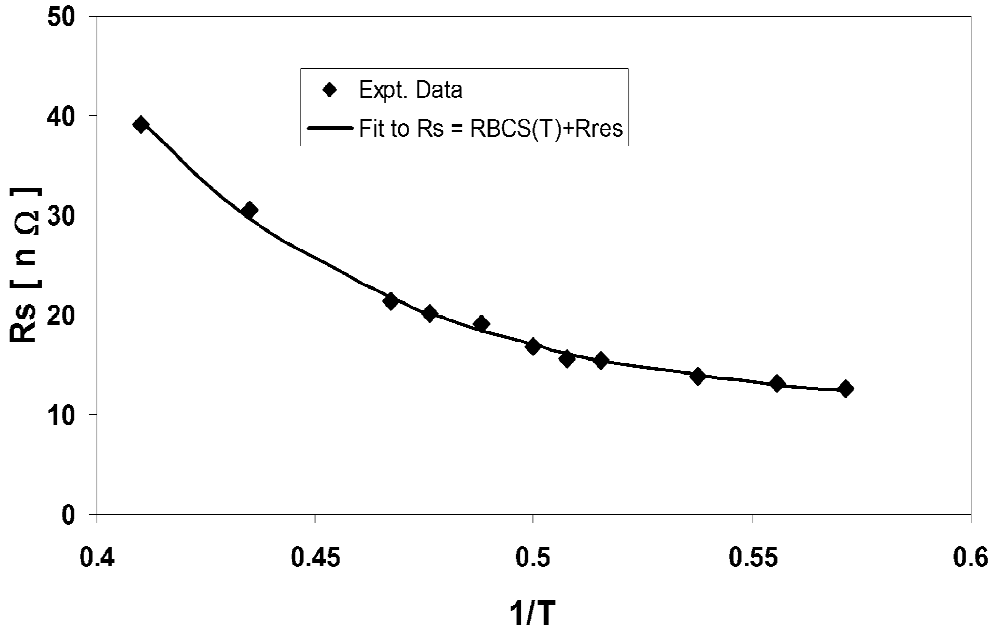

Fig.6.13 R_s vs 1/T for TM_{010} mode of the cavity. Data points are fitted with BCS theory plus residual resistance (solid line fit curve).

RF power in the cavity produces radiation pressure that acts on the cavity wall. The pressure is a function of the surface electric and magnetic fields as given by the equation,

$$P = \frac{1}{4}\left(\mu_0 H^2 - \varepsilon_0 E^2\right) \tag{6.3}$$

This pressure deforms the cavity wall, pushing outward near the equator and inward near the iris. The cavity deformations produce a frequency shift Δf which increases quadratically with accelerating field E_{acc}, producing the so-called Lorentz force detuning:

$$\Delta f = K_L E_{acc}^2 \tag{6.4}$$

Where K_L is the Lorentz force detuning coefficient. The Radiation Pressure calculated with SUPERFISH[107] on the Cavity wall at 5 MV/m accelerating gradient is shown in Fig.6.14.

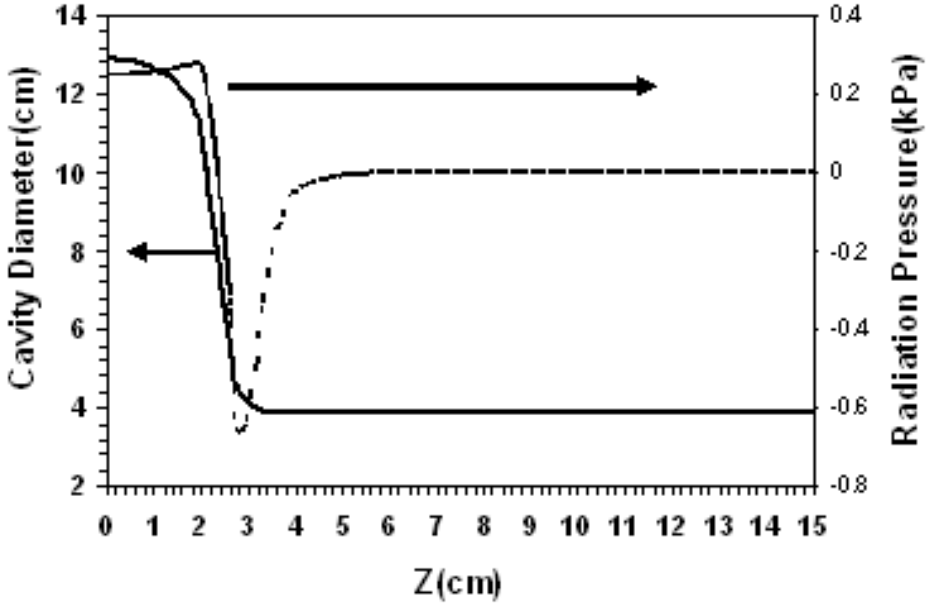

Fig.6.14 Radiation Pressure on Cavity wall at 5 MV/m accelerating gradient.

The frequency variation Δf versus E_{acc} were measured during the RF test and is shown in Fig.6.15.

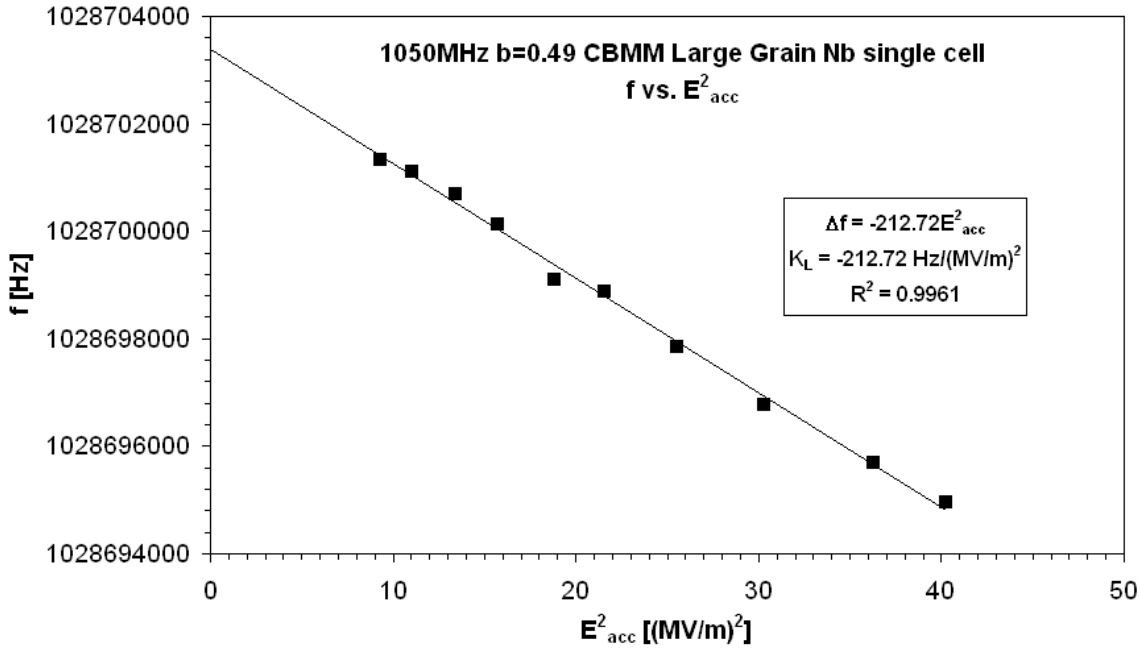

Fig.6.15 Resonant frequency variation with Eacc^2.

The experimental value of Lorentz force detuning coefficient K_L was -213 Hz/(MV/m)^2. This was significantly high value; therefore properly positioned stiffening rings between the cells were required in a multi-cell cavity. This needs a detail simulation in order to determine the position of stiffening rings so that the practical value of K_L lies between -3 and -7 Hz/ (MV/m)^2.

6.8 Medium field Q-Slope analysis

The performance of SRF cavity is mostly described by the dependence of the unloaded quality factor Q_0 with accelerating electric field E_{acc}. Several past experiments had shown that there is a continuous degradation of Q_0 with E_{acc} (or peak magnetic field B_p) in the range of 20 – 100 mT. This phenomenon is termed as 'medium field Q-slope'. To explain the medium field Q-slope J. Halbritter [108] introduced the non linear BCS term in Heabel's analytical model of R_s which takes into account the thermal impedance between the cavity inner surface and the helium bath. The dependence of R_s with the peak magnetic field at a given helium bath temperature is given by,

$$R_s(B) = R_{s0}\left[1+\gamma\left(\frac{B}{B_c}\right)^2 + O(B)^4\right] \tag{6.5}$$

Here Bc is the thermodynamic critical field of niobium (0.2 T) and Rso is the surface resistance at small magnetic fields.

Then the decrease in quality factor with increasing RF field is given by the following expression,

$$Q(B) = \frac{G}{R_{s0}}\left[1-\gamma\left(\frac{B}{B_c}\right)^2 + O(B)^4\right] \tag{6.6}$$

Our experimental results for large grain cavity at 2 and 1.75 K were fitted with the Eqn.6.5 taking γ as fit parameter. The variation of $R_s - R_{s0}$ with B_p/B_C at 2 and 1.75 K is shown in

Fig.6.16. The high γ-value (shown in Table 6.4) obtained from the fit of the data for the large grain cavity compared to the data for the fine grain one was most likely related to the presence of pits on the surface. Strong medium field Q-slope was also measured in the 1.5 GHz single cell as mentioned earlier [104]. However, it was quite uncommon for large grain cavities [109, 110]. Regions with high density of pits may have higher surface resistance because of a reduced energy gap or increased residual losses, resulting increase in γ. Because of the relatively lower RRR value of this material, the thermal conductivity may not be sufficiently high for thermal stabilization of such macroscopic defects.

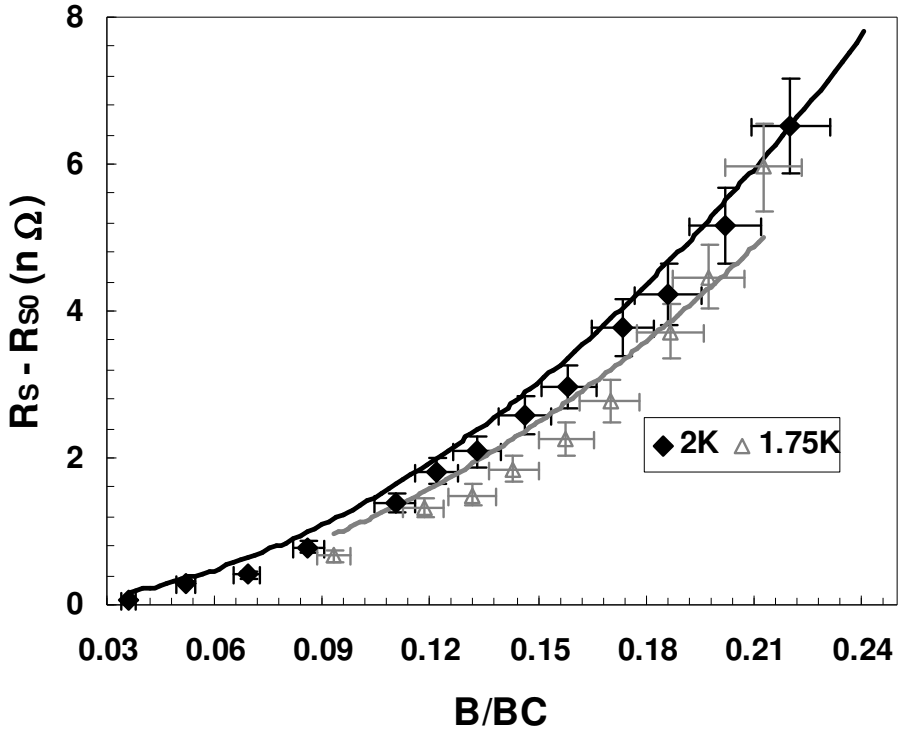

Fig.6.16 variation of $R_s - R_{s0}$ with B_p/B_C at 2 and 1.75K of the large grain cavity. Solid lines are fitted with Eqn. 6.5.

The medium field Q-slope for the fine grain cavity didn't fit well with the Eqn. 6.3. Often, a linear increase in Rs with Bp [111] is added as an additional term to Eqn.6.5. As suggested in

Ref. [111] this additional linear term can arise from the hysteresis losses due to the strong links formed on the niobium surface during oxidation [108]. The $R_s(B_p)$ dependence was then expressed as:

$$R_s(B) = R_{s0}\left[1 + R^1_{res}\left(\frac{B_p}{B_c}\right) + \gamma\left(\frac{B}{B_c}\right)^2 + O(B)^4\right] \quad (6.7)$$

Where, R^1_{res} is the residual hysteresis resistance per unit magnetic field. The increase in $R_s - R_{s0}$ with B_p/B_C at 2K of the fine grain cavity is shown in Fig.6.17.

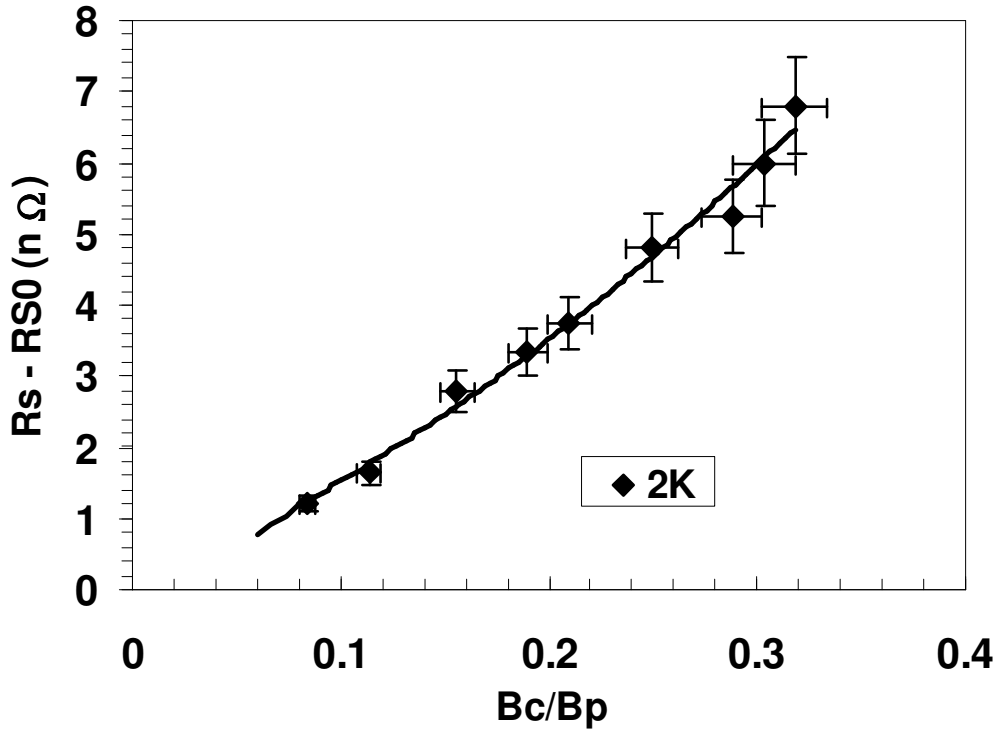

Fig.6.17 variation of $R_s - R_{s0}$ with B_p/B_C at 2K of the fine grain cavity. Solid lines are fitted with Eqn.6.7.

Table 6.4 shows the average values R^1_{res}, γ, R_{S0} and the correlation factor R^2 of the large grain cavity fitted with Eqn.6.5 and the fine grain cavity fitted with Eqn.6.7.

Table 6.4 Average values R^1_{res}, γ, R_{S0} and the correlation factor R^2 of the large and fine grain cavity.

	Large grain	Fine grain
T =2K		T =2K
R_{SO}(nΩ)	14.6±0.1	13.2±0.1
R^1_{res}(nΩ)		12.91±1.5
γ	9.2±0.26	1.776±0.42
R^2	0.97	0.986
T =1.75K		
R_{SO}(nΩ)	12.28±0.1	
R^1_{res}(nΩ)		
γ	9.0±0.47	
R^2	0.92	

6.9 Conclusion

Two single cell cavities of frequency 1050 MHz, β = 0.49 have been designed, fabricated and tested at 2 K. One was made of polycrystalline niobium and the other one was of large grain niobium. Both the cavities exhibited an unloaded Q value of $1X10^{10}$ and reached the design value of 5 MV/m for the low β section of the proton linac. The large grain cavity was quenching at 6 MV/m at 2 K and several areas with many pits on the surface were visible. The reasons for that are yet to be understood. The experimental value of Lorentz force detuning coefficient was significantly high and suggests the need for a stiffening ring for a multi-cell structure. The medium field Q-slope analysis showed a significantly higher value of γ in the large grain cavity compare to the fine grain cavity although both the cavities were subjected to similar surface treatments before the RF test. The higher value of γ was most likely related to higher RF losses at the pits' locations.

Chapter 7

Summary and Conclusion

Based on the above studies the following conclusions have been made.

1. The thermal conductivity measurement of large grain niobium samples in the Meissner state is well described by the model of Ref. [15] within the experimental error of $\pm 6\%$.
2. One important observation is that the phonon peak is eliminated by the presence of trapped vortices due to the strong scattering of phonons with vortex cores.
3. The dependence of the thermal conductivity with and without trapped vortices show the same H_{C1} and H_{C2} values in the magnetization measurement.
4. The temperature dependence of the thermal conductivity at low temperature and low magnetic field agrees qualitatively with the model of *Vinen et al*. In the vicinity of H_{C2} the thermal conductivity agrees quite well with *Houghton-Maki* theory for the virgin sample i.e without any trapped vortices. But if there is initial flux trapped within the sample, the measured thermal conductivity deviates from the *Houghton-Maki* theory and observed an increase in thermal conductivity in the range of $\mathbf{0.2 \leq \mu \leq 0.6}$.
5. The bulk properties of the samples such as T_C, B_C, H_{C1} and H_{C2} were essentially unchanged with surface treatments such as BCP, 600 ^{0}C annealing, LTB.
6. Surface pinning measurement shows that the H_{C3} value increases with the increased LTB temperature. It also shows that the surface H_{C1} is lower than the bulk H_{C1} and that the highest surface H_{C1} was obtained after baking at 120°C for 12hour.

7. The irreversibility between H_{C1} and H_{C2} decreases significantly with the low temperature baking, thus a reduction in the surface pinning centers can be inferred.
8. The increase of H_{C3}/H_{C2} ratio in the LTB regime has been analyzed with the Schmidt's model taking into account the low temperature correction to H_{C3}/H_{C2} ratio. The enhanced H_{C3}/H_{C2} ratio has been interpreted as the increased contaminated surface layer thickness. This fact is further corroborated by the penetration depth measurement.
9. The important observation in the positron annihilation studies (PAS) is that the surface defect density increases after the annealing where as in the bulk the defect density decreases. This is complimentary to the conclusion inferred with the magnetization measurement.
10. Elastic behavior of high purity niobium remains unchanged with different heat treatments only a change in yield strength is observed after 1200^0C heat treatment.
11. RF Properties of 1050 MHz, β = 0.49 single cell Elliptical cavity has been studied by means of 2D cavity tuning code SUPERFISH and 3D High Frequency Simulation code CST Microwave Studio. Electromagnetic properties of optimized cavity shape carried out on 2D code SUPERFISH are compared with 3D code CST Microwave Studio. Numbers of mesh cells are optimized by the adaptive mesh solver technique. It has been observed that the mode frequency remains almost constant for more than 10^5 mesh cells.
12. Two single cell cavities of frequency 1050 MHz, β =0.49 have been designed, fabricated and tested at 2 K. One was made of polycrystalline niobium and the other one was of large grain niobium. Both the cavities exhibited an unloaded Q value of $1x10^{10}$ and reached the design value of 5 MV/m for the low β section of the proton linac.

13. The medium field Q-slope analysis showed a significantly higher value of γ in the large grain cavity compare to the fine grain cavity although both the cavities were subjected to similar surface treatments before the RF test. The higher value of γ was most likely related to higher RF losses at the pits' locations.

REFERENCES

[1] H. Kammerlingh Onnes, Electrician **67**, 657 (1911).

[2] John C. Gallop (1990). *SQUIDS, the Josephson Effects and Superconducting Electronics*. CRC Press. pp. 3, 20. ISBN 0-7503-0051-5.

[3] J. G. Bednorz and K. A. Müller (1986). "Possible high T_c superconductivity in the Ba−La−Cu−O system". *Z. Physik, B* **64** (1): 189–193. doi:10.1007/BF01303701.

[4] Pines, D. (2002), "The Spin Fluctuation Model for High Temperature Superconductivity: Progress and Prospects", *The Gap Symmetry and Fluctuations in High-Tc Superconductors*, New York: Kluwer Academic, pp. 111-142, doi:10.1007/0-306-47081-0_7, ISBN 0-306-45934-5

[5] W. Meissner and R. Ochsenfeld *Naturwissenschaften* 21, 787(1933).

[6] London, F.; H. London (March 1935). "The Electromagnetic Equations of the Supraconductor". *Proc. Roy. Soc. (London)* **A149** (866): 71. ISSN 0080-4630

[7] W. S. Corak, B. B. Goodman, C. B. Satterthwaite, and A. Wexler, Phys. Rev. **102**, 656 (1956).

[8] A. Brown, M. W. Zemansky, and H. A. Boorse, Phys. Rev. **92**, 52 (1953).

[9] A. T. Hirshfeld, H. A. Leupold, and H. A. Boorse, Phys. Rev. **127**, 1501 (1962).

[10] C. A. Bryant and P. H. Keesom, Phys. Rev. **123**, 491 (1961).

[11] J.Bardeen, L. N. Cooper and J.R. Schrieffer, Phys. Rev. **108**, 1175 (1957).

[12] C. J. Gorter and H. B. J. Casimir, Physica 1, 306 (1934).

[13] F. and H. London, Proc. Roy. Soc. (London) A149, 71 (1935).

[14] A. B. Pippard, Proc. Roy. Soc. (London) A216, 547 (1953).

[15] T. E. Faber and A. B. Pippard, Proc. Roy. Soc. (London) A231, 336 (1955).

[16] V. L. Ginzburg and L. D. Landau, Zh. Eksperim, I Teor Fiz. 20, 1064 (1950).

[17] Alex Gurevich lecture on superconductivity.
http://epaper.kek.jp/srf2007/TUTORIAL/PDF/Tutorial_1a.pdf

[18] D. Saint-James and P. D. de Gennes, Phys. Letters **7**, 306 (1964).

[19] Pozar, David M. *Microwave Engineering.* s.l. : Wiley, 2004. 978-0471448785.

[20] T. P. Wangler, Principles of RF Linear Accelerators, Jone Wiley & Sons,Inc. 1998.

[21] H. Padamsee, et al., RF Superconductivity for Accelerators, John Wiley & Sons, 1998.

[22] J. Matricon *et al.*, Phys. Lett. A, 24:241, (1967).

[23] R. B. Flippen, Phys. Lett. A, 17:193, (1965).

[24] T. Yogi et al., Phys. Rev. Lett., 39:826 (1977).

[25] D. C. Mattis and J. Bardeen, Phys. Rev., 111:412 (1958).

[26] J. Halbritter, Z. Physik, 238:466-476 (1970).

[27] Z. H. Sung dissertation, "The Influence of Grain Boundaries on the Properties of Superconducting Radio Frequency Cavity Niobium" University Of Wisconsin – Madison (2010).

[28] L. Lilje dissertation, “Experimental Investigations on Superconducting Niobium Cavities at Highest Radiofrequency Fields” Hamburg, (2001).

[29] J. Halbritter, Appl. Phys. A. “On the oxidation and on the superconductivity of niobium” Solids Surf. 43, 1 (1987).

[30] F. Palmer, in the proceedings of the 3rd workshop on RF superconductivity, edited by K. Shepard, Argonne National Laboratory, Argonne, IL, USA, ANL-PHYS-88-1 (1988).

[31] P. Kneisel, “Surface characterization of bulk Nb: What has been done, what has been learnt?” in the proceedings of the 11th workshop on RF superconductivity, Travemünde, Tu002, (2003).

[32] C.Z. Antonie *et al*., “H in niobium: Origin and Method of Detetction” in the proceedings of 1st international workshop on hydrogen in materials and vacuum systems. AIP conference proceedings. Vol 671, p176-189, (2003).

[33] J. Knobloch, “The *Q* disease in Superconducting Niobium RF cavities” in the proceedings of 1st international workshop on hydrogen in materials and vacuum systems. AIP conference proceedings, Vol 671, p133-150, (2003).

[34] G. Ciovati dissertation, “ Investigation of the Superconducting Properties of Niobium Radio-Frequency Cavities” Old Dominion University (2005).

[35] T. Furuya et. Al., in Proceedings of the 5th symposium on Accelerator Science and Technology, KEK, p. 122 (1984).

[36] P. Kneisel, G.R.Myneni, G.Ciovati, J.Sekutowicz, T.Carneiro, Proc of the 2005 Particle Accelerator Conference,Tennessee, TPPT076.

[37] P. Kneisel, Proc of the 13th SRF Workshop, Peking Univ, China, October 2007, Th102.

[38] P. Bauer et.al, “Review of Q-drop in SRF cavities”, TD-05-56, January 2006.

[39] B. Visentin, “Q-Slope at High Gradients: Review of Experiments and Theories”, Proceedings of the 2003 workshop on RF superconductivity, Sept. 2003, Luebeck, Germany

[40] G. Ciovati, “Effect of Low-Temperature Baking on the Radio-Frequency Properties of Niobium Superconducting Cavities for Particle Accelerators”, J. Appl. Phys. 96, p. 1591, 2004

[41] L. Lilje, EPAC 04

[42] B. Visentin, J.P. Charrier, B. Coadou, D. Roudier, “Cavity Baking: A Cure for the High Accelerator Field Q0 Drop”, Proceedings of the 1999 workshop on RF superconductivity, 1999, Santa Fe, USA

[43] P. Kneisel, “Preliminary Experience with in-situ Baking of Niobium Cavities”, Proceedings of the 1999 workshop on RF superconductivity, 1999, Santa Fe, USA.

[44] G. Eremeev, “New Results on the High Field Q-Slope”, presentation at the 2005 workshop on RF superconductivity, July 2005, Ithaca, USA.

[45] S. Casalbuoni, L. von Sawilski, J. Koetzler, “Superconductivity Above Hc2 as a Probe for Niobium RF Cavity Surfaces”, Proceedings of the 2003 workshop on RF superconductivity, Sept.2003, Luebeck, Germany.

[46] S. Casalbuoni, Nuclear Instruments and Methods in Physics Research A, 538, 45-64 (2005).

[47] J. Lowell and J.B.Sous, Phys. Lett. 25A, 469 (1967).

[48] W.F.Vinen, E.M.Forgan, C.E.Gough and M.J.Hood, Physica (Utrecht), 55, 94 (1971).

[49] Sergei Sergeenkov and Marcel Ausloos, Phys. Rev. B 52, 3614–3618 (1995).

[50] K. Maki, Phys. Rev. 158, 397 (1967).

[51] J. B. Sousa, Physica (Utrecht) 55, 507 (1971).

[52] F.Koechlin and B. Bonin, Supercond. Sci. Technol., 9, 453, (1996).

[53] J. Bardeen, G. Rickayzen and L. Tewordt, Phys. Rev., 113, 982 (1959).

[54] Caroli, C., et. al. , Phys. Letters, 9 (1964) 307; Caroli et. al., Phys. Kondens. Mat. 3, 380 (1965).

[55] Hansen, E.B., Phys. Letters, 27A (1968) 576.

[56] Bergk, W. and Tewordt, L., preprint.

[57] P. H. Kes, J. P. M. van der Veeken, and D. De Klerk, J. Low. Temp. Phys. 18, 355 (1975).

[58] A. Houghton, K. Maki, Phys. Rev. B 4, 843 (1971).

[59] N. J. Imfeld, W. Bestgen and L. Rinderer, J. Low Temp. Phys. 60 (1985) 223.

[60] D. K. Finnemore and D. E. Mapother, Phys. Rev. 140 No. 2A (1965) 507.

[61] G.Ciovati, J.Mondal, P. Kneisel, G. R. Myneni, M. Morrone, R. Bundy, B. Clemens, T. Elliott, G. Slack, L. Turlington, Proc of the 13th SRF Workshop, Peking Univ, China, October 2007, paper TuP01.

[62] J. Lowell and J.B.Sous, Phys. Lett. 25A, 469 (1967).

[63] W.F.Vinen, E.M.Forgan, C.E.Gough and M.J.Hood, Physica (Utrecht), 55, 94 (1971).

[64] Sergei Sergeenkov and Marcel Ausloos, Phys. Rev. B 52, 3614–3618 (1995).

[65] K. Maki, Phys. Rev. 158, 397 (1967).

[66] J. B. Sousa, Physica (Utrecht) 55, 507 (1971).

[67] F.Koechlin and B. Bonin, Supercond. Sci. Technol., 9, 453, (1996).

[68] J. Bardeen, G. Rickayzen and L. Tewordt, Phys. Rev., 113, 982 (1959).

[69] Caroli, C., et. al. , Phys. Letters, 9 (1964) 307; Caroli et. al., Phys. Kondens. Mat. 3, 380 (1965).

[70] G.Ciovati, Tech note, Jlab, 2006. http://tnweb.jlab.org/tn/2006/06-019.pdf.

[71] V.V.Shmidt, in Physical Metallurgy, Physical Chemeistry and Metals Physics of Superconductors,p.90 (Moscow: Nauka, in Russian 1967).

[72] C.Hu and V.Korenman, Phys. Rev. 185, 672(1969).

[73] G.Ciovati, Appl. Phys. Lett 89, 022507(2006).

[74] Koch et. Al

[75] Schawlow and Davlin

[76] P.B.Miller, Phy.Rev, 113, 1209 (1959).

[77] S. K. Sharma et. al. , BARC news letter, October, 2008. http://barc.gov.in/publications/nl/2008/20081026.pdf

[78] R. Krause-Rehberg and H.S. Leipner, Positron Annihilation in Semi-conductors (Springer Series in Solid State Sciences 127, 1998).

[79] B. Visentin et. al., Phys. Rev. ST Accel. Beams 13, 052002 (2010).

[80] M. J. Puska and R. M. Nieminen. Theory of positrons in solids and on solid surfaces. *Review of Modern Physics*, 66(3):841–897, July 1994.

[81] A. Perkins and J. P. Carbotte. Effect of the positron-phonon interaction on positron motion. *Physical Review B*, 1(1):101–107, January 1970.

[82] K. O. Jensen and A. B. Walker. Positron thermalization and non-thermal trapping in metals. *Journal of Physics: Condensed Matter*, 2(49):9757–9775, 1990.

[83] R. M. Nieminen and J. Oliva. Theory of positronium formation and positron emission at metal surfaces. *Physical Review B*, 22(5):2226–2247, September 1980.

[84] B. Bergersen, E. Pajanne, P. Kubica, M. J. Stott, and C. H. Hodges. Positron diffusion in metals. *Solid State Communications*, 15(8):1377–1380, October 1974.

[85] O. V. Boev, M. J. Puska, and R. M. Nieminen. Electron and positron energy levels in solids. *Physical Review B*, 36(15):7786–7794, November 1987.

[86] E. Soininen, H. Huomo, P. A. Huttunen, J. Mäkinen, A. Vehanen, and P. Hautojärvi. temperature dependence of positron diffusion in cubic metals. *Physical Review B*, 41(10):6227–6233, April 1990.

[87] E. Soininen, J. Mäkinen, D. Beyer, and P. Hautojärvi. High-temperature positron diffusion in Si, GaAs, and Ge. *Physical Review B*, 46(20):13104–13118, November 1992.

[88] M. J. Puska, C. Corbel, and R. M. Nieminen. Positron trapping in semiconductors. *Physical Review B*, 41(14):9980–9993, May 1990.

[89] H. Peisl, in *Hydrogen in Metals I*, edited by G. Alefeld and J. Völkl, Topics in Applied Physics Vol. 28 Springer-Verlag, Berlin, 1978, p. 53.

[90] P. Hautojärvi, in *Positrons in Solids*, edited by P. Hautojärvi , Springer-Verlag, Berlin, 1979, p. 1.

[91] D. Larsen and J. Nørskov, J. Phys. F: Met. Phys. 9, 1975, 1979.

[92] M. Baskes and C. Melius, Z. Phys. Chem., Neue Folge 116, 289, 1979.

[93] V. Palmieri, F. Stivanello, C. Roncolato, M. Valentino Proc, 10th SC RF workshop, 2001 Tsukuba.

[94] J. Cizek et al. Phys. Rev. B 79, 054108 (2009).

[95] P. Singh et. al., Accelerator development in India for ADS programme, Pramana **68** (2007) 331.

[96] R. L. Kustom. "An Overview of the Spallation Neutron Source Project", Linac 2000, August 2000.

[97] http://www.ganil.fr/eurisol/Final_Report

[98] G. R. Myneni, AIP Conf. Proc. 927, 41 (2007); doi: 10.1063/1.2770677

[99] "RF Properties of 1050 MHz, β = 0.49 Elliptical cavity for High Current Proton Acceleration" Amitava Roy , J. Mondal, K. C. Mittal, Journal of Instrumentation, 3 P04002, 2008 (IOP Publication).

[100] "Design Criteria for Elliptical Cavities" C. Pagani, D. Barni, A. Bosotti, P. Pierini, G. Ciovati, Proc. of the 10th SRF Workshop,Tsukuba, Japan , (2001) 115.

[101] J. Mondal et. al. , Journal of Instrumentation, 6 T11003, 2011 (IOP Publication).

[102] J.Mondal, G.Ciovati, P.kneisel, K.C.Mittal, G.R.Myneni, Proc. of the 14th SRF Workshop,dBB Forum, Belin, Germany, September 2009, Paper THOAAU01.

[103] T. Powers, “Theory and practice of cavity test systems”, Proc. Of the 10th SRF workshop, Tutorial session, 2005.

[104] X. Zhao, G. Ciovati and T. R. Bieler, Phys. Rev. ST Accel. Beams **13**, 124701 (2010)

[105] J. Halbritter., “FORTRAN Program for the Computation of the Surface Impedance of Superconductors”, FZK 3/70-6, Karlsruhe, 1970.

[106] G. Ciovati, “SUPERFIT: a Computer Code to Fit Surface Resistance and Penetration Depth of a Superconductor”, JLAB-TN-03-003, 2003.

[107] J.H. Billen and L.M. Young, *Poisson SUPERFISH*, LA-UR-96-1834, L.A.N.L.

[108] J. Halbritter, J. Appl. Phys. 97 (2005) 083904.

[109] G. Ciovati, P. Kneisel and G. R. Myneni, “America's Overview of Superconducting Science and Technology of Ingot Niobium**”,** in Proceedings of the First International Symposium on the Science and Technology of Ingot Niobium, AIP Conference Proceedings 1352 (Melville, NY. 2011), p. 25

[110] W. Singer et al., “Advances in Large Grain Resonators for the European XFEL”, in Proceedings of the First International Symposium on the Science and Technology of Ingot Niobium, AIP Conference Proceedings 1352 (Melville, NY. 2011), p. 13.

[111] G. Ciovati, J. Halbritter, Physica C 441 (2006) 57-61.

Publications during Ph.D work

Journal Publications

1. **J. Mondal,** G.Ciovati, K.C.Mittal, G.R.Myneni**.** (2012)**. "**Thermal conductivity of large grain niobium and effect of trapped vortices in the temperature range 1.8-5K" Pramana-Journal of Physics, 635, 78(4), (2012).

2. **J. Mondal**, G. Ciovati, P. Kneisel, K. C. Mittal and G. R. Myneni (2011). "Design, fabrication, RF test at 2K of 1050 MHz, $\beta = 0.49$ single cell large and fine grain niobium cavity", Journal of Instrumentation, 6 – T11003, JINST, 2011.doi:10.1088/1748-0221/6/11/T11003.

3. Amitava Roy, **J. Mondal** and K.C. Mittal (2008). "RF properties of 1050 MHz, $\beta = 0.49$ Elliptical cavity for High Current Proton Acceleration", Journal of Instrumentation, 3-P04002, JINST, 2008.

Conference Publications

4. **J. Mondal**, K.C.Mittal, G.Ciovati, P.kneisel, G.R.Myneni, "Characterization of Ingot Materials for SRF Cavity Production", Proceedings of **SRF2009**, Berlin, Germany, THOAAU01, Page: 455-461.

5. **J. Mondal**, T.K.Saha, S.Sarkar, S.B.Jawale, R. S. Vohra, A.V.Bapat, "Design, fabrication, room temperature RF test of 1050 MHz, $\beta = 0.49$ single cell large grain niobium cavity"**,** International Vacuum Symposium-2012, VECC, Kolkata.

6. T.K.Saha, **J. Mondal**, K.C.Mittal, K.G.Bhushan and A.V.Bapat, "Fabrication of niobium superconducting accelerator cavity by electron beam welded joints" International Vacuum Symposium-2012, VECC, Kolkata.